2016

Advanced Reservoir Modeling and Fluid Flow Studies of Natural Gas Production from the Hydrate Reservoirs of the Alaska North Slope

Taiwo Ajayi

Advanced Reservoir Modeling and Fluid Flow Studies of Natural Gas Production from the Hydrate Reservoirs of the Alaska North Slope

Taiwo Ajayi

Dissertation submitted
to the Benjamin M. Statler College of Engineering and Mineral Resources
at West Virginia University

in partial fulfillment of the requirements for the degree of

Doctor of Philosophy in
Chemical Engineering

Brian Anderson, Ph.D., Chair
Charter Stinespring, Ph.D.
Debangsu Bhattacharyya, Ph.D.
Ilkin Bilgesu, Ph.D.
Evgeniy Myshakin, Ph.D.

Department of Chemical Engineering

Morgantown, West Virginia
2016

Keywords: methane hydrates, secondary hydrate formation, reservoir modeling, natural gas production, reservoir characterization, geostatistics, fluid flow, flow assurance, CMG STARS, Alaska North Slope

Abstract

Advanced Reservoir Modeling and Fluid Flow Studies of Natural Gas Production from the Hydrate Reservoirs of the Alaska North Slope

Taiwo Ajayi

The emerging possibility of the production of gas hydrates as an unconventional source of energy have spurred many objectives for research studies going on in this area. One of these is the U.S national hydrate research program with a primary goal of determining the tools and technologies for environmentally safe gas production from hydrate reservoirs. The work presented in this thesis is motivated by the need to provide reliable reservoir model-based predictions to support proposed long-term hydrate field production tests on the Alaska North Slope permafrost. While first order predictions have been made from reservoir models based on assumptions of homogeneity of properties, it has been shown that the degree of reservoir heterogeneity can significantly affect the quantitative and qualitative results.

This study is an advanced and robust evaluation of the gas production potential of hydrate reservoirs. The hydrate deposits within the region of Prudhoe Bay Unit (PBU) "L-Pad" and Mt. Elbert Well vicinity of the Milne Point Unit of the Alaska North Slope are primary subjects of investigation. It is an effort to build data-driven heterogeneous hydrate reservoir models by applying both conventional and novel methods of reservoir characterization to maximize the utilization of the available field data. Using well log data obtained from 78 L-Pad wells, geostatistical techniques were employed to obtain stochastic simulations of the 3D distribution of reservoir properties in the target hydrate units of the L-Pad region. Models for the Mt. Elbert deposit were developed by combining data obtained from well logs obtained during the 2007 Mt. Elbert stratigraphic test and a 3D seismic survey of the region. Additionally, wellbore flow assurance studies were coupled with reservoir models in order to predict potential production issues arising from the formation of secondary hydrates or ice within the wellbore fluids being produced under high pressure and low temperature conditions.

CMG STARS, a finite difference reservoir modeling software package, was used to solve the material and energy balance equations in which an equilibrium model of hydrate dissociation was used. The simulator also provides a means to couple artificial lift design of the wellbore with the reservoir model using established pressure drop-heat loss correlations. Gas and water production rates and the evolution of reservoir properties were extensively studied in varying production scenarios with depressurization as the primary recovery technique.

Predictions from 10 geostatistical realizations of the L-Pad model were within narrow ranges, which is an indication of the robustness and reliability of the model. Uncertainty assessment and sensitivity studies on the Mt. Elbert model showed that higher gas production rates were achieved in deeper (hence warmer) reservoirs and confirmed earlier studies that production from the Mt. Elbert prospect may too cold to be economically feasible. Furthermore, contrary to predictions from homogeneous models, the effect of secondary hydrate formation in the reservoir on gas flow was found to be very minimal. However, flow assurance and artificial lift design studies show that wellbore pressure and temperature conditions must be effectively managed to prevent formation of secondary hydrates or ice.

To the Almighty God, to whom I owe all that I am and all that I will ever be!

To my father, the late Dr. E.O Ajayi, whose life continues to inspire me even long after his passing on.

To my mother, Eunice Wuraola Ajayi, who nurtured and molded me with all her love, strength and courage.

And

To my wife, Abidemi Anike Ajayi, in whose love I will always find warmth, joy and peace.

Acknowledgement

My sincere and deep gratitude goes to all individuals and organizations that have supported my academic journey in one way or the other.

Firstly, I would like to appreciate my research advisor, Professor Brian Anderson, whose commitment to his students' success while instilling a performance-based culture to work, has given me every reason to believe that I could not have had a better understanding and motivation needed to complete my doctoral degree.

I wish to express my profound gratitude to the National Energy Technology Laboratory (NETL) of the U.S. Department of Energy (DOE) and the U.S. Geological Survey for providing funding to this project. I am specifically thankful to Dr. Evgeniy Myshakin, who was much more than a direct report during and after my work at NETL, as he provided selfless guidance to my work with the most remarkable patience. I also thank Dr. Yongkoo Seol for providing me the opportunity to benefit from his vast knowledge and experience with hydrates during the time I spent at NETL. A very special thanks to Dr. Tim Collett and Ms. Margarita Zyrianova of USGS for providing data and insightful directions for the project.

Furthermore, I would like to appreciate all past and present members of Dr. Anderson's group including Dr. Manohar Gaddipati, Dr. Nagasree Garapati, Dr. Srinath Velaga, Dr. Xiaoning He, Prathyusha Sridhara, Manish Nandanwar, Bryce Macaulay, Kelydra Welcker and Matthew Tacker, for sharing ideas with me one way or the other.

I also want to extend my appreciation to my professors at my former school Texas A & M University-Kingsville, especially Dr. David Murphy and Dr. Patrick Mills for providing me the opportunity to learn from and work with them.

A very special acknowledgement goes to Mr. Adebola Odu-Onikosi and Mr. Joseph Oluwasusi of Homble Energy Services Nigeria Ltd whose kind words of advice and financial support have nurtured my career aspirations. To Engr. (Dr.) and Mrs. Ajiboye, Mr. Israel Ogunleye, Mr. Tunde Sowunmi, Pastor (Mrs.) Yemisi (of MFM-Houston), I say a very big "thank you" for all your kind assistance in every way.

I am grateful to my entire family particularly Mrs. Richmonda Adeagbo (my "second mother") and my elder sister Mrs. Oluwatosin Adebayo (my "assistant mom" in Philadelphia) for their love and encouragement through thick and thin. On behalf of myself, Abidemi and Anjolaoluwa, I thank you all!

Table of Contents

List of Tables

List of Figures

1. Introduction

1.1 Overview and History of Gas Hydrates

Gas hydrates (properly known as "gas clathrate hydrates") are non-stoichiometric ice like compounds formed by the trapping of a guest molecule (usually gases) in a cage of hydrogen bonded water molecules. They were first discovered in 1810 by Sir Humphrey Davy[1], who observed a yellow precipitate when feeding chlorine gas through water at temperature near freezing point. In prior laboratory experiments, Priestley[2] had observed that vitriolic air (SO_2) impregnated water and caused it to freeze and refreeze to form what would later be known as SO_2 hydrate. Perhaps, the first evidence of the existence of CO_2 hydrate was demonstrated by Wroblewski[3] during one of studies conducted on carbonic acid, where he increased the pressure of his CO_2-H_2O system and observed a white material resembling snow.

In nature, gas hydrates occur both in the permafrost regions and in the marine sediments in the oceans and deep lakes where pressure-temperature conditions are suitable and where sufficient methane is delivered to the zone of hydrate stability in the uppermost sediments[4]. Stability of hydrates is favored by low temperature, high pressure, availability of a hydrate-forming gas and water.

1.1.1 Hydrate structure

The gas molecules in gas hydrates are not chemically bounded to the water molecules; instead, they are only simply trapped inside the crystal lattice. The hydrates have a physical appearance which resembles that of packed snow or ice. They burn easily, thus, they are also called "flammable ice". Clathrate hydrates can possess many different crystal structures but only three structures are known to occur in natural environments. These structures, which are different from any of the known forms of ice, have been classified into Structure I (sI), Structure II (sII) and the

most recently identified Structure H (sH). The type of structure formed depends on the size of the guest molecule. The type of structure formed depends on the size of the guest molecule, which occupies a combination of small and large cages.

A small cage has 12 pentagonal faces (denoted as 5^{12}) while a large cage could either have 12 pentagonal and 2 hexagonal faces ($5^{12}6^2$), as found in sI structures, or 12 pentagonal and 4 hexagonal faces ($5^{12}6^4$), as found in sII structures. These structures are shown in Figure 1-1[5].

A unit cell of a sI hydrate structure contains 46 water molecules and is made up of two 5^{12} (small) cages and six $5^{12}6^2$ (large) cages. Gases that form sI hydrates include methane, ethane, CO_2 and H_2S. A unit cell of sII hydrate is composed of 136 water molecules in a combination of sixteen 5^{12} (small) and eight $5^{12}6^4$ (large) cages. Large guest molecules such as propane and *i*-butane are common ***pure*** sII hydrate formers. The Largest sII formers such as n–butane and cyclohexane actually require a small help guest molecule which fits in the 5^{12} cages to form a ***mixed*** hydrate. A mixed hydrate is formed when guest molecules from two or more gases are trapped in the cages.

Structure type sH, first reported by Ripmeester and coworkers[6], is formed by even larger guest molecules and is a much less frequently observed structure. It has a hexagonal lattice containing 34 water molecules and three cage types: three 5^{12} cages, two medium $4^3 5^6 6^3$ cages, and one large $5^{12}6^8$ cage. The sH hydrate structure forms with molecules such as methylcyclohexane, however, like the largest sII formers, it only forms when a second smaller help-gas (e.g. CH_4) is present.

It is to be noted, however, that there can be structural transitions to other hydrate structures under different conditions of temperature, pressure and gas composition. Only sI and sII have been identified with hydrocarbon gas components and they are usually formed by gas molecules of smaller size compared with the guest molecules of sH formers[7].

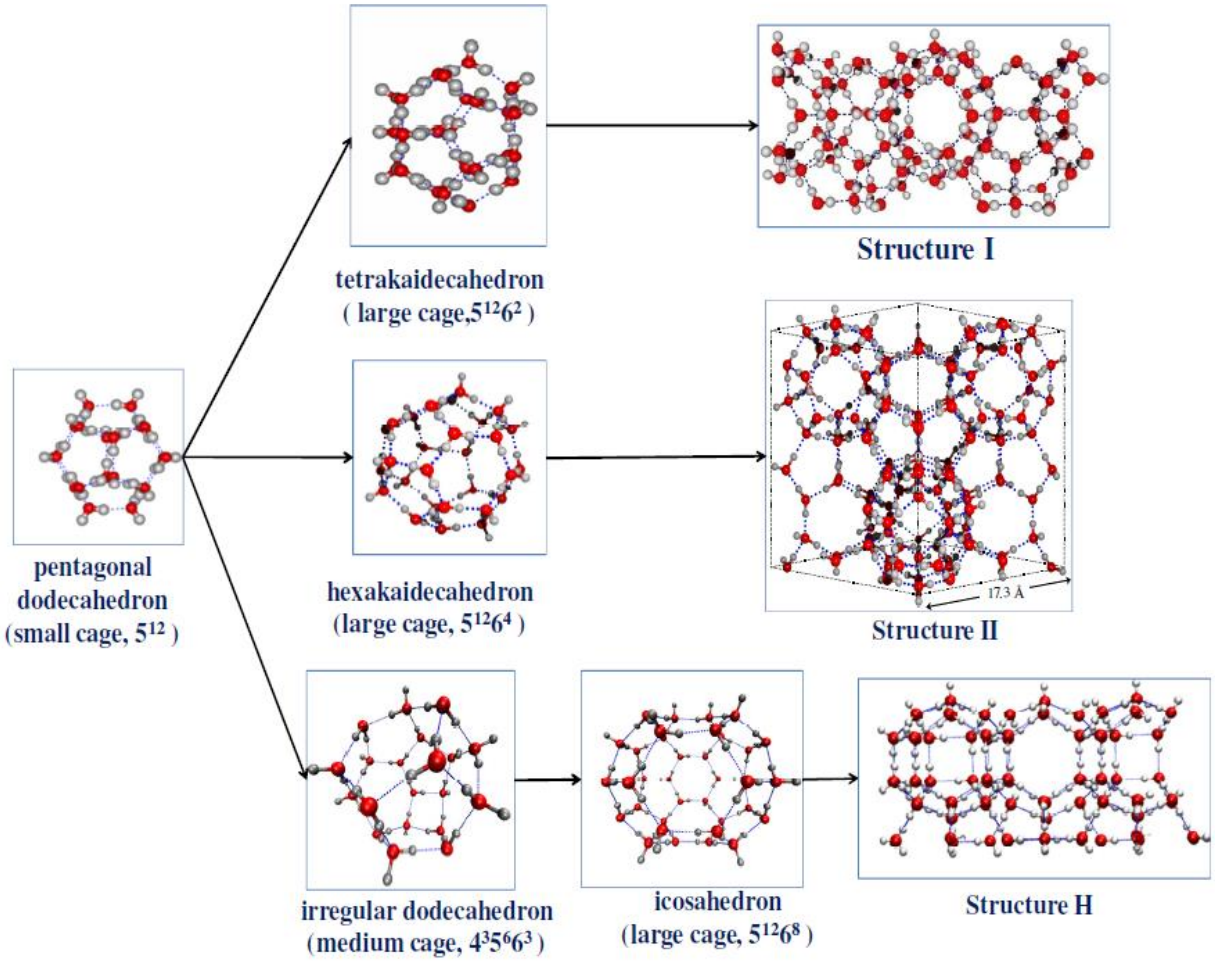

Figure 1-1: Hydrate crystals and their component cavities

The hydration number is the ratio of the number of water molecules to number of guest molecules in a unit cell. For example, the hydration number for a sI hydrate when all cages are filled is 5.75 (= 46/8) since a unit cell will contain 46 water molecules and 8 guest molecules. Hydrates are non-stoichiometric and hydration numbers vary widely based on the hydrate former and conditions. The hydration number increases with a decrease in the fractional cage occupancy. In methane hydrates, methane occupies almost all of the cages (around 95% of the large cages and 85% of the small cages) with $n = \sim 6^8$.

1.1.2 Stability of hydrates

Understanding the stability of hydrates is very crucial to understanding how hydrates occur in nature. It also helps in the investigation of possible gas recovery techniques and in the prevention of hydrate formation in pipelines (as in flow assurance applications). There are four conditions which need to be satisfied for the formation of gas hydrates:

- Low temperature
- High Pressure
- Availability of methane or other hydrate forming gases
- Availability of free water

Hydrate stability is completely restricted to these four criteria, outside of which, hydrates become unstable. Figure 1-2, shows a plot of the hydrate phase equilibrium (*P-T*) diagram for hydrate deposits of the Prudhoe Bay region of the ANS and geothermal temperature obtained from equilibrated distribution temperature sensor (DTS) readings of the Ignik-Sikumi well. The high temperatures at zero depth are as a result of the temperature disturbances due to drilling pad activities at the surface. Geothermal gradient increases as depth transitions from the permafrost region to the HBS. The region between the top and bottom intersections of both curves is known as the hydrate stability zone (HSZ). The top intersection (at ~100 m depth) is the upper bound of the HSZ and the bottom intersection (at ~ 900 m depth) is defined as the base of hydrate stability zone (BHSZ). Any condition of temperature and pressure within the HSZ and to the left of the equilibrium curve implies a possibility of a hydrate phase. Increasing temperature and/or decreasing the pressure would tend towards dissociating the hydrate. Other factors which affect hydrate stability are salinity and presence of heavier hydrocarbons as guest molecules. These will cause the equilibrium curve to shift either to the left (as in the case of increased salinity) or to the right (as in the case of heavier hydrocarbons).

The presence of heavier natural gas components, such as ethane, propane, or isobutane, will cause the hydrate stability depth to increase due to a displacement of the phase boundary line away from the geothermal gradient. However, arctic hydrates have not been found at depths greater than 2000 m below the surface, due to the high temperatures resulting from the geothermal gradient[7].

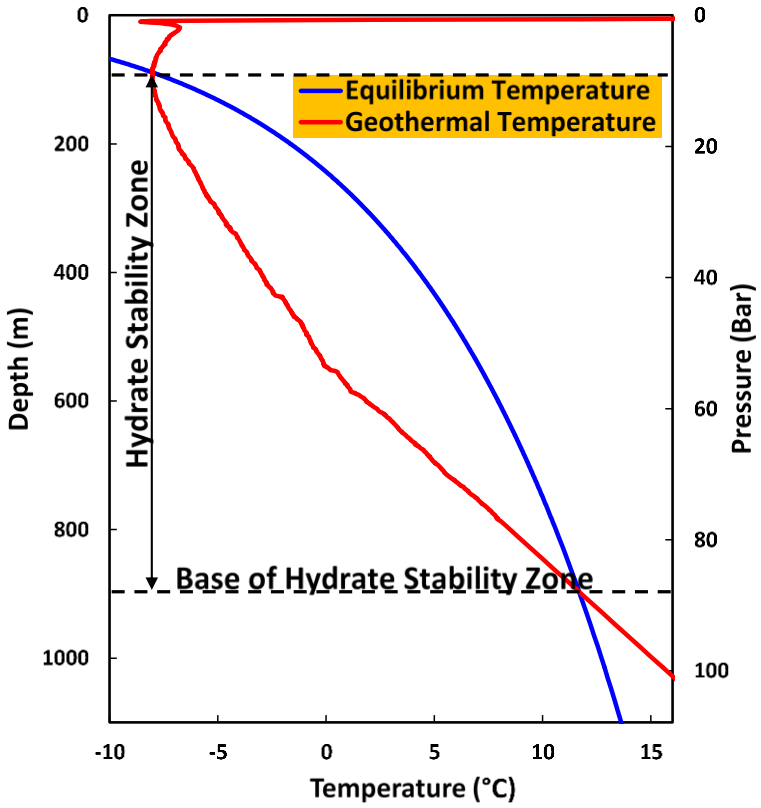

Figure 1-2: Thermodynamic phase diagram showing the region of stability for Prudhoe Bay Unit hydrates

1.1.3 Hydrates in nature

Gas hydrates are found throughout the world on every continent. They are mainly present off the coasts on the continental margins and below the permafrost. Figure 1-3 shows a map of known and inferred hydrate deposits worldwide[9].

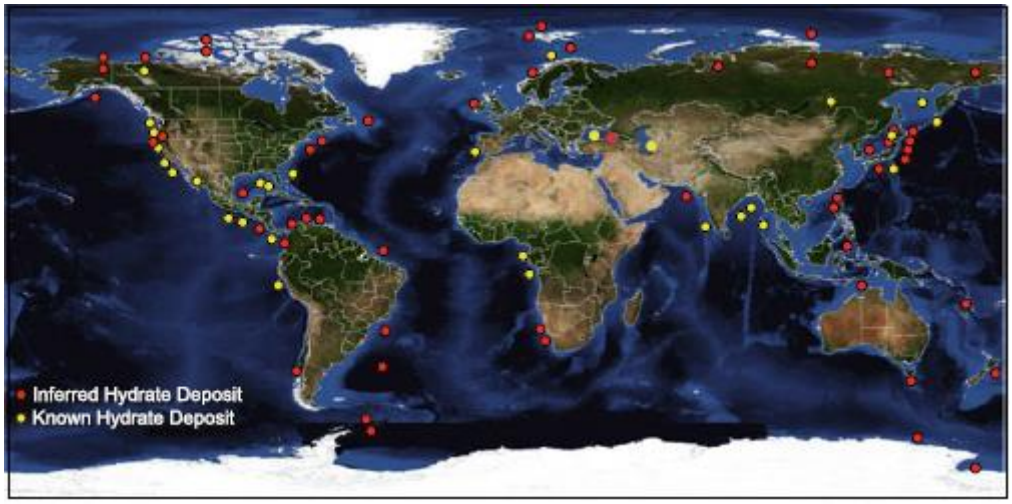

Figure 1-3: Worldwide occurrences of gas hydrates[9]

In nature, gas hydrates occur both in the permafrost regions and in the marine sediments in the oceans and deep lakes where pressure-temperature conditions are suitable and where sufficient methane is delivered to the zone of hydrate stability in the uppermost sediments. Naturally occurring methane hydrates can be found in both terrestrial and marine environments. Terrestrial deposits have been found in polar regions, hosted in sediments within and beneath the permafrost, while marine occurrences have been found mainly in sediments of the earth's outer continental margins.

Based on the fact that most naturally occurring gas hydrates are methane hydrates[10], it is possible to estimate the upper bound to the depths within which gas hydrates occur in nature, by defining a global hydrate stability zone (GHSZ). From this estimate, most of the permafrost would

be in the GHSZ, where an increase in the depth of base of permafrost would increase the depth of the GHSZ. A more accurate estimate for the actual occurrence of natural gas hydrates involves the determination of areas with biogenic or thermogenic source of gas, which provide adequate amount of methane needed in the pore water to form hydrates. The available methane concentration must be higher than its solubility in water.

Biogenic methane is produced as a common by-product of bacterial ingestion of organic matter in a process known as ***biogenesis***. They are produced in swamps and buried sediments and are considered the most dominant source of the methane trapped in hydrate accumulations in shallow sediments beneath the permafrost such as those found in the Alaska North Slope (ANS). The biogenesis process selectively produces methane and this is why ANS hydrate deposits are assumed to be pure methane hydrates.

Thermogenic methane, on the other hand, is produced from deeply buried organic-rich beds under very extreme condition of high temperature and pressure over a long period of time in a process called catagenesis. Thermogenic methane is the primary source of methane in conventional gas reservoirs. However, unlike the biogenesis process, catagenesis also creates high concentrations of heavier hydrocarbons such as ethane, propane, and butanes. Due to the fact that thermogenic methane is produced in areas much deeper than the base of hydrate stability zone (BHSZ), hydrates formed from thermogenic methane are far less common than biogenic methane.

Owing to the kinetics of the formation process of the hydrate-forming gas in situ, gas availability becomes the limiting factor for the natural occurrence of hydrates and usually determines the extent of a hydrated reservoir.

1.2 Energy Potential of Hydrates

The energy potential of hydrates is evident from the fact that they can store up to 164 times the volume of methane gas at STP and studies conducted by many investigators have indicated that commercial quantities of methane are trapped in naturally occurring gas hydrates. The nature of hydrate deposits and the quality of the reservoir are the primary technical factors which are indices of recoverability of methane from a hydrated reservoir [11]. Therefore, a clear identification of a hydrate deposit that can be considered as an "energy resource" becomes very central to evaluating their recovery potential. Moridis and Collett[12] developed a classification system for hydrate deposits in which each class of reservoir is associated with their gas recovery potential.

Class 1 reservoirs are characterized by an underlying two-phase fluid zone with a mobile gas phase in which the base of the hydrate bearing sand (HBS) is exactly at the BHSZ. The thermodynamic proximity to hydrate equilibrium, combined with the fact that the underlying mobile gas phase is an excellent target for the onset of recovery by depressurization, makes class 1 the most desirable for exploitation.[12] In Class 2 reservoirs, the HBS is underlain by a free (mobile) water zone with no free gas while Class 3 hydrate deposits are typified by the absence of underlying mobile fluids. Both Class 2 and 3 accumulations can have the HBS situated well above the BHSZ, which may exist under stable or equilibrium conditions. In addition to thermodynamic proximity of the HBS to hydrate equilibrium, recovery from Class 2 and 3 is more dependent on other factors including the initial reservoir condition, environmental issues and economic implications (Moridis et al, 2004; Moridis, 2004). Class 4 hydrate reservoirs, typically found in marine sediments, are characterized with low hydrate saturations and, therefore, production rates from this class are expected to be lower that economic limits as predicted by reservoir simulations.[13] Ultimately, the economic feasibility of production from gas hydrate deposits will be

significantly influenced by its proximity to already existing infrastructure for conventional oil and gas[12].

1.3 Gas Recovery Techniques

Gas recovery techniques from hydrates are based on its stability criteria with the primary objective of making it unstable in a process known as hydrate dissociation. Dissociation of hydrates can be accomplished by:

- Pressure Reduction (Depressurization)
- Formation Heating (Thermal Stimulation)
- Equilibrium Shifting (Hydrate Inhibition)
- Novel techniques e.g. CH_4-CO_2 exchange (CO2 Sequestration)

In the depressurization method, the reservoir pressure is lowered outside the pressure-temperature stability region, which induces hydrate dissociation. This method has been assessed to be the simplest, cheapest and the most efficient single method to recover gas from hydrates[14] and is most effective in a Class 1 reservoir (as discussed in the previous section). The endothermic nature of hydrate dissociation coupled with additional cooling due to Joule-Thomson effects at the wellbore perforations, cause depressurization to be accompanied by a decrease in reservoir temperature. When the reservoir temperature becomes low enough, pressure-temperature condition in the reservoir may begin to favor hydrate stability, hence increasing the risk of secondary formation of hydrates or ice in the reservoir. An adequate control of the depressurization rate or heating of the well bore would reduce or eliminate these risks. The severity of the reformation of hydrates in the reservoir on gas production has been extensively studied by many researchers using predictions from simplistic reservoir models[15-22], and is one of the focal points of discussion in this work.

The thermal stimulation method requires a heat source to increase the formation temperature and, thereby, destabilizing the hydrate. The required heat may be provided by the injection of hot fluids (e.g steam), direct electrical heating or heat recovery of the neighboring conventional oil and gas operations. Injection of hot fluids can be done using a single well or multiple wells. Due to the amount of energy required to heat up the hydrate bearing rock of the target hydrate zone, thermal stimulation may be too expensive to be efficient, as indicated by the results of the 2002 Mallik Production Tests and corroborated by previous reservoir simulation studies[19, 23, 24]. However, the method can be used as a recovery enhancement to supplement a primary recovery technique such as depressurization.

Inhibitors can dissociate gas hydrates by causing the equilibrium curve to shift to the left, thereby, narrowing the stability region of the hydrate. They are usually combined with one or both of depressurization and thermal stimulation. Methanol, glycols and halides are examples of inhibitors which can be used. A significant concern about the use of inhibitors, is the environmental impact they may have. The tendency of the dissociating high water content hydrates to dilute inhibitors requires that the inhibitors be fed into the reservoir at sufficient concentrations. This heavy requirement of large inhibitor consumption increases the risks of corrosion and cost of production and, hence, leaves a very big question about the economic viability of the recovery technique.

Gas-methane exchange is a technique which involves using a gas whose molecules have a higher affinity to form hydrates than methane to displace the methane molecule from the hydrate-water cavity. For example, CO_2 can be used to displace methane from methane hydrates while being trapped as CO_2 hydrate in situ. A “proof of concept” for this recovery technique was demonstrated in a field production trial conducted at the Ignik-Sikumi well of the ANS Prudhoe

Bay oilfield during the Spring of 2012 [25]. In a "huff and puff" cycle, a 14 day continuous injection of a 23/77 molar ratio of CO_2/N_2 mixture was followed by a 28-day production by depressurization. Test data indicated that CO_2-CH_4 exchange did occur and history matching of the results from the test was performed to improve model predictions by hydrate reservoir simulator codes (Garapati, 2013). One huge advantage of this method is the simultaneous sequestration of the CO_2 (a greenhouse gas), as methane is being produced. Furthermore, the CO_2 hydrate formed in situ will preserve the integrity of the hydrate-bearing rock and therefore reduce risks and concerns about possible geomechanical failure due to methane hydrate dissociation.

1.4 Flow Assurance

Hammerschmidt (1934) embarked on an investigation to understand the nature of the ice-like substance blocking gas transmission lines frequently at temperatures above the freezing point of water, and later identified it as hydrate. Before this period, the subject of hydrates had always been an academic discourse and the possibility of their occurrence outside the laboratory had not been anticipated. Hammerschmidt's discovery quickly led to a more intensified interest in gas hydrates because of the economic implications of pipeline blockages in the oil and gas industry.

Blockage, due to secondary formation of hydrates, can also occur in the wellbore during production from hydrate reservoirs. The requirement of low well flowing bottom-hole pressures (BHP) during production by depressurization would necessitate the use of an artificial lift system (pump) to ensure that produced fluids reach the wellhead. The high pressure which would be supplied by the pump to move cold fluids up within a well surrounded by a cold reservoir would increase the risk of reformation and growth of hydrates in the wellbore as production progresses. During the Ignik Sikumi field trial, hydrates were confirmed to have formed within wellbore when pressures became high enough, which led to operational difficulties and occasional shutdowns.[25]

Therefore, wellbore conditions including temperature, pressure and solids control need to be managed effectively in order to forestall flow assurance issues during hydrate production.

1.5 Motivation and Scope of Work

The focus of natural gas hydrate research worldwide has since shifted from assessment of quantity of reserves to production. Research on hydrate production has also moved from laboratory scale to field scale. In the year 2000, the Methane Hydrate Research and Development Act was established to support the U.S national hydrate research program whose primary goal is to determine the economic viability of developing gas hydrates as an energy resource. Since the inception of the methane hydrate program, the U.S. Department of Energy (DOE) has made huge investments (over $100,000,000) on natural gas hydrate exploration projects which included two short-term production tests on the Alaska North Slope (ANS). The first project, carried out in February 2007, was an extensive data collection collaborative effort by the DOE, BP Exploration (Alaska), Inc. (BPXA) and the U.S. Geological Survey (USGS) at the Mt. Elbert Well located in the Milne Point Unit (MPU) of the ANS. The second project was a field production trial using the CH_4-CO_2 exchange technique at the Ignik Sikumi well located in the Prudhoe Bay Unit of the ANS. It was a joint effort led by DOE and Japan Oil Gas and Metals National Corporation (JOGMEC) and executed by ConocoPhillips. International drilling programs include the Malik Gas Hydrate Production Test at Mckenzie Delta, Canada (2002, 2007-2008) and Japanese Production Test at the Nankai Trough, Japan (2013-2015). Significant investments and contributions to hydrate exploration have also been made by China, South Korea and India. The objectives of these programs culminate into demonstrating the technical feasibility of producing methane hydrates through long term production tests. As of now, the ANS is the most promising

and available hydrate production test site in the U.S., where the State of Alaska has reserved unleased state lands in the PBU vicinity for a potential long-term hydrate tests[26].

There are continued efforts by the DOE, USGS and other international organization to build and develop the scientific foundation for establishing gas hydrates as a critical energy resource. These organizations have been involved in the significant advancements of gas hydrate production computer simulators for more than a decade. Recently, the DOE and USGS embarked on project under the International Code Comparison Group to conduct numerical gas hydrate production simulations for idealized scenarios of the ANS hydrate deposits[27, 28]. The project was aimed at establishing confidence in reservoir model predictions by sharing knowledge and cross validating results from various simulators. Like in most published hydrate reservoir modeling efforts, these idealized scenarios are a simplistic geological and geophysical representation based on the assumption of reservoir homogeneity. While first order predictions are obtained from these simplified models, it has been shown that the degree of reservoir heterogeneity can significantly affect the quantitative and qualitative results obtained from homogeneous models.[20, 29, 30]

Therefore, there is a need for continuous and advanced modeling and analysis to accurately and more realistically determine energy parameters related to the production potential of hydrate accumulations in an actual geological setting. This need forms the primary motivation for this work.

1.5.1 Overall Thesis Objectives

The main goal of this study is to obtain an advanced assessment of the gas recovery potential of the hydrate bearing sediments of the ANS permafrost. To obtain a more realistic evaluation, results from a data driven reservoir characterization must be incorporated into mathematical reservoir flow simulation models.

More explicitly, the objectives of this study are to:

- Characterize hydrate reservoirs of the ANS in order to develop field-scale heterogeneous 3D representative models of the ANS hydrate deposits
- Investigate the effectiveness of depressurization as a gas recovery technique from gas hydrates of the ANS simulations to support long-term production tests and subsequent field development.
- Identify the key parameters which influence model performance
- Provide a clear understanding on the phenomenon of secondary hydrate formation in the reservoir
- Investigate the effect of reservoir pressure and temperature on gas rate profiles and cumulative production in order to determine suitable well locations and designs.
- Design and couple multiphase wellbore with reservoir models to forestall any flow assurance issues such as secondary hydrate formation
- Recommend production design for long-term development

The two main study areas are the hydrate deposits of PBU ("L-Pad") and MPU (Mount Elbert). All models developed in this work are based on depressurization as a primary recovery method. Methods involving thermal stimulation, use of chemical inhibitors and gas molecule exchange are not studied.

References

1. Davy, H.P., Trans. Roy. Soc. London, 1811. **101**(1).

2. Priestley, J., *Experiments and observations on different kinds of air*. 1775.

3. Wroblewski, S., *On the combination of carbonic acid and water.* Acad. Sci. Paris, Comptes rendus, 1882. **94**: p. 212-213.

4. Max, M.D., *Natural gas hydrate in oceanic and permafrost environments*. Vol. 5. 2003: Springer.

5. Hammerschmidt, E., *Formation of gas hydrates in natural gas transmission lines.* Industrial & Engineering Chemistry, 1934. **26**(8): p. 851-855.

6. Ripmeester, J.A., John, S.T., Ratcliffe, C.I., and Powell, B.M., *A new clathrate hydrate structure.* Nature, 1987. **325**(6100): p. 135-136.

7. Sloan, E.D. and Koh, C., *Clathrate hydrates of natural gases*. 2007: CRC press.

8. Circone, S., Kirby, S.H., and Stern, L.A., *Direct measurement of methane hydrate composition along the hydrate equilibrium boundary.* The Journal of Physical Chemistry B, 2005. **109**(19): p. 9468-9475.

9. Giavarini, C. and Hester, K., *Gas hydrates: Immense energy potential and environmental challenges*. 2011: Springer.

10. Kvenvolden, K.A. and Lorenson, T.D., *The global occurrence of natural gas hydrate*, in *Natural gas hydrates: Occurrence, distribution, and detection*. 2001, American Geophysical Union. p. 3-18.

11. Collett, T.S., *Energy resource potential of natural gas hydrates.* AAPG bulletin, 2002. **86**(11): p. 1971-1992.

12. Moridis, G.J. and Collett, T.S., *Gas production from class 1 hydrate accumulations*, in *Advances in the study of gas hydrates*, C. Taylor and J. Kwan, Editors. 2004, Springer US. p. 83-97.

13. Moridis, G.J. and Sloan, E.D., *Gas production potential of disperse low-saturation hydrate accumulations in oceanic sediments.* Energy Conversion and Management, 2007. **48**(6): p. 1834-1849.

14. Pooladi-Darvish, M. and Hong, H., *Effect of conductive and convective heat flow on gas production from natural hydrates by depressurization*, in *Advances in the study of gas hydrates*, C. Taylor and J. Kwan, Editors. 2004, Springer US. p. 43-65.

15. Moridis, G.J., Kowalsky, M.B., and Pruess, K., *Depressurization-induced gas production from class-1 hydrate deposits.* SPE Reservoir Evaluation & Engineering, 2007. **10**(05): p. 458-481.

16. Moridis, G. and Reagan, T., *Strategies for gas production from oceanic class 3 hydrate accumulations, paper otc 18865 presented at the offshore technology conference.* Am. Assoc. of Pet. Geol., Houston, Tex, 2007. **30**.

17. Reagan, M., Moridis, G.J., and Zhang, K., *Sensitivity analysis of gas production from class 2 and class 3 hydrate deposits*, in *2008 Offshore Technology Conference*. 2008: Houston, Texas, USA.

18. Anderson, B.J., Wilder, J.W., Kurihara, M., White, M.D., Moridis, G.J., Wilson, S.J., Pooladi-Darvish, M., Masuda, Y., Collett, T.S., and Hunter, R. *Analysis of modular dynamic formation test results from the mount elbert 01 stratigraphic test well, milne point unit, north slope, alaska*. in *6th International Conference on Gas Hydrates (ICGH 2008)*. 2008. Vancouver, British Columbia, Canada.

19. Kurihara, M., Funatsu, K., Ouchi, H., Masuda, Y., Yasuda, M., Yamamoto, K., Numasawa, M., Fujii, T., Narita, H., and Dallimore, S.R., eds. *Analysis of the jogmec/nrcan/aurora mallik gas hydrate production test through numerical simulation*. Scientific results from the mallik 2002 gas hydrate production research well program, mackenzie delta, northwest territories, canada, ed. S.R. Dallimore and T.S. Collett. Vol. 585. 2008, Geological Survey of Canada, Bulletin.

20. Myshakin, E.M., Anderson, B.J., Rose, K., and Boswell, R., *Simulations of variable bottomhole pressure regimes to improve production from the double-unit mount elbert, milne point unit, north slope alaska hydrate deposit.* Energy & Fuels, 2011. **25**(3): p. 1077-1091.

21. Li, X.-S., Li, B., Li, G., and Yang, B., *Numerical simulation of gas production potential from permafrost hydrate deposits by huff and puff method in a single horizontal well in qilian mountain, qinghai province.* Energy, 2012. **40**(1): p. 59-75.

22. Li, X.-S., Yang, B., Li, G., and Li, B., *Numerical simulation of gas production from natural gas hydrate using a single horizontal well by depressurization in qilian mountain permafrost.* Industrial & Engineering Chemistry Research, 2012. **51**(11): p. 4424-4432.

23. Hancock, S., Collett, T., Dallimore, S., Satoh, T., Inoue, T., Huenges, E., Henninges, J., and Weatherill, B., eds. *Overview of thermal-stimulation production-test results for the japex/jnoc/gsc et al. Mallik 5l-38 gas hydrate production research well*. Scientific results from the mallik 2002 gas hydrate production research well program, mackenzie delta, northwest territories, canada, ed. S.R. Dallimore and T.S. Collett. Vol. 585. 2005, Geological Survey of Canada, Bulletin. 135.

24. Moridis, G.J., Collett, T.S., Dallimore, S.R., Inoue, T., and Mroz, T., eds. *Analysis and interpretation of the thermal test of gas hydrate dissociation in the japex/jnoc/gsc et al. Mallik 5l-38 gas hydrate production research well*. Scientific results from the mallik 2002

gas hydrate production research well program, mackenzie delta, northwest territories, canada, ed. S.R. Dallimore and T.S. Collett. Vol. 585. 2005, Geological Survey of Canada, Bulletin.

25. Schoderbek, D., Farrell, H., Hester, K., Howard, J., Raterman, K., Silpngarmlert, S., Martin, K.L., Smith, B., and Klein, P., *Conocophillips gas hydrate production test final technical report*. 2013.

26. Flemings, P.B. and Kastnert, M., *Recommendations to secretary of energy*, M.H.A. Committee, Editor. 2014.

27. Wilder, J.W., Moridis, G.J., Wilson, S.J., Kurihara, M., White, M.D., Masuda, Y., Anderson, B.J., Collett, T.S., Hunter, R.B., and Narita, H., *An international effort to compare gas hydrate reservoir simulators*, in *Proceedings of the 6th International Conference on Gas Hydrates (ICGH 2008)*. 2008: Vancouver, CANADA.

28. Gaddipati, M., *Code comparison of methane hydrate reservoir simulators using cmg stars*. 2008: West Virginia University.

29. Anderson, B.J., Kurihara, M., White, M.D., Moridis, G.J., Wilson, S.J., Pooladi-Darvish, M., Gaddipati, M., Masuda, Y., Collett, T.S., and Hunter, R.B., *Regional long-term production modeling from a single well test, mount elbert gas hydrate stratigraphic test well, alaska north slope.* Marine and petroleum geology, 2011. **28**(2): p. 493-501.

30. Reagan, M.T., *The effect of reservoir heterogeneity on gas production from hydrate accumulations in the permafrost.* Lawrence Berkeley National Laboratory, 2010.

2. Theoretical Background

2.1 Evolution of Hydrate Phase Equilibrium Prediction

Hammerschmidt[1] published a correlation of over 100 hydrate formation pressure-temperature points. Other early efforts to predict the formation of hydrates include the works of Wilcox et al[2] and Katz.[3] Wilcox et al defined vapor-hydrate distribution coefficients (K_{vsi} values) for hydrates and developed a method to predict hydrate formation conditions in a method directly analogous to the stand vapor-liquid dew point calculations, leading to publication of K_{vsi} charts for CH_4, C_2H_6, C_3H_8, H_2S and CO_2. Robinson and Ng[4] presented a similar chart for i-C_4H_{10} while Poettmann[5] published a chart for n-C_4H_{10}. Katz[3] developed a very simple method based on gas-gravity, where different pressure-temperature hydrate formation conditions were predicted for gases with different specific gravities. While these methods are very simple, they only provide initial estimates and qualitative understanding of the hydrate phase equilibria.

Recent efforts to predict hydrate formation conditions include those developed following the fundamental principles of statistical thermodynamics and equations of state. They are both more comprehensive and accurate, and provide the link between the molecular structures of hydrates and their measurable thermodynamic properties (e.g. pressure, temperature and density). The foundation of this new generation of thermodynamic models can be traced back to the work of Barrer and Stuart.[6] Their work was later modified by van der Waals and Platteeuw[7] based on the definition of a Langmuir constant and its relation to guest-host potential parameters.

Ballard[8] expanded on the work of van der Waals and Platteeuw by defining the hydrate fugacity and some reference parameters and derived equations to calculate the fugacity of water in hydrates. Ballard's work also included an extension of the work of Gupta[9], which is based on the minimization of the Gibbs free energy. The Gibbs free energy method allows for calculations

of formation conditions of the hydrate and the calculation of all the phases present at any temperature and pressure regardless of the presence of the hydrate phase.

The increase in the availability of high performance computers is continually strengthening the applicability of computer simulation techniques which have been shown to yield significant improvements over earlier methods. Molecular Dynamics (MD) and Monte Carlo (MC) simulations are the most common computer based techniques. MD involves using an accurate water potential function to solve Newton's equation of motion for small number of molecules over time. An integration of these intermolecular forces over several time-steps would yield to the evaluation of the macroscopic properties of hydrates.[10]

Another computer simulation technique includes the ab initio methods or quantum mechanics, where efforts have been made to calculate potentials between atoms and molecules in hydrates. Among the notable works describing these methods are Cao[11], Klauda[12] and Anderson[13], which have provided significant improvements on the works of van der Waals and Plateeuw.

2.2 Hydrate Dissociation Models

The dissociation process requires external energy (known as the enthalpy of dissociation) to break the bonds in the hydrate structure, that would lead to the liberation of the trapped methane molecule in the crystal lattice and produce the associated water. Hence, hydrate dissociation is an endothermic process.

The mechanisms that control hydrate dissociation can be explained by the annotated phase diagram shown for a depressurization process in Figure 2-1. The overall process is initiated by a reduced pressure constraint which is held constant at P_5 (e.g. a BHP of a production well at some location in a hydrated reservoir). In the first step (I), P_1 is reduced at constant temperature T_1 to the equilibrium pressure at T_1, P_2.

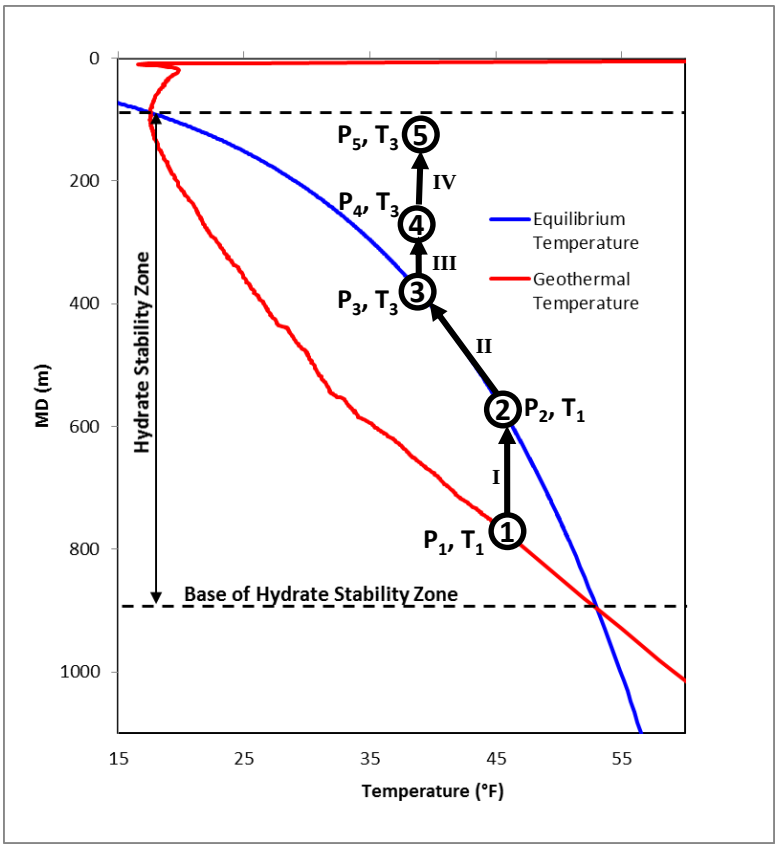

Figure 2-1: Hydrate dissociation process with depressurization

The driving force for this step is $P_1 - P_2$. The second step (II) is the onset of the endothermic phase change occurring at equilibrium, where a $+\Delta H$ is absorbed and T_1 decreases to T_3 (the equilibrium temperature at P_3), as pressure reduces from P_2 to P_3. The temperature difference T_1-T_3, which is a measure of the sensible heat available for **heat transfer** from the undissociated part of the reservoir (hence the magnitude of $+\Delta H$ that can be provided to break the hydrate bonds) is the driving force for this step. Stage 3 marks an onset of the evolution of a gas phase from the hydrate phase and step III is governed by **intrinsic rate kinetics** whose driving force is the difference in the fugacity of the gas molecule in the hydrate phase and its fugacity in the gas phase. The last step (IV) is the **fluid flow** from the hydrate/gas phase boundary to the bulk gas phase at P_5 (e.g. gas flow to the well), with a driving force of $P_4 - P_5$.

Researchers[14, 15] have shown that hydrate dissociation process can be mainly driven or controlled by any combination of heat transfer, intrinsic rate kinetics and fluid flow. Hydrate dissociation models are classified according to the importance of these three phenomena.

2.2.1 Equilibrium Model

In the equilibrium model, dissociation is considered to occur instantaneously with heat transfer as the rate-limiting process. In a heat transfer controlled dissociation, the sharp drop in temperature at the shrinking hydrate phase boundary caused by the endothermic nature of hydrate decomposition creates a temperature gradient, and the sensible heat from the remaining part of the reservoir provides the energy which drives the rest of the dissociation process. For the case of pure methane hydrates, the endothermic dissociation reaction is [16]:

$$CH_4.N_H H_2O_{(h)} \rightarrow CH_{4(g)} + N_H.H_2O_{(w)} \quad (2\text{-}1)$$

N_H is the hydration number (typically ~ 6, for methane). The equilibrium model is based on the assumption that Equation (2-1) occurs at chemical equilibrium, so that the hydrate will liberate a stoichiometric quantity of gas spontaneously as soon as the hydrate reservoir pressure and temperature (P, T) conditions reach the equilibrium values (P_e, T_e) defined by the hydrate phase equilibrium relationship. With methane and water as the only components, the equilibrium model considers heat transfer among four phases namely:

- Gas phase whose components are methane and water vapor
- Aqueous phase whose components are water and dissolved methane
- Solid ice phase which contains only water
- Solid hydrate phase which contains methane and water

In the equilibrium model, the surrounding gas at the interface is assumed to always be at thermodynamic equilibrium with the hydrate. Heat transfer could be achieved via conduction,

convection or both. Using a 1-D domain, Hong et al[15] used an analytic procedure to describe the relationship between sensible heat (or ΔT) and rate of hydrate dissociation in a heat transfer controlled hydrate dissociation. It was shown that the evolution of temperature in the hydrate phase can be obtained following a similar solution approach to the melting moving boundary problem [17].

$$T(x,t) = T_i - (T_i - T_e)\frac{erfc\left(\frac{x}{2\sqrt{\alpha t}}\right)}{erfc(\lambda)} \tag{2-2}$$

where,

$$X(t) = 2\lambda\sqrt{\alpha t} \tag{2-3}$$

i.e. location of the hydrate interface as the hydrate dissociates. λ is the solution of the equation:

$$\lambda e^{\lambda} erfc(\lambda) = \frac{Ste}{\sqrt{\pi}} \tag{2-4}$$

Ste is the Stefan number, a dimensionless quantity which drives the dissociation process [15] and is defined as:

$$Ste = \frac{c_p(T_i - T_e)}{\phi \Delta H}\frac{\rho}{\rho_H} \tag{2-5}$$

where,

t = time (s)

T_i = Initial hydrate temperature (K)

T_e = Equilibrium hydrate dissociation temperature (K)

α = Average thermal diffusivity of the hydrate medium (m^2/s)

c_p = Average heat capacity of the hydrate medium , J/kg/K

ϕ = Porosity of hydrate medium

ΔH = Heat of dissociation of hydrate (J/kg hydrate)

ρ = Average density of the hydrate medium (kg/m^3)

ρ_H = Density of hydrate (kg/m^3)

In porous media, Stefan number can be used as an preliminary indication of how much recovery can be achieved under adiabatic conditions, based on reservoir temperature alone. The product of the porosity and interface velocity is a measure of rate of hydrate dissociation [15] obtained from the differentiation of Equation (2-3), the interface velocity is given by

$$\frac{dX(t)}{dt} = \lambda\sqrt{\frac{\alpha}{t}} \tag{2-6}$$

Equation (2-6) clearly shows the proportional dependence of dissociation rate on *Ste* and, therefore, on ΔT.

It has been shown that the rate of hydrate dissociation is mainly controlled by heat transfer in hydrate dissociation processes occurring over a reservoir production time scale [15, 18]. This is why in many hydrate reservoir simulators, the hydrate dissociation process is fairly approximated with the equilibrium model, which is computationally less expensive than the more complex kinetic model. It is to be noted however, that the effects of intrinsic rate kinetics may become very significant at shorter time scales especially at the onset of hydrate dissociation. [15, 19]

2.2.2 Kinetic Model

A kinetic model accounts for the phase changes and transitions are determined by a kinetic rate of dissociation or formation given by [20]:

$$\dot{m} = k_d^0 exp(-\Delta E/RT) F_a A_d (p_e - p_g) \tag{2-7}$$

where,

$\dot{m}$ = Mass rate of hydrate dissociation

k_d^0 = Intrinsic dissociation rate constant independent of temperature and pressure

ΔE = Change in activation energy for the dissociation reaction

R = Universal gas constant

T = Temperature of Hydrate

A = Hydrate surface area of decomposition

F_a = Adjustment factor, for reaction surface area corrections

p_e = Hydrate equilibrium pressure at T

p_g = pressure in bulk gas

Equation (2-7) is a statement of the direct proportionality relationship between the rate of hydrate dissociation to the product of the rate constant and the dissociation surface area. Unlike the equilibrium model, a kinetic model considers hydrate as a third component composed only of $CH_4.N_HH_2O$ rather than separate methane and water components.

While the kinetic rate model is more accurate for short dissociation times, it is computationally more intensive. In order to improve on kinetics-based dissociation models, there is need to incorporate nucleation phenomena and the tendencies of hydrate reformation.[19] However, based on current knowledge, in order for kinetics to be important, the kinetic rate constant would have to be reduced by more than 2–3 orders of magnitude.[15]

2.2.3 Effect of Fluid Flow

According to preliminary studies, it is very unlikely that hydrate dissociation rates would be controlled by fluid flow, however, the effect of fluid flow in the reservoir can become significant if fluid flow paths are considerably long enough[15]. Furthermore, fluid flow would have more effect in reservoirs with low formation porosity or permeability.[18, 21 22]

2.3 Numerical Solution with CMG STARS

The complexity of the mass and energy conservation equations of fluid flow in porous media often makes the applicability of analytical (or closed form) solution techniques impracticable in real-life problems. As a result, this has given rise to the development of various numerical solution methods for hydrate dissociation in porous media, executable by computer program codes embedded in reservoir simulators. Although commercial made-for-hydrate reservoir simulators for hydrates are not yet available, the existing simulators include:

- TOUGH + HYDRATE,[23] developed at the DOE's Lawrence Berkely National Laboratory
- MH-21 HYDRES,[24] a product of Japan's Methane Hydrate R&D Program developed by the National Institute of Advanced industrial Science and Technology, Japan Oil Engineering Co., Ltd.
- STOMP-HYD, developed by Pacific Northwest National Laboratory[25]
- HydrateResSim,[26] developed at the DOE's National Energy Technology Laboratory
- CMG STARS[27], developed by the Computer Modelling Group, Canada.

STARS is a commercial reservoir simulator built for conventional thermal reservoir flow simulations[27]. The choice of STARS as the numerical simulator for all the models presented in this work is based on its well-established and advanced numerical techniques and, hence, its capability of modeling a reservoir with a very complex geometry with high degree of heterogeneity of geophysical properties, compared with the other built-for-purpose hydrate reservoir simulators.
In order to gain confidence in simulation predictions by all of these simulators, efforts were made by the USGS and DOE in collaboration with international organizations to reach consensus between these codes. This was the objective of the International Gas Hydrate Code Comparison Project which involved studies conducted on idealized problems. The performance of this study

using CMG STARS was the main subject discussed in the MSc thesis of Gaddipati[28], in which a close agreement with other codes was confirmed. A more detailed results of the project is documented in a comprehensive report by Wilder et al.[29]

2.3.1 Hydrate Dissociation and Formation Models

In STARS, hydrate is modeled as a separate and only component of a highly component of a highly viscous "black oil" phase.[28-30] A summary of all the components and phases are given in Table 2-1. The hydrate dissociation and formation processes are based on an equilibrium model approximated by intrinsic rate kinetics, as in the following discussion.

Table 2-1: Components and phases in hydrate dissociation modeling with STARS[31]

Component	**Phase**		
	Aqueous	Gaseous	Oleic ("oil-like")
H_2O	X	X	
CH_4		X	
$CH_4.N_H\,H_2O$			X

Pure methane hydrate is assumed in this study with N_H = 6.176.[28, 30, 32] The dissociation and formation processes are represented by the two kinetic reactions in Equations (2-8) and (2-9), respectively.

$$CH_4.\,6.176\,H_2O_{(ol)} + H_2O_{(aq)} \rightarrow CH_{4(g)} + 7.176\,H_2O_{(aq)} \quad (2\text{-}8)$$

$$CH_{4(g)} + 6.176\,H_2O_{(aq)} \rightarrow CH_4.\,6.176\,H_2O_{(ol)} \quad (2\text{-}9)$$

The additional H_2O on both sides of Equation (2-8) is necessary because in STARS, the primary reacting component has to be in either one of aqueous or gaseous phases.

The rate of hydrate dissociation (in gmol/m^3/s) in a porous media can be recast from Equation (2-7) into Equation (2-10).[31]

$$-\frac{dc_H}{dt} = \frac{k_d^0 A_{HS}}{\rho_w \rho_H} \exp\left(-\frac{E}{RT}\right)(\phi S_w \rho_w)(\phi S_H \rho_H) p_e (1 - {}^1/_{K(P,T)}) \qquad (2\text{-}10)$$

where $k_d{}^0$ is the first-order intrinsic dissociation rate constant A_{HS} is the hydrate surface area of decomposition per unit volume ρ_w and ρ_H are the densities of water and methane hydrate, ϕ is the porosity of the media and S_w and S_H are the saturations of water and hydrate in the pores. E is the activation energy, R is the universal gas constant, p_e is the hydrate dissociation equilibrium pressure at temperature T and $K(P,T)$ is the three-phase (L_w-H-V) equilibrium relationship. The $K(P,T)$ function is inputted as a three-parameter correlation and is obtained by fitting a three-phase equilibrium data of water-rich liquid, hydrate and vapor of pure CH_4.

$$K(P,T) = \frac{p_e}{P} = ({}^a/_P) exp\left(\frac{b}{T-c}\right) \qquad (2\text{-}11)$$

where a, b and c are fitting parameters.

Substitution of Equation (2-11) in Equation (2-10) would yield Equation (2-12)

$$-\frac{dc_H}{dt} = A \exp\left(-\frac{E_H}{RT}\right)(\phi S_w \rho_w)(\phi S_H \rho_H)(1 - {}^1/_{K(P,T)}) \qquad (2\text{-}12)$$

where,

$A = \frac{k_d^0 A_{HS} a}{\rho_w \rho_H}$, and

$E_H = \frac{ET - bRT - cE}{(T-c)}$, the new parameter for hydrate activation energy[31].

Similarly, hydrate formation rate can be formulated and expressed as Equation (2-13).

$$\frac{dc_H}{dt} = B(1 + \phi S_H) \exp\left(-\frac{E_H}{RT}\right)(\phi S_w \rho_w)(\phi S_H \rho_H)({}^1/_{K(P,T)} - 1) \qquad (2\text{-}13)$$

$B = \frac{k_f^0 A_{HS} a}{\rho_w}$, with k_f^o being the hydrate intrinsic formation rate constant.

STARS input data for intrinsic rate parameters are summarized in Table 2-2.

Table 2-2: STARS Input Data for Intrinsic Rate Kinetics[15, 20, 31]

Parameter	Value
$k_d^o(gmol/(day.kPa.m^2))$	1.17 x 10^{15}
$k_f^o(gmol/(day.kPa.m^2))$	1.64 x 10^{11}
$A_{HS}(m^2/m^3)$	3.75 x 10^5
$a\ (kPa)$	9.03 x 10^{15}
$b\ (K)$	-7894
$c\ (\ ^oC\ /\ K)$	-273.15 / 0
$E(J/gmol)$	81084
$R(J/gmol/K)$	8.314
$+\Delta H(J/gmol)$	51858

Values of k_d^o and k_f^o are such that the magnitude of A and B are greater than 10^{27}, and as a result, Equations (2-8) and (2-9) would occur spontaneously, essentially leading to an equilibrium model of hydrate dissociation. As mentioned earlier, the approximations of hydrate dissociation rate over a reservoir time-scale by an equilibrium model are valid, however, the inaccuracies for hydrate formation may be more significant owing to additional mechanisms such as hydrate nucleation and growth, which are not accounted for.

2.3.2 Relative Permeability and Capillary Pressure Models

Intrinsic or absolute permeability of a reservoir is a measure of its ability to flow a particular fluid at total saturation (i.e. when no other fluid is present in the reservoir pores). The ability of the rock to allow flow of a particular fluid becomes impaired in the presence of other immiscible fluids and the permeability of the reservoir to the fluid at this time is called effective permeability. The ratio of the effective permeability to the absolute permeability to a fluid is known

as relative permeability, and has been shown to be a function of the saturation of the fluid in the reservoir pores at any time.[33] Intrinsic permeability is typically a function of porosity – the relative amount of void space in a reservoir rock. Therefore, in a hydrate reservoir, the formation porosity, hence the intrinsic permeability will change continuously, as saturation of hydrate decreases or increases due to hydrate dissociation or formation in the reservoir pores.

Modeling hydrate as an oleic component in STARS makes it is impossible to explicitly include the dependency of permeability on porosity as hydrate is being dissociated or formed. However, the change in permeability is implicitly accounted for through the use relative permeability tables where values for relative permeability to water or gas are entered separately as a function of their respective saturations. In STARS and other numerical simulators, relative permeability are usually incorporated using data-fitted correlations similar to Equation (2-14), which is the modified three-phase relative permeability model of Stone.[33]

$$k_{r\alpha} = \left\{\frac{(S_\alpha - S_{\alpha ir})}{(1 - S_{\alpha ir})}\right\}^n \tag{2-14}$$

where,

$k_{r\alpha} = Relative\ permeability\ to\ \alpha\ phase$

$S_\alpha = Saturation\ of\ \alpha\ phase$

$S_{\alpha ir} = Irreducible\ saturation\ of\ \alpha\ phase$

$\alpha = w\ (water\ phase), g\ (gas\ phase); n = fitting\ exponent, typically\ in\ the\ range\ 3 - 5$

Irreducible water saturation is the relative amount of water which remains either clay- and/or capillary-bound to the formation pores during production. Figure 2-2 shows a typical relative permeability model curve generated for hydrate-bearing sands of the PBU L-Pad with S_{wir}= 0.10 and S_{wir} = 5.04 using Stone's model. Relative permeability to water increases from 0

to 1 while gas relative permeability decreases from 1 to 0, as water saturation increases from S_{wir} to 1 and gas saturation decreases from 0.9 to 0.

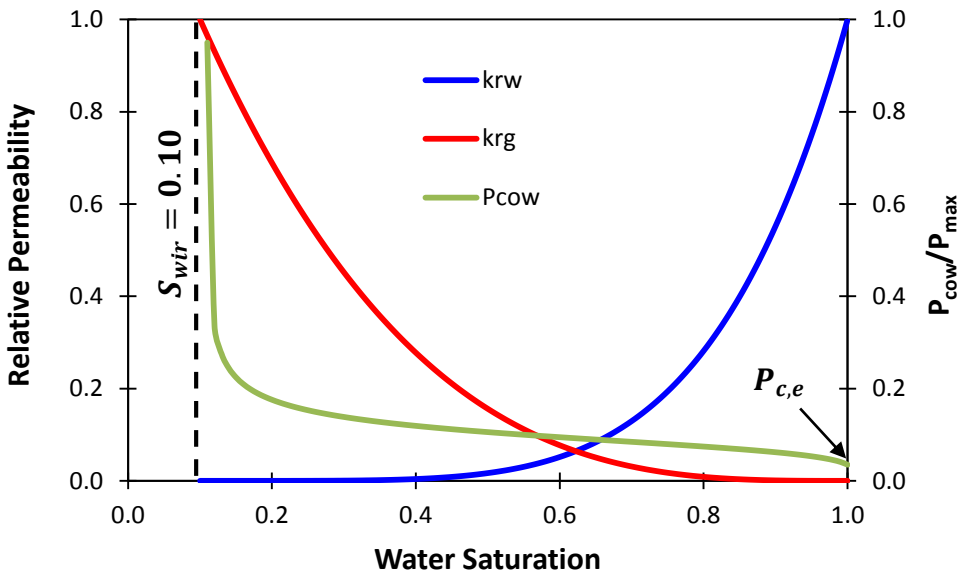

Figure 2-2: Relative permeability and capillary pressure models of PBU L-Pad hydrates

Capillary pressure exists in formation pores due to the interfacial tension between two immiscible fluids in contact with each other. It is the difference in pressures at the interface between the fluid which preferentially wets the inside of the pore (known as the "wetting phase") and the other fluid (the "non-wetting phase"). Capillary pressure can also be interpreted as the pressure required to force a non-wetting phase to displace the wetting phase in the reservoir pore in a process known as "drainage". Water is considered to be the wetting phase in most reservoirs as well as the reservoir models in this study[34] and therefore, capillary pressure is the minimum pressure required to force trapped water out of the formation pores.

Owing to the dependence of capillary pressure on pore size, capillary pressure models are typically associated with a reservoir with a particular set of pores. However, due to the complex structure of reservoir pores, capillary pressure is usually determined as a function of the saturation

of the wetting phase. The capillary pressure model used in this work is given by Equation (2-15), after van Genuchten[35].

$$P_c = -P_{max}\left[(S^*)^{-\frac{1}{\lambda}} - 1\right]^{1-\lambda} \quad (2\text{-}15)$$

where P_c= capillary pressure, $S^* = \frac{S_w - S_{wir}}{1 - S_{wir}}$, P_{max}=10 kPa, λ=0.77437 and all other variables are as defined in Equation (2-14).

The capillary pressure curve given by Equation (2-15) is also plotted as a function of water saturation in Figure 2-2, with capillary pressure expressed as a fraction of its maximum value in the reservoir (P_{max}). As water saturation decreases, the force required to eject water out of the pores (or capillary pressure) increases. However, no amount of force or capillary pressure would be high enough to reduce water saturation below the irreducible water saturation. Furthermore, the endpoint of the capillary pressure at S_w = 1 is known as the "entry pressure" ($P_{c,e}$) which is the minimum pressure required to squeeze out the wetting phase (water) from any of the reservoir pores.

2.3.3 Governing Equations

A spatially discretized form of mass and energy conservation equations are written for each component in each grid block and is given by Equations (2-16) and (2-17), respectively [27].

$$V\frac{\partial}{\partial t}\left[\phi_f\left(\rho_w S_w w_i + \rho_o S_o x_i + \rho_g S_g y_i\right)\right]$$

$$= \sum_{k=1}^{n_f}\left(\rho_w T_w w_i \Delta\emptyset_w + \rho_o T_o x_i \Delta\emptyset_o + \rho_g T_g y_i \Delta\emptyset_g\right)$$

$$+ V\sum_{k=1}^{n_r}(s'_{ki} - s_{ki})r_k \qquad (2\text{-}16)$$

$$+ \sum_{k=1}^{n_f}\left(\phi\rho_w D_{wi}\Delta w_i + \phi\rho_g D_{gi}\Delta y_i + \phi\rho_o D_{oi}\Delta x_i\right)$$

$$+ \rho_w q_{wk} w_i + \rho_o q_{ok} w_i + \rho_g q_{gk} y_i$$

$$V\frac{\partial}{\partial t}\left[\phi_f\left(\rho_w S_w U_w + \rho_o S_o U_o + \rho_g S_g U_g + (1-\varphi_f)U_r\right)\right]$$

$$= \sum_{k=1}^{n_f}\left(\rho_w T_w H_w \Delta\emptyset_w + \rho_o T_o H_o \Delta\emptyset_o + \rho_g T_g H_g \Delta\emptyset_g\right)$$

$$+ \sum_{k=1}^{n_f} K\Delta T + \rho_w q_{wk} H_w + \rho_o q_{ok} H_o + \rho_g q_{gk} H_g \qquad (2\text{-}17)$$

$$+ V\sum_{k=1}^{n_r} H_{rk} r_k + HL$$

V = Total volume of a grid block

ϕ_f = Porosity of formation grid block

S_α = Saturation of phase α, α = w,o,g (w=water, o = oil, g = gas phases)

ρ_α = Density of phase α

w_i, x_i, y_i = Mole fractions of component "i" in water, oil and gas phases, respectively

U_α, U_r = Internal energies of phase α and rock, respectively

H_α = Enthalpy of phase α

H_{rk} = Enthalpy of reaction k

r_k = Volumetric rate of reaction "k"

$q_{\alpha k}$ = Well mass flow rate of phase α

s_{ki}', s_{ki} = Product and reactant stoichiometric coefficients of "i" in reaction "k", respectively

T_α = Mass transmissibility of phase α between two regions

K = Thermal transmissibility at the interface between two regions

ΔT = Temperature drop between the nodes

$\Delta \emptyset_\alpha$ = Mass flow potential difference between the current and previous nodes

For a three-component system (water, CH_4 and hydrate), three mass (component) conservation equations, one energy conservation equation and one phase constraint equation are solved simultaneously for each grid block using the Newton-Raphson method for a system of equations given by Equation (2-18).

$$X^{k+1} = X^k - [J^k]^{-1}.R^k \tag{2-18}$$

where k is the iteration level and J^k is the Jacobian matrix of the derivatives of the residual R given by Equation (2-19).

$$R(X) = [net\ inflow\ rate] + [net\ source/sink\ rate]\ -\ [rate\ of\ accumulation] \tag{2-19}$$

Solution convergence requires that both $X^{k+1} - X^k$ and R are sufficiently small.

2.4 Geostatistics

Reservoir characterization often requires the application of statistical principles to predict the distribution of geophysical properties in a given reservoir, which is the essential goal of a branch of study known as geostatistics. The motivation to employ geostatistical techniques stems from the need to build a high-fidelity and robust 3-D reservoir model that is consistent with

available data, which is the very foundation of the overall objective this study. Geostatistical methods are developed based on the concept of random function (or random variable) to model the associated uncertainties. Strictly speaking, distribution of reservoir properties like porosity, facies, phase saturations, etc. are not random since there is only one single true distribution of the properties. However, because it is impossible to develop a completely deterministic model to evaluate geophysical properties at every location based on the evolution of the reservoir, the validity of the treatment of sampled variables as random variables is justified.[36]

Another very important concept in geostatistical analysis is the assumption of stationarity, which defines the applicability of a model developed based on sampled data over the entire region of interest. A small region of stationarity implies a closer approximation to satisfying the requirement of stationarity while a large region very much has the tendency to violate this requirement. The L-Pad model developed in this work assumes that the region of stationarity is limited to the areal extent within which data was collected and the validity of this assumption is discussed in Chapter 3.

Following the treatment of variables as random variables within the assumption of stationarity, application of geostatistical techniques generally proceeds with the quantification of spatial relationships with the sampled variables and estimation of variable values at other unsampled locations. Variograms are often used to represent spatial relationships, and techniques like *kriging* are used to estimate values at unsampled locations, usually in combination with other conditional simulation algorithms.

2.4.1 Spatial Relationships

Geostatistics takes advantage of the fact that in a naturally occurring sediment, measurements taken within a small radius of separation tend to be similar. It attempts to account for the spatial relationship through certain correlation functions. The **variogram**, which is the most commonly used, is a measure of the variability of a quantity sampled in different locations with respect to spatial coordinates. It is a function of both the separation (or "lag") distance and direction. Mathematically, it is defined by[37]

$$\gamma(\boldsymbol{h}) = \frac{1}{2N(\boldsymbol{h})} \sum_{i=1}^{N(\boldsymbol{h})} [z(\boldsymbol{x}_i) - z(\boldsymbol{x}_i + \boldsymbol{h})]^2 \qquad (2\text{-}20)$$

where,

$\boldsymbol{h}$ = separation $vector\ between\ a\ pair\ of\ samples$ ($lag\ distance\ vector$)

$N(\boldsymbol{h})$ = $Number\ of\ sample\ pairs\ separated\ by\ \boldsymbol{h}$

$\boldsymbol{x}_i$ = $position\ vector\ of\ one\ of\ the\ i^{th}\ sample\ pair$

$z(\boldsymbol{x}i)$ = $sampled\ quantity\ with\ position\ vector\ \boldsymbol{x}_i$

($\boldsymbol{h}$) = $Variogram\ o$f all $sample\ pairs\ separated\ by\ \boldsymbol{h}$

Equation (2-20) is the equivalent of a statement that the variogram is half of the variance of the difference between two sampled values located $\boldsymbol{h}$ distance apart.

The physical interpretation of the variogram can be explained by Figure 2.3 which shows a normalized horizontal directional porosity variogram for "Unit C" of the PBU L-Pad hydrate bearing sands, calculated at a lag distance interval of ~ 70 m (with tolerance of +/- 70 m). It shows that the variability between any two sampled quantities (or the variogram) increases as the separation distance between them increases and reaches a maximum (the ***sill***) at a lag distance equal to the ***range***. Beyond this range, the variability remains the same regardless of the separation

distance between the two sampled locations. Normally, sampled variables at the same location (i.e. lag distance = 0) would have the same value (i.e variogram = 0), however structural discontinuities or measurement errors may cause γ(0) to be non-zero, leading to a ***nugget effect*** as shown in Figure 2.3. (Note that the variogram in Figure 2.3 was intentionally modeled with a nugget effect for illustration purpose only).

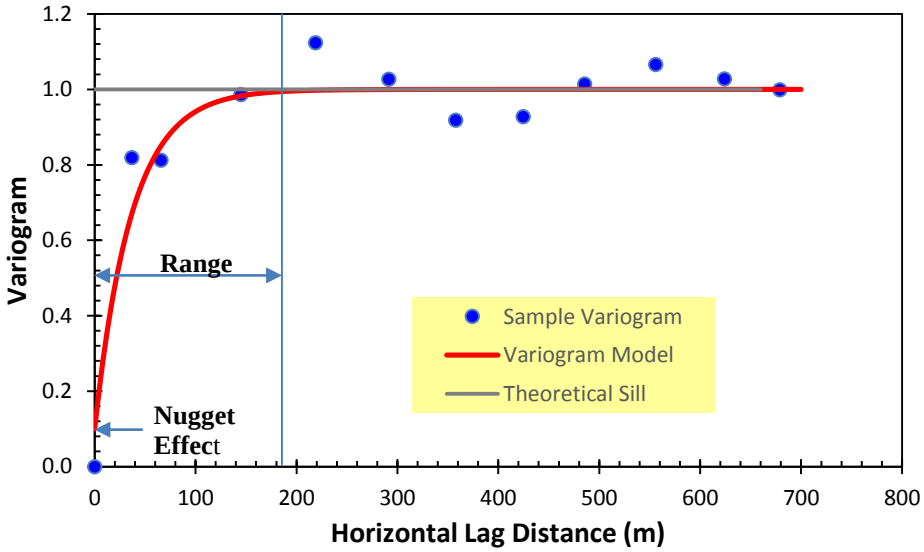

Figure 2-3: Normalized porosity variogram for "Unit C" of PBU L-Pad hydrate-bearing sands

The variogram function is required to be defined for all lag distance and directions, hence, the variogram values calculated using Equation (2-20), known as sample (or experimental) variograms, cannot be used directly in subsequent geostatistical steps. Therefore, a variogram model must be fitted to the sample variogram using any combination of known positive definite functions.[36, 38, 39] The requirement of positive definiteness of a variogram ensures that the ensuing kriging equations can be solved during stochastic simulations. Table 2-3 summarizes the most common positive definite functions that are used to model variograms.

Table 2-3: Positive Definite Variogram Models[39]

Model	**Mathematical Definition**	**Comments**
Nugget	$\gamma(h) = \begin{cases} 0, if\ h = 0 \\ 1, if\ h > 0 \end{cases}$	Models discontinuities at a scale smaller than the lag distance. Accounts for only a small fraction of the total variability.
Spherical	$\gamma(h) = \begin{cases} [1.5h - 0.5h^3], if\ h \leq 1 \\ 1, \quad if\ h \geq 1 \end{cases}$	Used to describe variograms which rise linearly before reaching the sill
Exponential	$\gamma(h) = 1 - e^{-3h}$	Similar to spherical but rises to the sill with a steeper slope
Gaussian	$\gamma(h) = 1 - e^{-3h^2}$	Models implicit continuity at short distances such as structural surfaces and thickness
Hole Effect	$\gamma(h) = 1 - \cos(h.\pi)$	Seldom used in models where data show cyclicity

where,

$$h_i = \sqrt{\left(\frac{h_{vert}}{a_{vert_i}}\right)^2 + \left(\frac{h_{hor}}{a_{hor_i}}\right)^2},\ i = 1,\ 2, \ldots N(total\ number\ of\ nested\ structures)$$

and

$h_{vert} = distance\ between\ sampled\ and\ unsampled\ points\ in\ the\ vertical\ direction$

$h_{hor} = distance\ between\ sampled\ and\ unsampled\ points\ in\ the\ horizontal\ direction$

$a_{vert_i} = variogram\ range\ in\ the\ vertical\ direction\ for\ the\ i^{th} structure$

$a_{hor_i} = variogram\ range\ in\ the\ horizontal\ direction\ for\ the\ i^{th} structure$

The final variogram model structure is a combination of these "nested structures" with each having a variance contribution that sums up to the overall (normalized) sill value of 1.

2.4.2 Stochastic Simulation

Following the development of a variogram model, it is then used to determine the weighting factors to be applied in the estimation of values in unsampled locations. This is done in a stochastic simulation process based on a set of interpolation techniques called known as ***kriging*** (developed and named by Matheron[37], after a South African mining engineer Danie G. Krige[40] who is the pioneer of the geostatistics field). Kriging involves using a minimum variance unbiased estimation technique to estimate weights, yielding a minimum error variance. Usually, the result of kriging is the expected value ("kriging mean") and variance ("kriging variance") computed for every point within a region.

In S***imple Kriging*** (SK), a value at an unsampled location is evaluated by the linear estimator

$$X^*(\vec{u}_0) = \lambda_0 + \sum_{i=1}^{n} \lambda_i X(\vec{u}_i) \tag{2-21}$$

where,

$X^*(\vec{u}_0)$ = value to be estimated at location $\vec{u}_0$, $X(\vec{u}_i)$ = value at a nearby sampled location $\vec{u}_i$ and n = total number of samples selected within a predefined search neighborhood.

In this kriging technique, there is an assumption that the population mean is known and a condition that its value at both the sampled and unsampled locations be equal (a first order stationarity requirement). Imposition of these constraints to Equation (2-21) leads to the evaluation of the constant

$$\lambda_0 = m\left(1 - \sum_{i=1}^{n} \lambda_i\right) \tag{2-22}$$

Since the weights λ_i are to be chosen such that the error variance is minimized, then

$$\boldsymbol{\Lambda} = \boldsymbol{C^{-1}c} \tag{2-23}$$

where, $\boldsymbol{\Lambda} = \begin{bmatrix} \lambda_1 \\ \lambda_2 \\ \vdots \\ \lambda_n \end{bmatrix}$, $\boldsymbol{C} = \begin{bmatrix} C(\vec{u}_1, \vec{u}_1) & \dots & C(\vec{u}_1, \vec{u}_n) \\ \vdots & & \vdots \\ C(\vec{u}_n, \vec{u}_1) & \dots & C(\vec{u}_n, \vec{u}_n) \end{bmatrix}$ and $\boldsymbol{c} = \begin{bmatrix} C(\vec{u}_1, \vec{u}_0) \\ \vdots \\ C(\vec{u}_n, \vec{u}_0) \end{bmatrix}$

$C(\vec{u}_i, \vec{u}_j)$ is the covariance between two sampled variables located at $\vec{u}_i$ and $\vec{u}_j$ and is obtained from the variogram as in Equation (2-24)

$$C(\vec{u}_i, \vec{u}_j) = 1 - \gamma(\vec{u}_i, \vec{u}_j) \tag{2-24}$$

The assumption of a known mean makes simple kriging a less popular technique compared with ***Ordinary Kriging*** (OK). The OK technique assumes that the true population mean is unknown (which is often so in practice) and therefore, the local mean within a search radius is a function of the sample location $\vec{u}_0$, i.e. there is no requirement of first order stationarity.

However, Equation (2-21) is still valid for OK with the results of the relaxation of these assumptions being:

$$\sum_{i=1}^{n} \lambda_i = 1, \text{ and } \lambda_0 = 0$$

Additionally, applying the minimum variance condition modifies Equation (2-23) to

$$\boldsymbol{\Lambda} = \begin{bmatrix} \lambda_1 \\ \lambda_2 \\ \vdots \\ \lambda_n \\ \mu \end{bmatrix}, \boldsymbol{C} = \begin{bmatrix} C(\vec{u}_1, \vec{u}_1) & \dots & C(\vec{u}_1, \vec{u}_n) & 1 \\ \vdots & & \vdots & \vdots \\ C(\vec{u}_n, \vec{u}_1) & \dots & C(\vec{u}_n, \vec{u}_n) & 1 \\ 1 & \dots & 1 & 0 \end{bmatrix} \text{ and } \boldsymbol{c} = \begin{bmatrix} C(\vec{u}_1, \vec{u}_0) \\ \vdots \\ C(\vec{u}_n, \vec{u}_0) \\ 1 \end{bmatrix}$$

where μ is a new constant called the *Lagrange parameter*.

Universal Kriging (UK) is another interpolation technique used when a trend has been observed in the data. However, because it is often a better practice to remove trends observed in data before performing geostatistical analysis, the method is not used as often as OK.[39]

One main drawback of the kriging technique is that extreme values observed in the original data are not reproduced except when such extreme value is the only sampled data present within the search radius.[36] Therefore, because of the need to preserve the variability of data in the estimated values, a conditional simulation technique is used in combination with kriging. The main idea of condition simulation techniques such as the ***Sequential Gaussian Simulation*** (SGS) is to incorporate previously simulated values as input data to estimate other values in other unsampled locations. As a result, the technique ensures that the original sample distribution is honored.

References

1. Hammerschmidt, E., *Formation of gas hydrates in natural gas transmission lines.* Industrial & Engineering Chemistry, 1934. **26**(8): p. 851-855.

2. Wilcox, W.L., Carson, D.B., and Katz, D.L., *Natural gas hydrates.* Ind. Eng. Chem., 1941. **33**: p. 662.

3. Katz, D.L., *Prediction of conditions for hydrate formation in natural gases.* Trans. AIME, 1945. **160**: p. 140-149.

4. Robinson, D.B. and Ng, H.-J., *Improve hydrate predictions.* Hydrocarbon Proc., 1975. **54**(12): p. 95-98.

5. Poettmann, F.H., *Here's butane hydrates equilibria.* Hydro. Proc., 1984. **63**(6): p. 111-112.

6. Barrer, R.M. and Stuart, W.I., *Non-stoicheiometric clathrate compounds of water.* Proceedings of the Royal Society of London A: Mathematical, Physical and Engineering Sciences, 1957. **243**(1233): p. 172-189.

7. van der Waals, J. and Platteeuw, J., *Clathrate solutions.* Adv. Chem. Phys, 1959. **2**(1): p. 1-57.

8. Ballard, A.L., Chemical, C.S.o.M.D.o., and Engineering, P.-R., *A non-ideal hydrate solid solution model for a multi-phase equilibria program*. 2002: Colorado School of Mines.

9. Gupta, A.K., *Steady state simulation of chemical processes*, in *Chemical and Petroleum Engineering*
1990, University of Calgary.

10. van der Spoel, D., Lindahl, E., van Buuren, A., Apol, E., Meulenhoff, P., Tieleman, D., Sijbers, A., Feenstra, K., and van Drunen, R., *Gromacs user manual version 3.3*. 2008.

11. Cao, Z., *Modeling of gas hydrates from first principles*, in *Chemical Engineering*. 2002, Massachusetts Institute of Technology: Massachusetts Institute of Technology.

12. Klauda, J.B., *From ab initio intermolecular potentials to predictions of macroscopic thermodynamic properties and the global distribution of gas hydrates*. 2004, University of Delaware.

13. Anderson, B., *Molecular modeling of hydrates-clathrates via ab initio, cell potential and dynamic methods*, in *Chemical Engineering*. 2005, Massachusetts Institute of Technology: Massachusetts Institute of Technology.

14. Moridis, G.J., Collett, T.S., Dallimore, S.R., Satoh, T., Hancock, S., and Weatherill, B., *Numerical studies of gas production from several ch4-hydrate zones at the mallik site, mackenzie delta, canada.* Lawrence Berkeley National Laboratory, 2002.

15. Hong, H., Pooladi-Darvish, M., and Bishnoi, P., *Analytical modelling of gas production from hydrates in porous media.* Journal of Canadian Petroleum Technology, 2003. **42**(11): p. 45-56.

16. Sloan, E.D. and Koh, C., *Clathrate hydrates of natural gases*. 2007: CRC press.

17. Ozisik, M.N., *Heat conduction*. 1993, New York: John Wiley & Sons.

18. Moridis, G.J., Seol, Y., Kneafsey, T.J., , , and *Studies of reaction kinetics of methane hydrate dissocation in porous media.* Lawrence Berkeley National Laboratory, 2005.

19. Kowalsky, M.B. and Moridis, G.J., *Comparison of kinetic and equilibrium reaction models in simulating gas hydrate behavior in porous media.* Energy Conversion and Management, 2007. **48**(6): p. 1850-1863.

20. Kim, H., Bishnoi, P., Heidemann, R., and Rizvi, S., *Kinetics of methane hydrate decomposition.* Chemical engineering science, 1987. **42**(7): p. 1645-1653.

21. Pooladi-Darvish, M. and Hong, H., *Effect of conductive and convective heat flow on gas production from natural hydrates by depressurization*, in *Advances in the study of gas hydrates*, C. Taylor and J. Kwan, Editors. 2004, Springer US. p. 43-65.

22. Howe, S.J., *Production modeling and economic evaluation of a potential gas hydrate pilot production program on the north slope of alaska*. 2004, University of Alaska Fairbanks.

23. Moridis, G., Kowalsky, M.B., and Pruess, K., *Tough+hydrate v1.0 user's manual: A code for the simulation of system behavior in hydrate-bearing geologic media*. 2008.

24. MH21, *Methane hydrate research consortium*. 2012.

25. White, M.D. and McGrail, B.P. *Stomp-hyd: A new numerical simulator for analysis of methane hydrate production from geologic formations*. in *2nd International Symposium on Gas Hydrate Technology at the 43rd Coordinating Committee for Geoscience Programmes in East and Southeast Asia (CCOP) Annual Session*. 2006. Daejeon, Republic of Korea: The Coordinating Committee for Geoscience Programmes in East and Southeast Asia (CCOP).

26. Moridis, G., Kowalsky, M., and Pruess, K., *Hydrateressim user's manual: A numerical simulator for modeling the behavior of hydrates in geologic media*. 2005.

27. CMG, *Advanced processes & thermal reservoir simulator (stars) user's guide*. 2014, Calgary, Alberta Canada: Computer Modelling Group Ltd.

28. Gaddipati, M., *Code comparison of methane hydrate reservoir simulators using cmg stars*. 2008: West Virginia University.

29. Wilder, J.W., Moridis, G.J., Wilson, S.J., Kurihara, M., White, M.D., Masuda, Y., Anderson, B.J., Collett, T.S., Hunter, R.B., and Narita, H., *An international effort to*

compare gas hydrate reservoir simulators, in *Proceedings of the 6th International Conference on Gas Hydrates (ICGH 2008)*. 2008: Vancouver, CANADA.

30. Hong, H., Zatsepina, O., and Pooladi-Darvish, M., *Hydrate simulation using cmg stars thermal simulator*. Unpublished, Fekete Associates and University of Calgary.

31. Uddin, M., Coombe, D., Law, D., Gunter, B., , , and *Numerical studies of gas hydrate formation and decomposition in a geological reservoir.* Journal of energy resources technology, 2008. **130**(3): p. 032501.

32. Gaddipati, M., *Reservoirs modeling of gas hydrate deposits in north slope of alaska and gulf of mexico*. 2014, West Virginia University: Ann Arbor. p. 136.

33. Stone, H.L., *Probability model for estimating three-phase relative permeability.* Journal of Petroleum Technology, 1970. **22**(02): p. 214-218.

34. Johnson, A., Patil, S., and Dandekar, A., *Experimental investigation of gas-water relative permeability for gas-hydrate-bearing sediments from the mount elbert gas hydrate stratigraphic test well, alaska north slope.* Marine and Petroleum Geology, 2011. **28**(2): p. 419-426.

35. van Genuchten, M.T., *A closed-form equation for predicting the hydraulic conductivity of unsaturated soils.* Soil science society of America journal, 1980. **44**(5): p. 892-898.

36. Kelkar, M., Perez, G., and Chopra, A., *Applied geostatistics for reservoir characterization*. 2002: Society of Petroleum Engineers.

37. Matheron, G., *Principles of geostatistics.* Economic geology, 1963. **58**(8): p. 1246-1266.

38. Isaaks, E.H. and Srivastava, R.M., *Applied geostatistics*. 1989: Oxford University Press.

39. Pyrcz, M.J. and Deutsch, C.V., *Geostatistical reservoir modeling*. 2014: Oxford university press.

40. Krige, D.G., *A statistical approach to some basic mine valuation problems on the witwatersrand.* J. of the Chem., Metal. and Mining Soc. of South Africa, 1951. **52**(6): p. 119-139.

3. Prudhoe Bay Unit "L-Pad" Reservoir Models

3.1 Introduction

Natural gas hydrate within ANS shallow sand reservoirs was first directly confirmed by data acquired in the Northwest Eileen State-02 well drilled in 1972. Since then, the hydrate deposits in the ANS have been discovered to occur within two large expanses known as the Eileen and Tarn trends. The Eileen trend, shown in Figure 3-1 (a), spans over the eastern part of the Kuparuk River Oilfield, the southern part of the Milne Point and the western part of the Prudhoe Bay oil fields. Estimates indicate that the total gas in place interpreted within shallow sand reservoirs below the production infrastructures within the Eileen Trend may be up to 0.93 trillion cubic meters (33 TCF)[1]. It has been described to compose of six laterally continuous gas hydrate-bearing sand units (as interpreted from the wells penetrating the Eileen accumulation) with thicknesses ranging from 3 to 30 m thick[2]. However, as shown in Figure 3-1 (b), only three hydrate-bearing units (C, D and E) are found in the L-Pad region, with E being in the permafrost region and hence being too cold to be a production target[2].

The PBU L-Pad site has been evaluated to be a favorable site for long-term production testing because of the unique combination of relatively warm reservoirs (approximately 3 ^{0}C warmer than the most promising target in MPU) providing greater sensible heat to maintain gas production rates and the presence of multiple potential production targets (Units C, and D), offering more testing options and flexibility and less operational risks associated with conducting a successful gas hydrate production test[2].

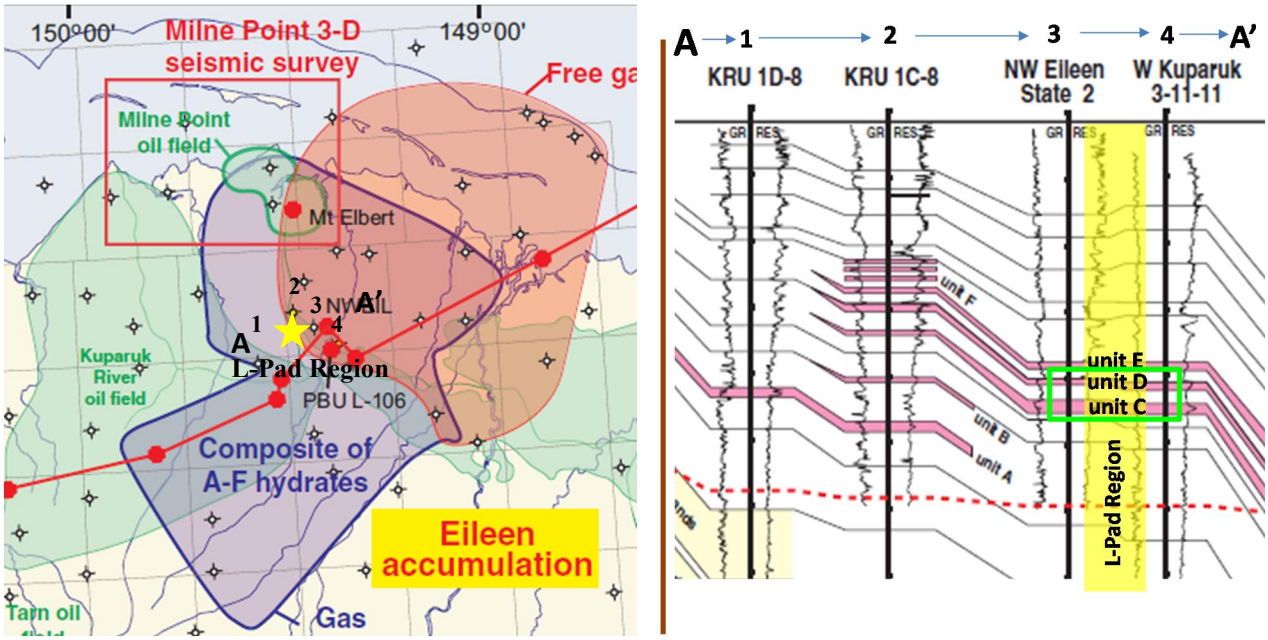

(a) (b)

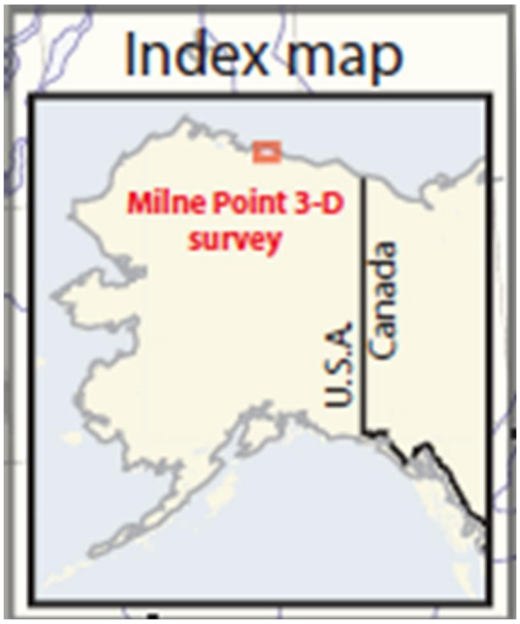

(c)

Figure 3-1: Map of ANS Hydrate Accumulations Showing (a) the Tarn and Eileen Trends (b) cross-section between selected wells (c) index map for (a)[3]

Prior to this study, well log inferred correlations from L-106 and Ignik Sikumi wells have been used to characterize the physical properties controlling the occurrence of gas hydrates within this region. However, in addition to these two control wells, there are other 76 wells with gamma-ray logs that have penetrated the full target intervals (D and C units). The extensive range of well log data provides a sufficient means to describe and assess the reservoir complexity in the development of 3D heterogeneous reservoir model[2].

3.2 Previous Modeling Efforts

Only a few of previous hydrate reservoir models have explicitly incorporated heterogeneity in flow simulation models. Based on a 2D cylindrical geometry and using a vertical heterogeneity in porosity, saturation and intrinsic permeability, Anderson et al.[4, 5] and Myshakin et al.[6] compared production forecasts with those developed based on homogeneity of these properties. In the vertical heterogeneous models, properties were uniform within the lateral extent of a hydrate layer but varied from layer to layer in the vertical direction. These heterogeneous models were significant improvements over their homogeneous counterparts as they predicted higher and accelerated gas production rates. In the study of the production potential of the Eastern Nankai Trough hydrate reservoirs, Kurihara et al.[7, 8] incorporated a higher degree of heterogeneity and included features such as fault and structural dip, and also accounted for change in absolute permeability. It was found that sealing capability of faults and formation dip are the factors significantly affecting short term production. Reagan et al.[9, 10] investigated the impact of heterogeneity (both vertical and lateral) using a 2D reservoir model and concluded that vertical hydrate saturation variability derived from well log data results in enhanced gas production forecasts due to effects of small zones of greater in situ permeability. They also demonstrated that variability in hydrate saturations led to non-uniform

dissociation and the eventual secondary hydrate formation manifesting itself as "evolving solid barrier around a wellbore", "moving solid barrier" or "hydrate lensing" predicted in numerous simulations, the features which can potentially deteriorate production performance[9, 11, 12]. Other models with homogeneous approximations in the descriptions of porosity, saturation distributions and other geophysical properties include those of Gaddipati[13], Gaddipati and Anderson[14], Myshakin et al.[15], Reagan et al.[16] and Kurihara et al.[8].

Heterogeneous 3D reservoir simulations of hydrate systems are very much less common largely due to the complexity of the model domain and sparsity of available field data. However, as the techniques of reservoir characterization of hydrate prospects are being more clearly understood, and more field data from downhole logging operations, core sample analysis, and fluid measurements become available to characterize gas hydrate deposits, more sophisticated reservoir models can be developed.

3.3 Model Objectives

One of the main advantages of three-dimensional reservoir modeling is the more realistic simulation of fluid flow path in the reservoir pore spaces, which might significantly affect the cumulative volumes of gas that may be produced[8]. As a result, a 3D reservoir model should yield a more reliable prediction of sustained gas production.

The goal of the modeling efforts discussed in this chapter is to assess the production potential from 3D reservoir models of the "D" and "C" hydrate-bearing units of the PBU "L-Pad" area of the ANS. The aim is to improve on the existing L-Pad models taking into account the structural and geophysical heterogeneities of the reservoir by maximizing the utilization of the available field data in a comprehensive characterization of the modeled region. Geological

features including faults, dips and hydrate-water contact would also be incorporated in some of the models and the key expected outcomes are:

- a measure of reliability of predictions from a highly data-driven heterogeneous reservoir model
- a deepened understanding of the implications of the differences between predictions of reservoir performance by homogeneous and heterogeneous models
- identification of key reservoir parameters which affect production performance of a hydrate reservoir in a real geological setting
- a description of the true effects of secondary hydrate formation reservoir fluid flow and, ultimately, gas production
- an engineering basis for the design of artificial lift systems for wellbore management and flow assurance during production
- economically viable development options for long-term production

3.4 Reservoir Characterization and Model Development

Simulations were carried out using geostatistical porosity realizations conditioned to log data from 78 wells and incorporating porosity-dependent hydrate saturations and intrinsic permeability. The following is a list of the available field data provided by the USGS:

- Contour map data of depth to top of D and C sand units (Figure 3-2)
- Spatial coordinates (x, y, z) of the intersections of 78 L-pad wells with the top of D and C sand unit i.e. "D and C sand top picks"
- Gamma ray log data from all 78 wells
- Resistivity-derived hydrated saturation log data from two wells - L-106 and Ignik Sikumi (see Figure 3-3 for the cross-section of data from Ignik Sikumi)
- Density logs from two wells (L-106 and L-112)

The maps of Figure 3-2 indicate that there is a general monocline with dip of roughly 5^0 to the east north-east[2]. It also shows a major normal fault (known as the "L-Pad fault") which cuts across the western region of the model area in a roughly north-south orientation in both sand units. The fault has an offset of about 30 m (100 ft) with the most wells penetrating both target sand units on the upthrown side of the fault. This fault has been suggested by Collett et al.[2] to be a lateral seal and therefore, the hydrate formations on both sides of the fault are assumed to be non-connecting. There is a strong indication of hydrate-water contact at ~ 685 m (~ 2248 ft) which may be evidenced in the fact that the bottom of the C sand (pink numbers in Figure 3-2) in L-106 and Ignik Sikumi wells are both at ~ 685 m (~ 2248 ft), and in the well log cross-section for the Ignik Sikumi well shown in Figure 3-3. The water contact also explains why the areal extent of hydrate accumulations (to the east) stops definitively at depths of about 686 m (2250 ft), as shown by the shaded region and the blue line in Figure 3-2 (a).

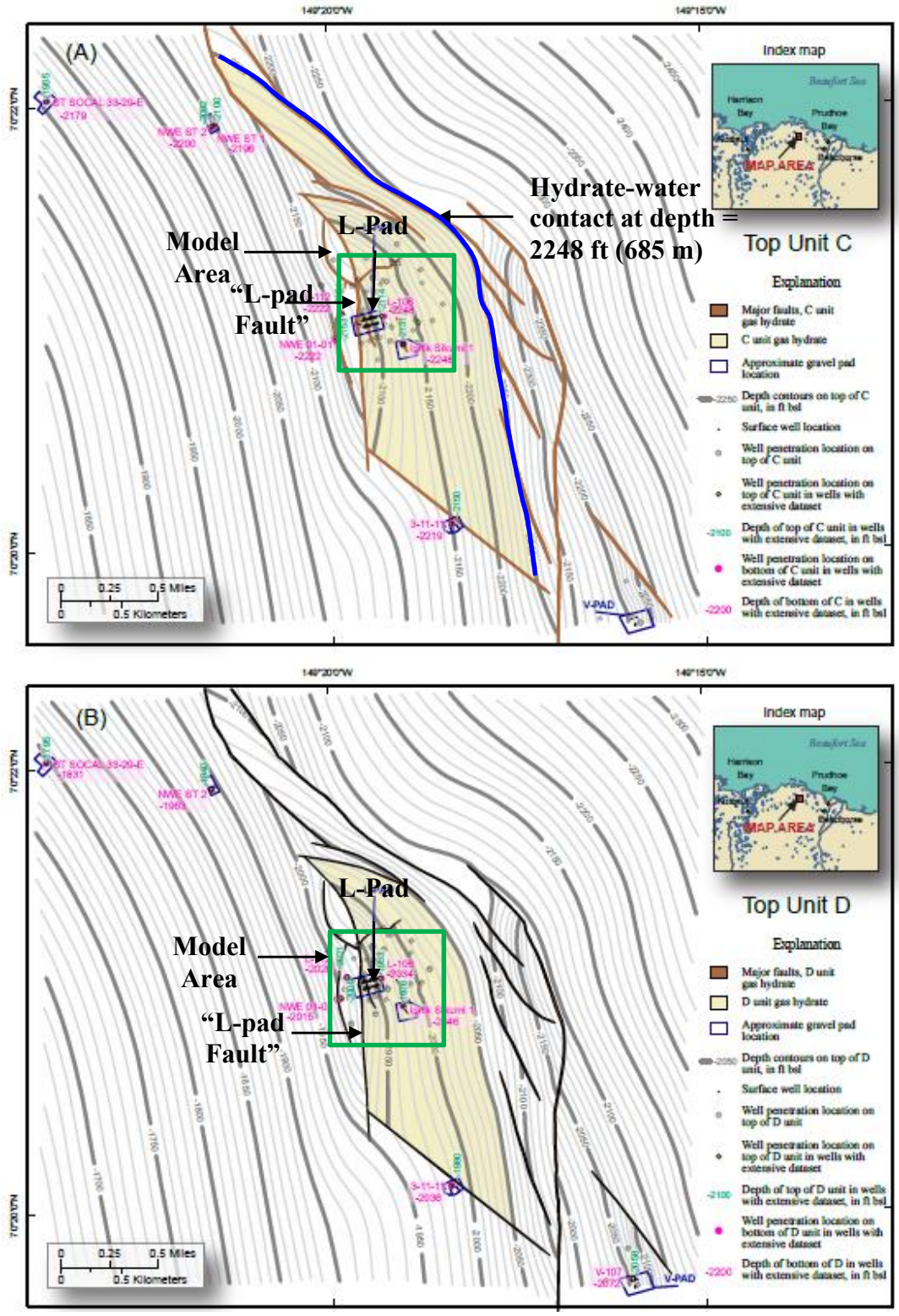

Figure 3-2: Structure contour maps of depth to top of (a) C sand, (b) D sand showing major faults, extent of hydrate occurrence, L-pad location, well intersections points with the sands and model area (1275 m x 1275 m)[17].

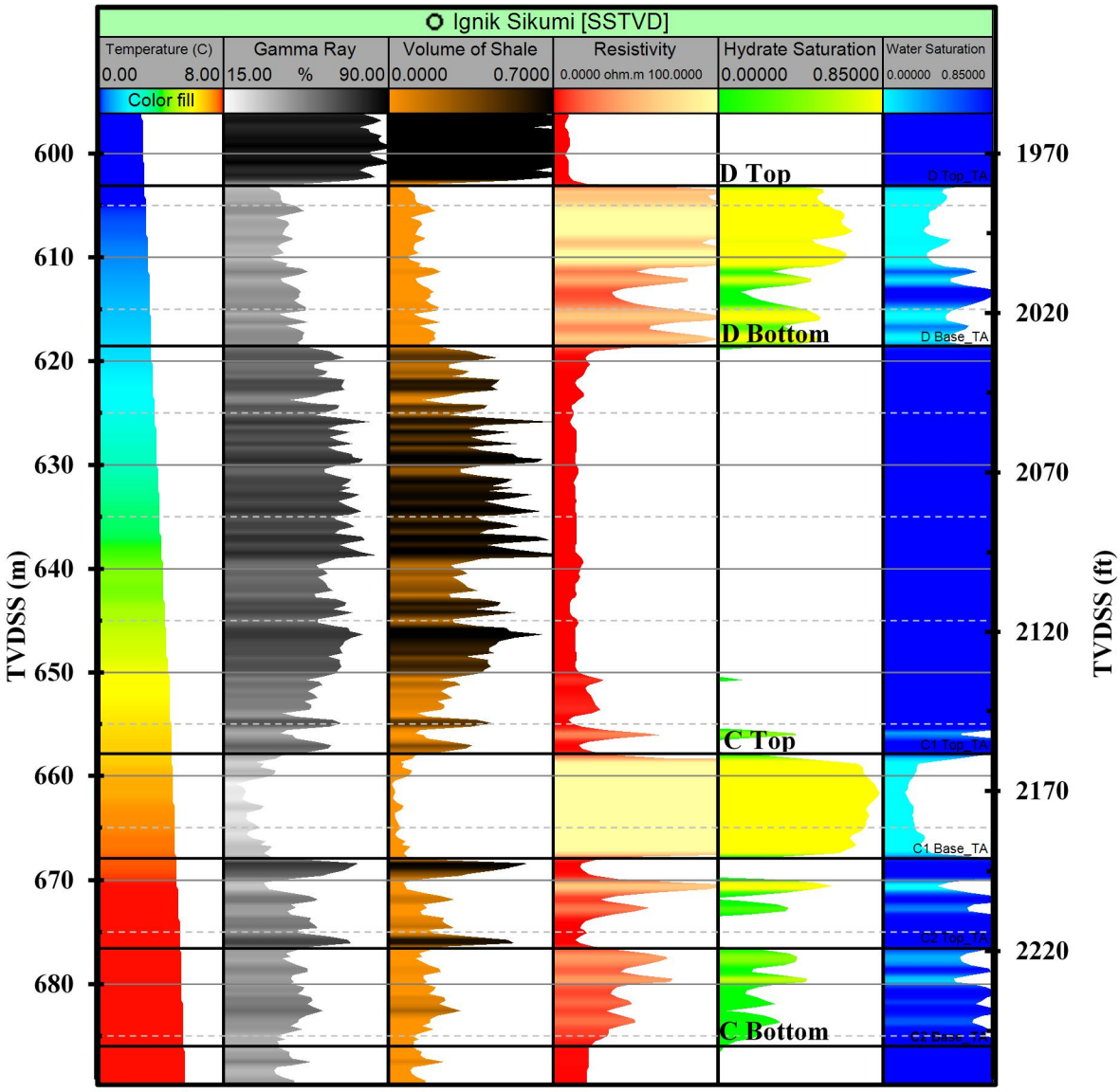

Figure 3-3: Composite LWD log and computed S_h variations with the true vertical depth subsea (TVDSS) within primary sand target intervals at the PBU Ignik Sikumi well. From left to right across the plot: i) equilibrated temperature, ^{0}C ii) gamma ray, gAPI, iii) shale content corrected for non-linear effects, fractional, iv) electrical resistivity, Ωm, v) hydrate saturation, fractional. Hydrate saturations were calculated from resistivity using Archie's Law[18] with the exponent n = 2

There has also been a suggestion of a possibility of hydrate-water contact at the western side of the fault which is also corroborated by the C sand bottom depths being at 677 m (2222 ft) in the wells L-112 and NW Eileen 01-01[3].

Characterization of the reservoir proceeded with calculating volume of shale content (V_{sh}) from gamma-ray logs for all 78 wells using a formula for tertiary sedimentary rocks, with the gamma ray log response in a 100% clean zone (30 API) and a 100% shale zone (120 API)[19]. The density logs available for the L-106 and L-112 wells were used to calculate the shale-corrected porosity (φ_c)[20]:

$$\varphi = \frac{\rho - \rho_m}{\rho_w - \rho_m}, \qquad \varphi_{sh} = \frac{\rho_{sh} - \rho_m}{\rho_w - \rho_m}, \qquad \varphi_c = \varphi - \varphi_{sh} V_{sh} = \varphi - 0.17 * V_{sh} \tag{3-1}$$

where,

ρ = density log value; ρ_m = matrix rock density = 2.65; ρ_w = density of water = 1.00;

ρ_{sh} = shale density ≅ 2.37; φ = porosity without correction;

φ_{sh} = shale porosity correction ~ = 0.17;

φ_c = shale − corrected porosity; V_{sh} = volume of shale from log

Figure 3-4 shows the relationship between the calculated shale volumes, as inferred from the pooled gamma-ray well logs of L-106 and L-112, and their porosity values calculated using Equation (3-1). The field data were fitted by the least-square technique to get the mathematical expression given in Equation (3-2) which was used to estimate porosities for other 76 well logs.

$$\phi = 0.52\, V_{sh}^2 - 0.81\, V_{sh} + 0.48 \tag{3-2}$$

where ϕ = porosity and V_{sh} = gamma ray-inferred volume of shale

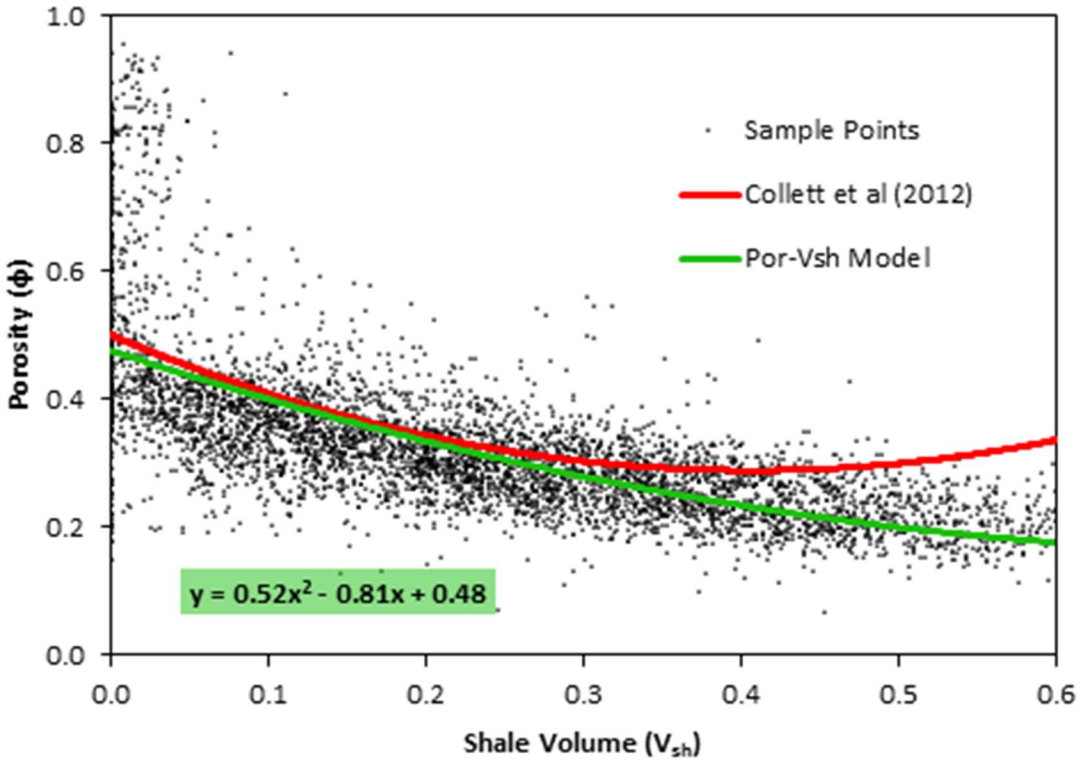

Figure 3-4: Relationship between shale volume and porosity derived from the density and gamma ray logs of PBU L-106 and L-112 wells in the depth interval (33 – 853 m).

The computed "pooled" correlation is compared with a similar equation obtained by Collett et al.[2], using log data from only L-106 (as it was the only available one at the time). There is a close agreement between two equations within the *Vsh* range [0 - 0.4], an interval of which covers more than 80 % of the shale volume data points throughout depths [33 – 853 m]. Validation with the correlation by Collet et al.[2], combined with the indication that the pooled correlation predicts a more realistic deeper reduction in porosity with increase of shale content, justifies the use of the pooled correlation in this study to estimate the porosity values in other 76 wells. The correlations displayed in Figure 3-4 follows a similar trend for the porosity change relative to shale volume derived in other works[21, 22].

A total of 83,450 porosity values were estimated for other 76 wells at intervals of 0.30 m (1 ft) along their trajectories (shown in Figure 3-5) over an approximate area of 1212 m x 1281 m and were the "sampled" input porosity values to be honored in computing geostatistical realizations of porosity distributions over the grid representing the reservoir volume.

Prior to a conducting a geostatistical analysis, it is often a practice to transform original coordinates of the reservoir geometry. This allows for a simpler and more accurate description of spatial relationships among the property values and also ensures that the final model actually reflects geological features such as dips and fault offsets (Pyrcz and Deutsch, 2014). In this work, a simple z-coordinate transformation was done by "flattening" the top of the reservoir with reference to the D sand top picks in each well.

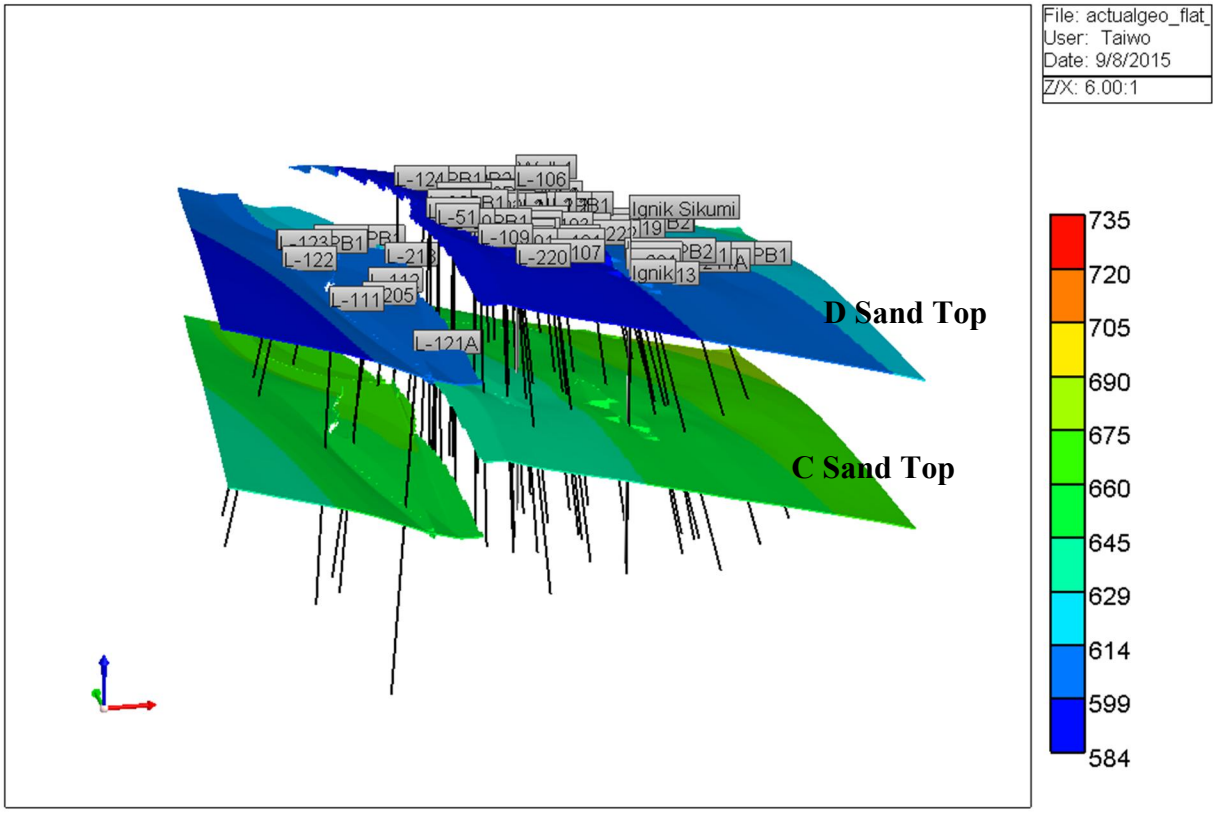

Figure 3-5: Approximate trajectories of 76 L-pad wells penetrating the tops of D and C sands

The transformed z-value (z*) would now represent "thickness" of the sand with respect to top of the D sand, at a given depth (z). For example, the L-106 well intersects the D sand at a depth z_0 = 597 m, therefore a point at z = 620 m in the L-106 well was transformed to z* = z – z_0 = 23 m, where z and z_0 are true vertical depths with reference to sea level (TVDSS). Figure 3-6 shows the pooled variation of estimated porosity values in all 76 wells with transformed depth z* in the interval [0 m– 100 m]. The trend of the porosity distribution is better visualized in the green line, which represents a 400 data point-moving average of the calculated porosity values, and suggests the following general cut-off points for three different sand facies for which three separate geostatistical analyses were conducted.

- [0 m – 20 m] – D Sand
- [20 m – 50 m] – DC Intermediate Shale
- [50 m – 100 m] – C Sand

Many existing well log-based interpretations[2] and reservoir models[5, 13, 23, 24] have described the C sand having a subdivision into an upper (C1) and a lower (C2) by an intermediate shale formation and, although there is only a little supporting evidence of this feature in the depth interval [66 m – 70 m] of Figure 3-6, some of the models developed in this study have included a subdivided C sand for sensitivity and comparison purposes.

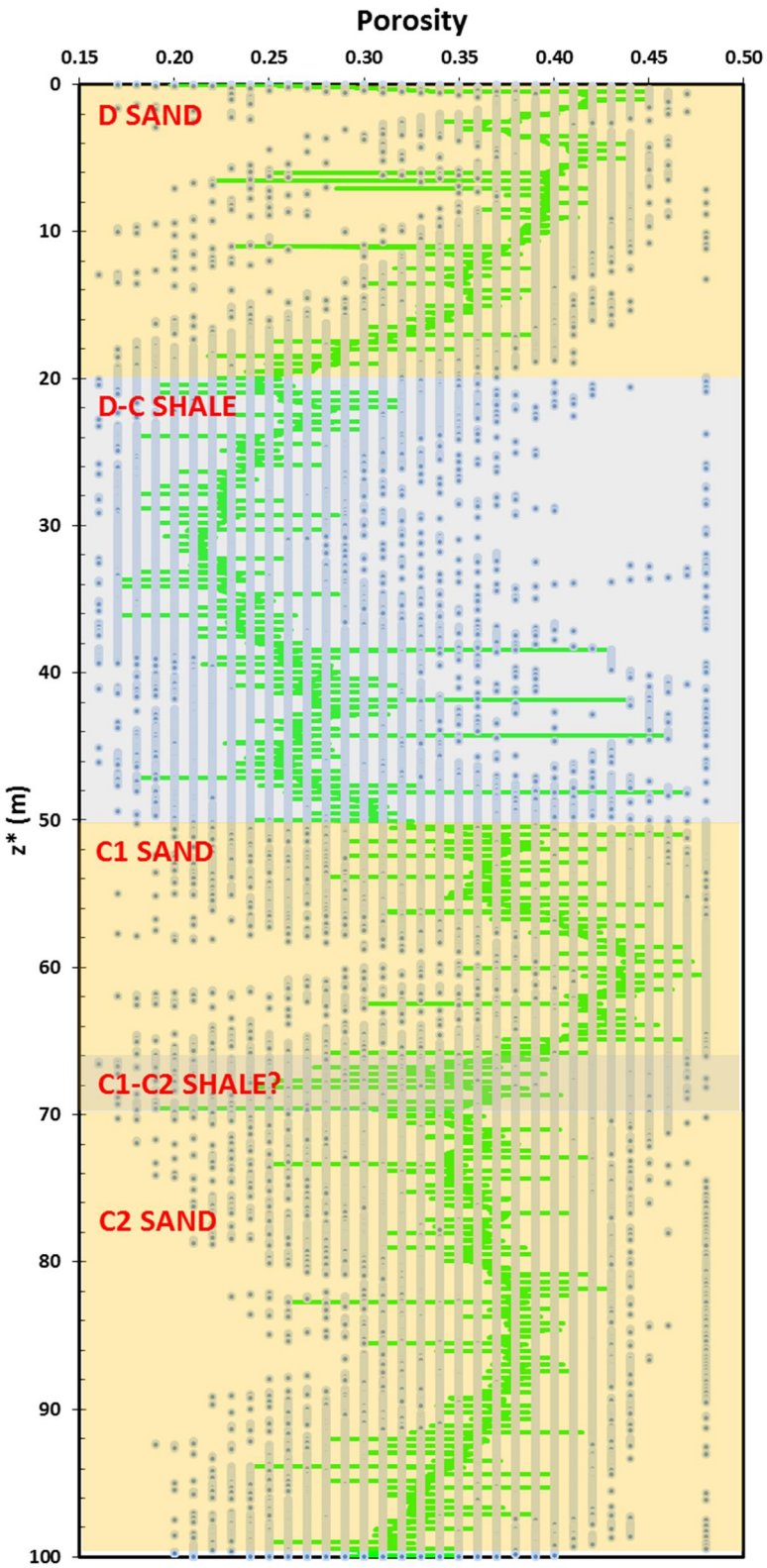

Figure 3-6: Porosity vs transformed depth. The blue dots are the porosity values from Equation (3-2), and the green line represents a 400 data point-moving average of the porosity values

WinGSLIB v.2015, a geostatistical software developed by Clayton and Journel[25] was used for further analysis of the porosity data. To obtain a 3D distribution of the porosity within each of the units, the following steps were taken:

- pre-processed data by trimming, declustering and obtained a normal-score transform of the well log-derived porosity values
- determined and quantified spatial relationships between the porosity values by modeling anisotropic variograms from sample variograms (see Section 2.4.1)
- performed ordinary kriging (OK) with sequential Gaussian simulation (SGS) using the modeled variogram as a weighting function to obtain 10 realizations of normal-score porosity distribution.
- back-transformed the normal-score values into actual porosity values and combined the outputs of three separate sand units for each realization
- converted the transformed coordinates back into original coordinates to obtain the actual reservoir geometry

A more detailed description of the above steps are given in Appendix A. Figure 3-7 shows high low resolution 3D models of a single realization of porosity distribution in the reservoir. The high resolution model (geocellular model) was developed for the purpose of geologic representation while flow simulations were conducted on the low resolution models with near-wellbore grid refinements. High resolution cross-sections across selected wells including L-106 and Ignik-Sikumi are shown in Figure A-11 in the appendix.

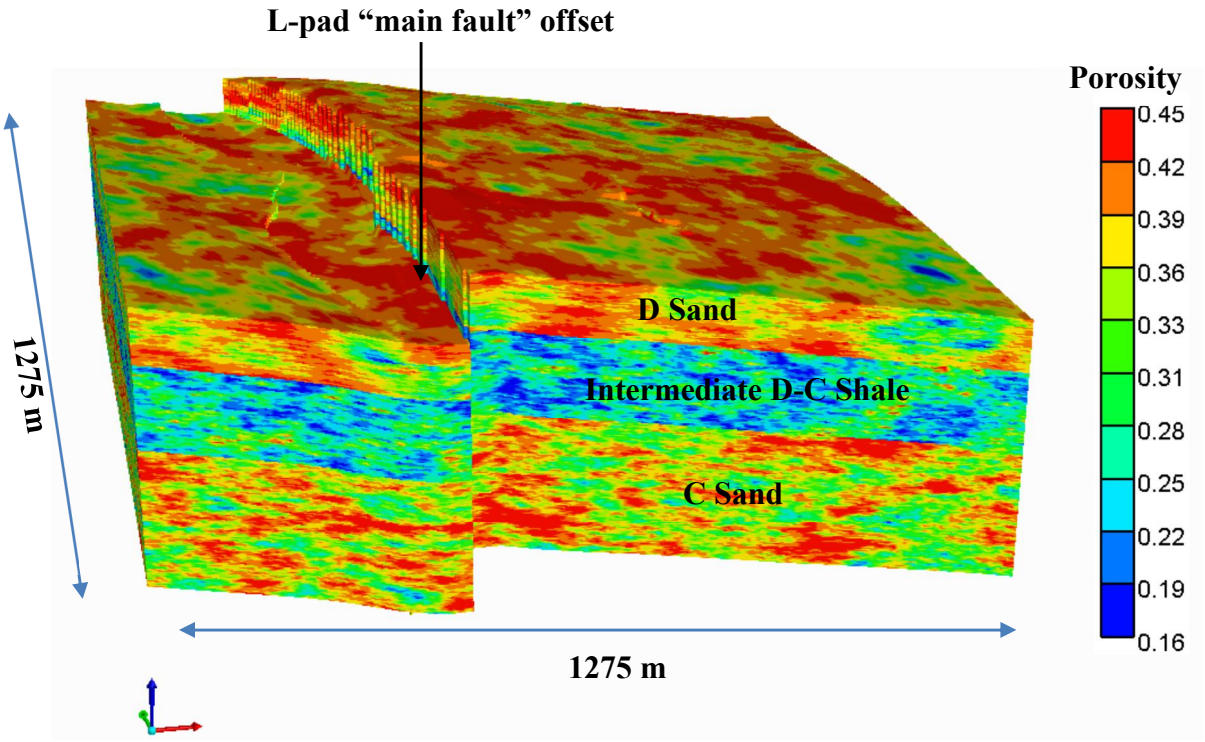

(a)

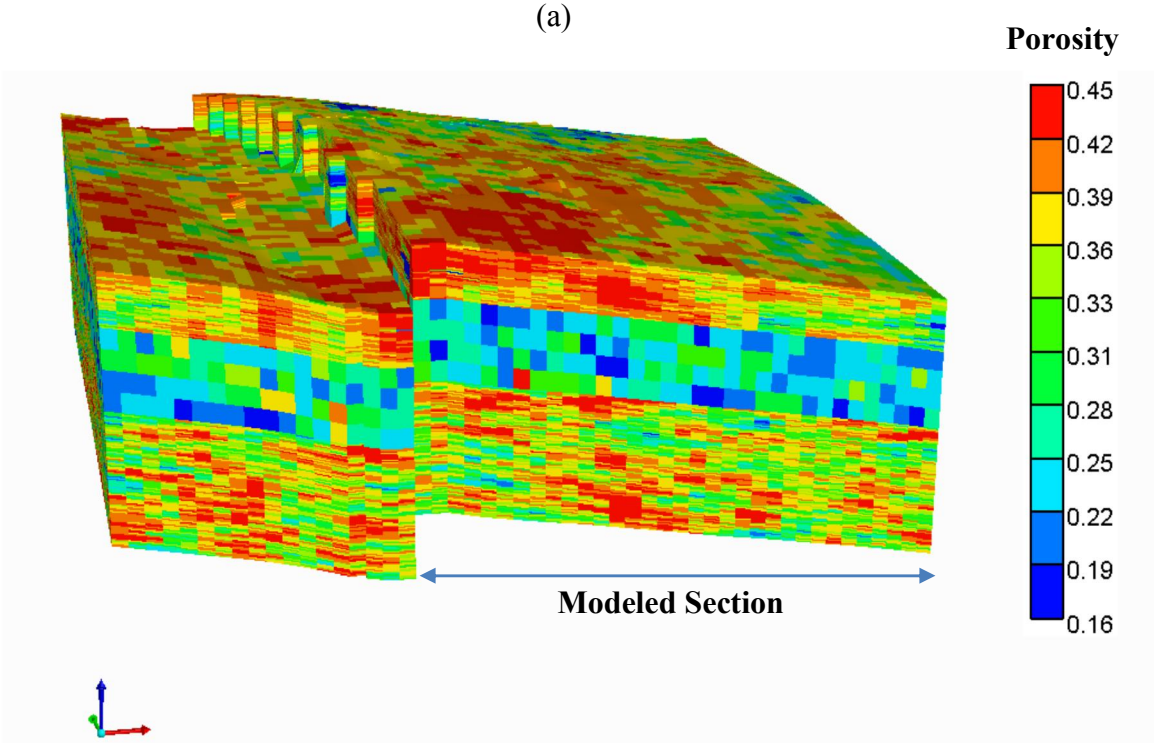

(b)

Figure 3-7: (a) High resolution and (b) Low resolution models of a geostatistical realization of 3D porosity distribution in D and C units of L-pad hydrate-bearing sands

Porosity-dependent hydrate saturation (S_h) distribution was estimated from a linear correlation given by Equation (3-3), which was developed from pooled well log data from the L-106 and Ignik Sikumi wells.

$$S_h = 2.67\,\phi - 0.43 \tag{3-3}$$

The distribution of intrinsic permeability, i.e. permeability of a hydrate-free rock, was estimated by adopting the permeability-porosity correlation given by Equation (3-4)[6],

$$\log k = 0.8052 + 5.2818\,\phi \tag{3-4}$$

The equation above is a result of correlation of porosity and permeability data obtained from measurement experiments on core sections retrieved from the Mt Elbert stratigraphic test well[6]. Given that the petrophysical properties of the D and C sands of the Mt Elbert and L-pad regions have been interpreted as being very similar[2], the use of Equation (3-4) as a proxy is justified.

As indicated on Figure 3-7 (b), in this study, flow simulation models which accounted for all the geological features of the reservoir were conducted using the section of the reservoir model in the eastern upthrown side of the L-pad "main fault" based on a) the fact that most of the wells penetrate the sands in the upthrown side of the fault b) the assumption of a lateral seal provided by the fault, as explained in the previous section.

The following modifications were made to the original low resolution reservoir model derived from geostatistical analysis:

- Large thickness of low permeable overburden and underburden shale layers were added to the top and bottom of the hydrate bearing sands.

- Porosity of intermediate D-C shale was reset to have a uniform value at 0.16, corresponding to the lowest obtained from geostatistical simulation. Shale (horizontal) permeability obtained from Equation (3-4) was also reset to 0.001 mD
- To account for the presence of a hydrate-water contact, hydrate saturation of grid blocks below 685 m were reset from their values obtained from Equation (3-3) to 0.0, and water saturation was set to 1.0.

The addition of the overburden and underburden shale accounts for the heat sink and no mass flow boundaries at the top and bottom of the hydrate bearing sands. The need to adjust shale permeability (k_{xy_shl}) is related to the fact that Equation (3-4) was developed for core-sections retrieved from hydrate-bearing interval, and so the original permeability value (44.7 mD) obtained for shale (with $\phi = 0.16$), may not be accurate. The choice of $k_{xy\_shl} = 0.001$ mD used in all the models in study is somewhat arbitrary, however, the motive for assigning a small non-zero value is to allow hydraulic communication with hydrate-bearing sand units. Shale permeability should be a focus of model refinement in future studies, as it has been shown that predictions can significantly be influenced by shale permeability[13, 15]. Modifications of intermediate shale porosity values were done for simplicity since preliminary sensitivity runs showed no significant difference between a model with the geostatistical values and a model with uniform value at 0.16. Vertical cross-sections of the final model showing porosity, permeability, hydrate and water saturation distributions are shown in Figure 3-8.

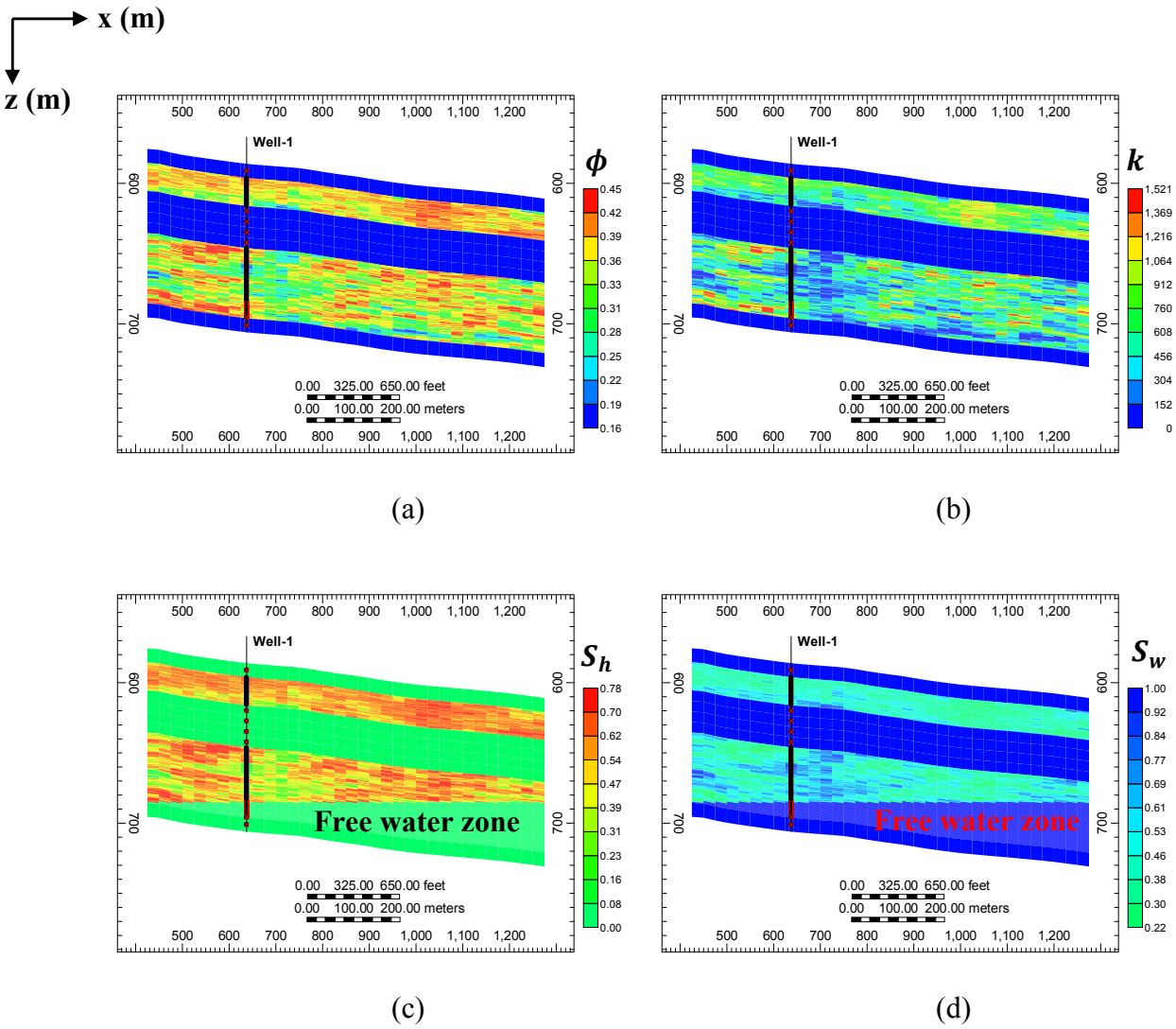

Figure 3-8: Vertical cross-sections of actual reservoir geometry-based models showing distributions of a) porosity (ϕ), b) horizontal permeability (k, mD) c) hydrate saturation (S_h) and d) water saturation (S_w)

The absence of hydrates in the free water region below hydrate-water contact which is well above the inferred approximate base of hydrate stability at 823 m^2 has been attributed to the unavailability of methane gas charge to form hydrates. The water contact at the base of the C unit makes it a Class 2 reservoir (see Section 1.2) and the implications of production from this class of reservoir will be further discussed in this study.

3.5 Reservoir Model Parameters and Initial Conditions

A summary of the model geometry and discretization based on the sand cut-off intervals suggested by Figure 3-6 are presented in Table 3-1.

Table 3-1: Model geometry details

Formation	Top (m)	Thickness (m)	Layer Range (Number of Layers)	Simulation Layer Thickness (m)
Shale	575 – 626	10 (x 10)*	1 (1)	100*
D Sand	585 – 636	20	2 – 41 (40)	0.5
Shale	605 – 656	30	42 – 45 (4)	7.5
C Sand	635 – 686	50	46 – 145 (100)	0.5
Shale	685 – 736	10 (x 10)*	146 (1)	100*

*Grid thickness was multiplied by a volume modifying factor of 10, so that effective simulation layer thickness = 100 m

A summary of the other reservoir properties and initial conditions are given in Table 3-2. The parameters for relative permeability model (see Section 2.3.2) used in this study were such that the average effective (horizontal) permeability of the hydrate-bearing sections of the reservoir is ~ 0.2 mD. This value compares very closely to the result from the analysis and history matching of data obtained from the pressure buildup and drawdown tests from the Mount Elbert stratigraphic test well using Schlumberger's Modular Dynamics Formation Tester (MDT) wire line tool[26].

Table 3-2: Reservoir properties, initial conditions, and pertinent model parameters.

Parameter	Value
Porosity of sand units, ϕ	0.16 – 0.45 Geostatistical realizations based on 78 well logs
Initial hydrate saturation	0.00 – 0.78
Intrinsic permeability of sand units, k_{sand}, *mD*	47 – 1521 horizontal and 24 – 761 vertical permeability (0.5 anistropic factor)
Intrinsic permeability of the shale layers, k_{shl}, *mD*	0.001 horizontal and 0.0005 vertical
Porosity of shale layers, ϕ	0.16
Pore compressibility, α_p, Pa^{-1}	$5 \cdot 10^{-10}$
Thermal conductivity of hydrate-bearing sand, k_{sand}, *W/m K*	2
Thermal conductivity of shale, k_{sand}, *W/m K*	2
Capillary pressure model[27]	$P_{cap} = -P\left[(S^*)^{-1/\lambda} - 1\right]^{1-\lambda}$ $S^* = \frac{(S_A - S_{irA})}{(S_{\max A} - S_{irA})}$
S_{irrA}[24]	0.10
λ[5, 23]	0.77437
S_{maxA}	1
P_{max}, *Pa*	10^4
Pore water salinity, *ppt*	5
Relative permeability Modified Stone 3-phase model[28]	$k_{rA} = (S_A^*)^{nA}; \;\; k_{rG} = (S_G^*)^{nG}$ $S_A^* = \frac{(S_A - S_{irA})}{(1 - S_{irA})}; \; S_G^* = \frac{(S_G - S_{irG})}{(1 - S_{irG})}$
n[4, 5]	n_A = 5. 04; n_G=3.16
S_{irrG}	0
S_{irrA}	0.1
Rock density, kg/m^3	2650

The pressure in the sediment subsurface was assumed to follow a hydrostatic pore pressure distribution. This assumption is supported by measurements taken in natural hydrate deposits[29]. For thermal distribution throughout the reservoir model the local geothermal gradient, 0.038 °C/m, derived from the Iġnik Sikumi DTS temperature log was used[30]. This resulted in average pressure and temperature of 7.4 MPa and 5.05 °C for unit D, and 8.0 MPa and 7.15 °C for unit C, respectively. For the layers of the reservoir model, the initialization of P/T conditions (pressure and temperature gradients throughout the vertical dimension of the domain) were carried out to achieve hydraulic, thermal, thermodynamic, and chemical equilibrium and ensure correct pressure and temperature conditions of the layers relative to the base of gas hydrate stability. A no-mass/heat flow boundary is imposed at the western boundary due to the presence of the assumed "sealing" L-pad fault[2]. Owing to lack of additional information, the model assumes no mass or heat flow at the north, south and east boundaries and the possible implications of this assumption is outside of the scope of the work and should be a focus of model refinement in subsequent studies. The top of the overburden and the bottom of the underburden are kept at a fixed temperature condition to provide heat flux from the surrounding strata into the reservoir.

The original size (25 m x 25 m) of the grid blocks in the horizontal plane was refined to the smaller grid blocks (0.6 m x 0.6 m) around the wellbore to improve accuracy of numerical computation. The size of the refined grid blocks is such that their effective radii is at least 10 % larger than the wellbore radius of 0.11 m to ensure numerical convergence[31]. Depressurization is initiated by setting a fixed minimum well flowing bottom-hole pressure (BHP) at 2.8 MPa, which is just above the quadruple point of pure methane hydrate i.e. a thermodynamic equilibrium state where water, gas, ice and hydrate phases coexist. In the

absence of significant additional heat-losses due to Joule-Thomson effect, the well BHP constraint would prevent ice formation. The numerical studies were performed using CMG STARS, a commercial simulator for non-isothermal reservoir processes[31] (see Section 2.3).

3.6 Flow Simulation Results and Discussions

This section describes the design and discusses the results of all simulation cases in this part of the study. In the first set of flow simulations, production forecasts done based on 10 different geostatistical realizations with each utilizing vertical and inclined well designs, respectively. The purpose was to quantify uncertainty assessments in the estimation of property distributions in the reservoir and also to observe the response of reservoir performance to different well designs.

In the vertical well design (Well-1 in Figure 3-8), a well was completed in the vicinity of the actual location of the L-106 well, which is an optimal location with respect to formation temperature and well-hydrate contact i.e. in the deepest (warmest) possible region in which the wellbore-hydrate contact area is maximized. The inclined well design (Well-2a in Figure 3-9 (b)) penetrates the top of the D sand in the eastern part of the reservoir and drilled westward through the sands with an inclination of $\sim 8^{0}$ to the horizontal. Sensitivities were conducted using other five inclined well configurations based on a selected geostatistical realization. Well-2b, shown in Figure 3-9 (c), was such that the direction of completion of the well section in the D and C units is exactly opposite that of Well-2a, to model a *fish-hook* style of completion. Well-3a is different from Well-2a in the sense that it is drilled from west to east (Figure 3-9 (d)) and Well-3b is the *fish-hook* counterpart of Well-3a. Well-L2a and Well-L2b (Figure 3-9 (e) and (f)), represent well designs with two lateral legs penetrating each of the sands. A summary of the well trajectories is presented in Table 3-3.

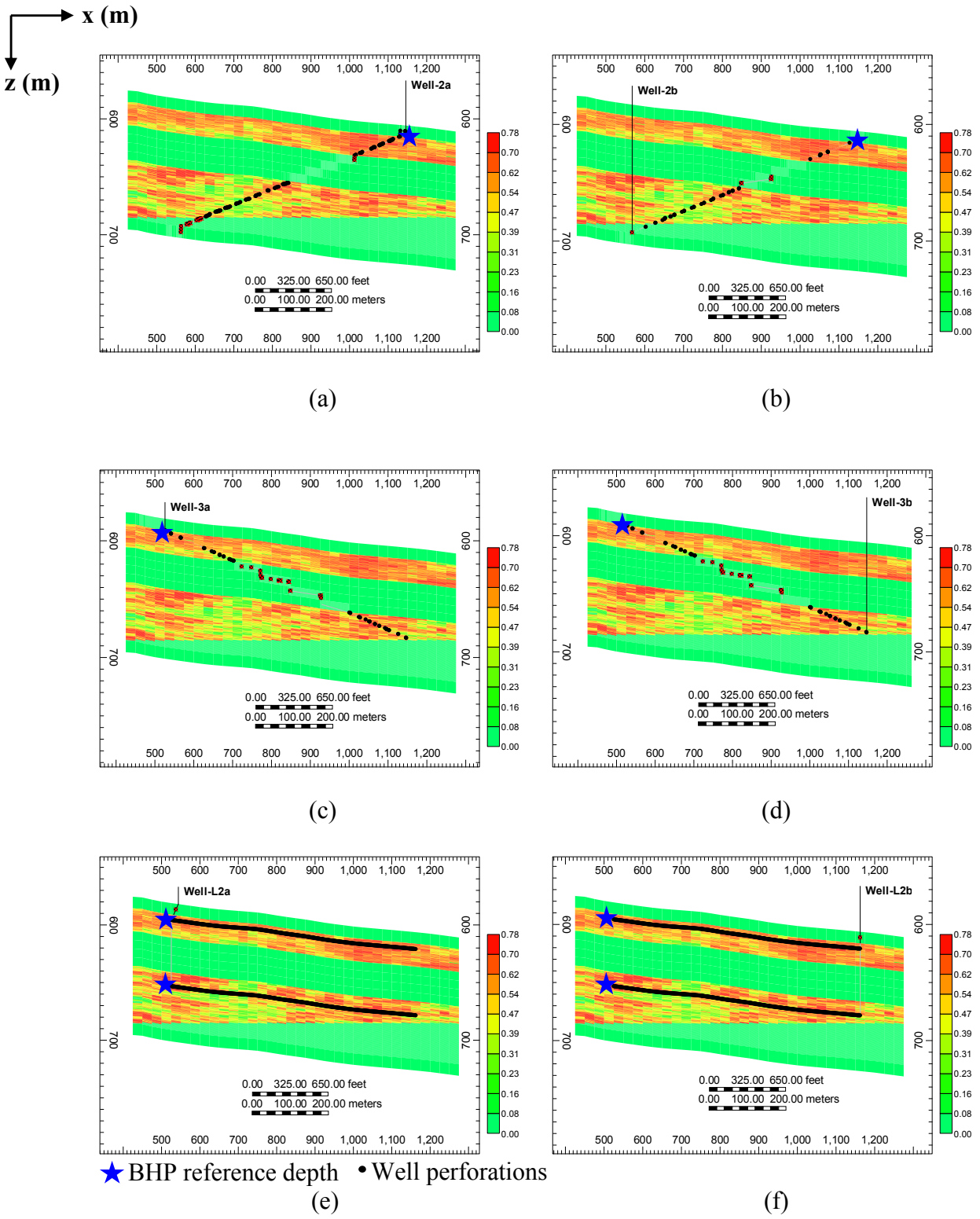

Figure 3-9: Well designs for a) Well-2a, b) Well-2b, c) Well-3a, d) Well-3b, e) Well-L2a, and f) Well-L2b

Table 3-3: Well trajectory and completions summary

Well Configuration	Angle to Horizontal Plane (^{0})*	Perforated Length (m)		Overall Length (m)
		D Sand	C Sand	
Well-1	90	20	30	700
Well-2a/Well-2b	8	134	217	1275
Well-3a/Well-3b	8.5	183	150	1270
Well-L2a/Well-L2b	2.3	650	650	1980

*within the target sands

A guide to drilling these wells is given in Table B-1 of Appendix B. In all configurations, wells were perforated only in the hydrate bearing sand intervals and well sections below the hydrate water (free water zone) were not perforated. However, a sensitivity study based on well perforation in the free water-zone was performed and is discussed in Section 3.6.2. Well BHP reference depth was set to be at the highest point in the well trajectory within the sand for all well designs, as indicated on the cross-sections shown in Figure 3-9. A production time of 30 years was simulated.

3.6.1 Uncertainty Assessment

The gas rates and cumulative volumes of gas produced using 10 realizations are given in Figure 3-10 (a) and (b) as a time-dependent series for the vertical (Well-1) and inclined (Well-2a) well configurations, respectively. In Well-1, the peak gas rates are within the range $7.00 \times 10^4 - 8.82 \times 10^4$ ST m^3 (2.5– 3.1 MMSCF/day), and are reached within 14 – 23 years of production. The highest rates in Well-2a are in the interval $1.05 \times 10^5 - 1.20 \times 10^5$ ST m^3/day (3.71 – 4.24 MMSCF/day), are quickly reached within 3 – 5 years of production.

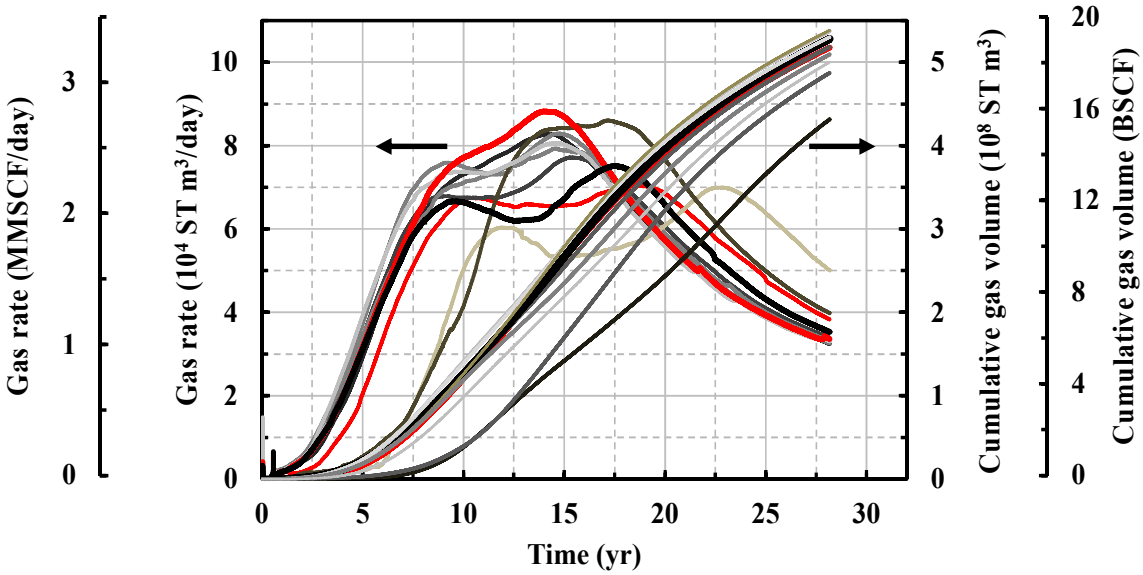

(a)

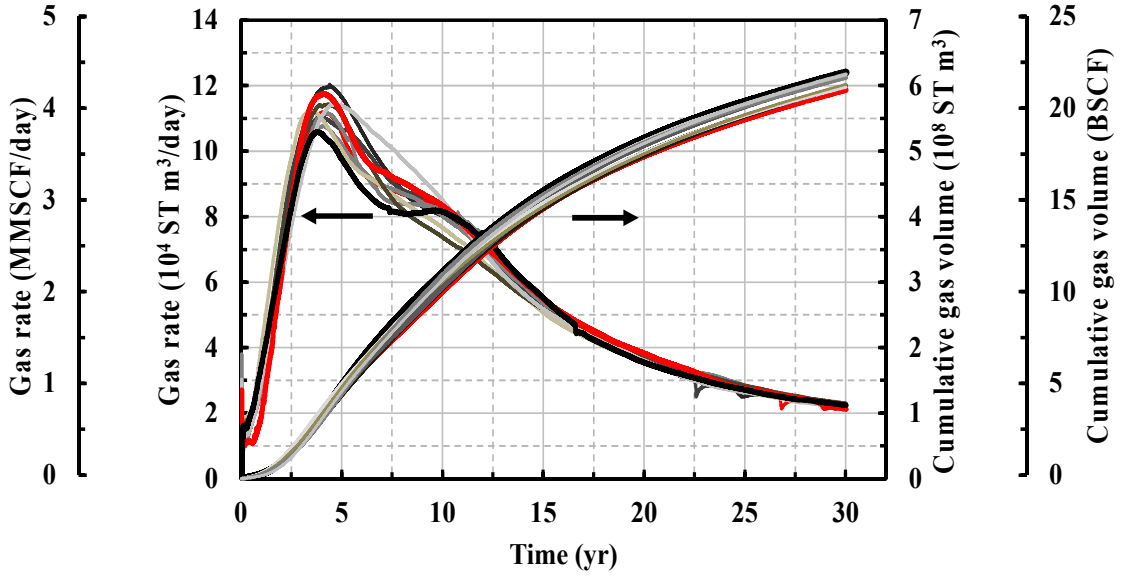

(b)

Figure 3-10: Gas rate and cumulative volumes using 10 realizations of porosity distributions with coupled hydrate saturation and intrinsic permeability with a) Well-1 (vertical), and b) Well-2a (inclined)

At the end of the production period, cumulative gas volumes are within 4.63 x 10^8 – 5.59 x 10^8 ST m^3 (16.35 – 19.74 BSCF) and 5.93 x 10^8 – 6.20 x 10^8 ST m^3 (20.94 – 21.90 BSCF) for Well-1 and Well-2a models, accordingly. The calculated means and standard deviations of cumulative gas volumes at the end of the 30 year-production period indicate that uncertainties (in form of standard error of the means) are only about 1.7 % and 0.5 % of the mean values 5.33±0.09 x 10^8 ST m^3 (18.82±0.32 BSCF) and 6.07±0.03 x 10^8 ST m^3 (21.44±0.11 BSCF) for the vertical and inclined wells, correspondingly. These numbers show that deviations in assessment of gas production potential based on 10 geostatistical realizations are within narrow ranges and are an indication of consistency in model predictions. This also provides the evidence that the amount of well log data available for this study is sufficient to adequately characterize the reservoir, as earlier inferred by Collett et al.[2] from which reliable estimates of production potential can be obtained.

Table 3-4 provides a summary of the probability associated with the predictions, which is inferred from the plots of cumulative probability of the total gas volume produced at the end of 30 yr shown in Figure 3-11.

Table 3-4: Probabilities of cumulative gas volume predictions at 30 yr

P-Level, %	**Cumulative gas volume @ 30 yr, 10^8 ST m^3 (BSCF)**	
	Well-1	Well-2a
10	≤ 4.70 (16.60)	≤ 5.98 (21.12)
50	≤ 5.33 (18.82)	≤ 6.07 (21.44)
90	≤ 5.70 (20.13)	≤ 6.23 (22.00)

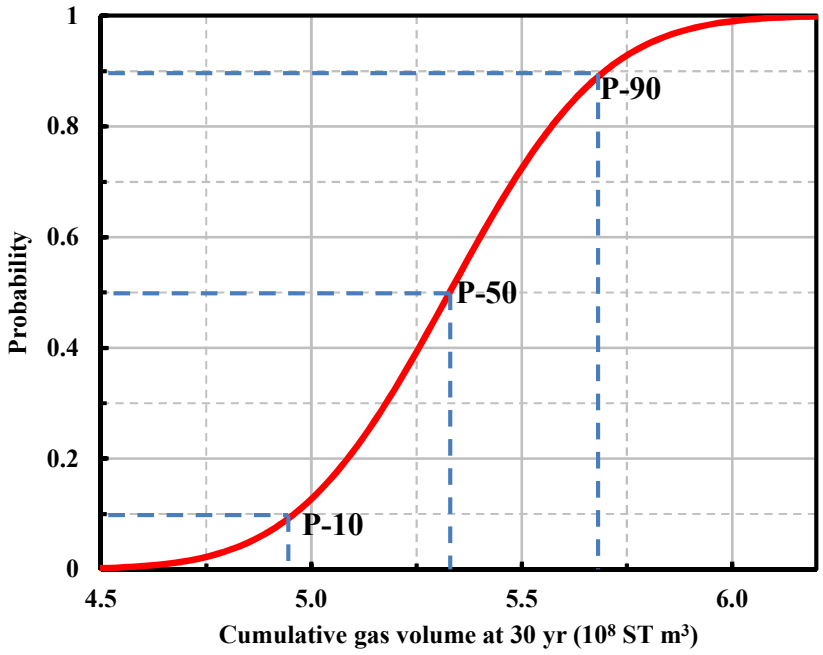

(a)

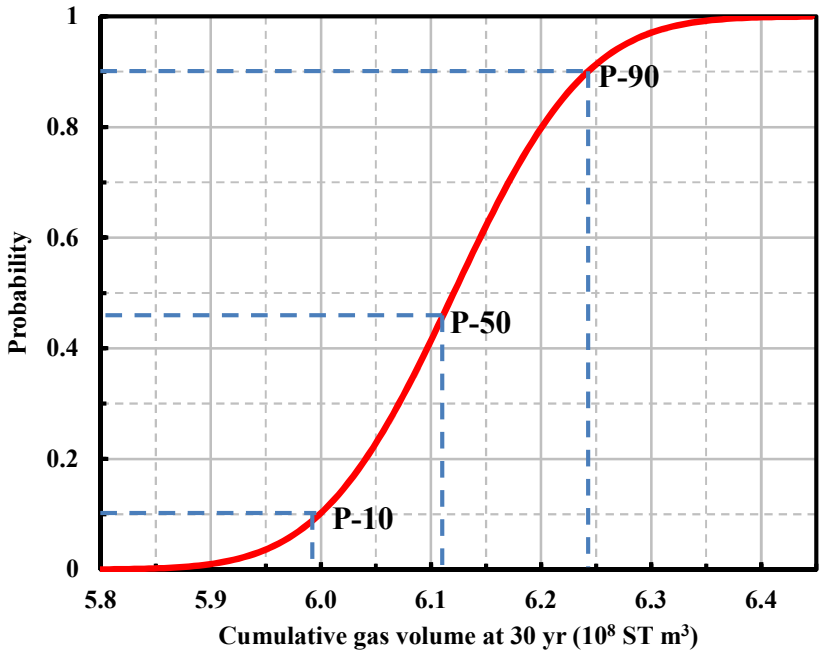

(b)

Figure 3-11: Probability distribution of cumulative gas volume produced at 30 yr in a) vertical well (Well-1), and b) inclined well (Well-2a)

3.6.2 Sensitivity to Well Design

The results reported in this section provides an opportunity to study the effect of well design on reservoir performance in order to provide a basis for recommending an optimum well configuration.

Gas rates and cumulative volumes

Figure 3-12 shows gas production rates and cumulative volumes for selected well designs (of Figure 3-9). Results for Well-2b and Well-3b show no significant disparity from Well-2a and Well-3a, respectively, and hence are not plotted in Figure 3-12. The gas rate profiles show that production from the 2-leg lateral well (Well-2a) is highest during the first 10 years of production. However, rates from Well-2a continue to fall below those from other well configurations in the period between 10 – 17 yr. In the last 10 years of production, rates from all deviated wells (Well-2a, Well-3a and Well-L2a) converge, with the vertical well producing at significantly higher rates for most of the period. The maximum gas rate, peak time and cumulative gas volume achieved at 30 yr are given for each well configuration in Table 3-5.

A common feature in the observed gas rate profiles is the rise to two distinct peaks at different times, and the interval between these peak times seems to be consistent (7 – 8 yr) in all four well configurations. The "lag" time between these two peaks may be directly related to the difference in stability between the D and C hydrates i.e. the difference in time required for the reservoir conditions of the D and C units to be shifted outside the zone of hydrate stability under the effect of depressurization.

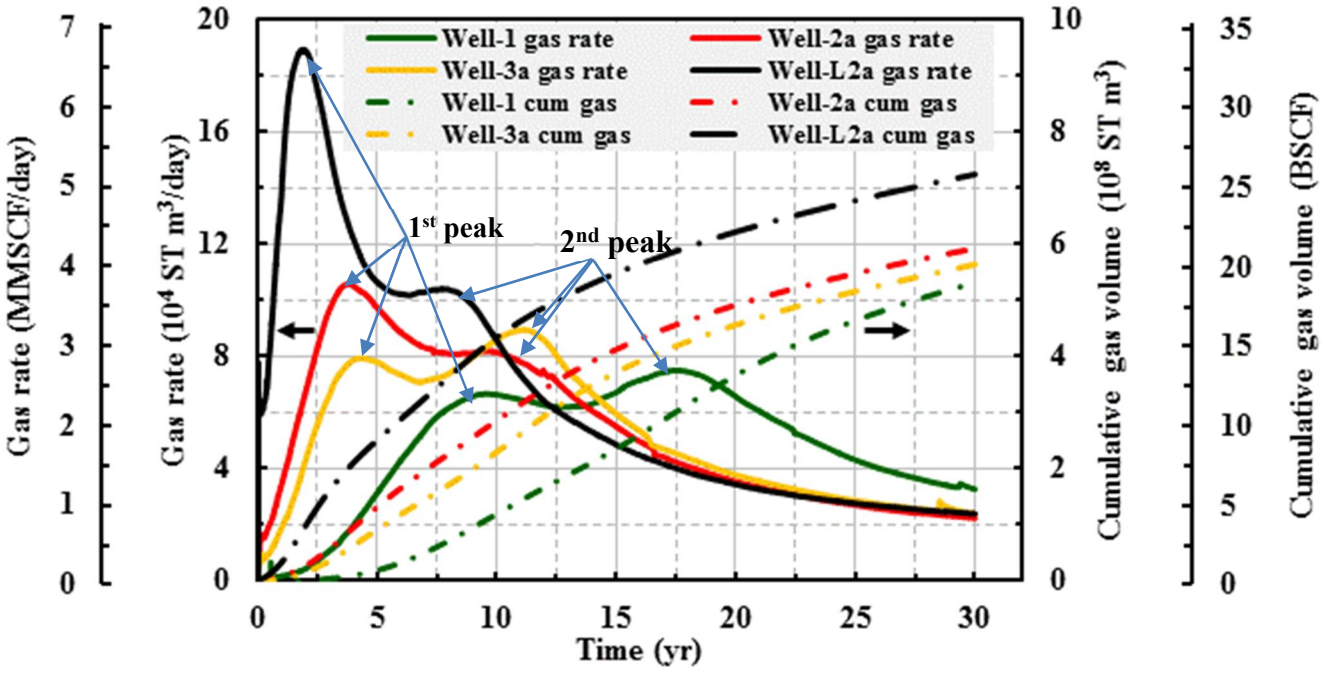

Figure 3-12: Gas rates and cumulative gas volumes from selected well configurations shown in Figure 3-9

Table 3-5: Maximum gas rates, peak times and cumulative gas volumes

Well configuration	Maximum gas rate, 10^4 ST m^3/day (MMSCF/day)	Time to 1st peak, yr	Time to 2nd peak, yr	Cumulative gas volume at 30 yr, 10^8 ST m^3 (BSCF)
Well-1 (vertical)	7.51 (2.65)	10	18*	5.32 (18.79)
Well-3a (inclined, W-E)	8.95 (3.16)	4	12*	5.65 (19.95)
Well-2a (inclined, E-W)	10.58 (3.74)	4*	11	5.93 (20.94)
Well-L2a (2-leg lateral)	18.95 (6.69)	2*	9	7.27 (25.67)

*time at maximum gas rate

Due to warmer temperatures and, hence, proximity to equilibrium, hydrates in the C sand would dissociate first, and therefore is the source of the bulk part of the total gas produced in earlier times, as indicated by the rise to the 1st peak. As reservoir pressures are further lowered, hydrates in the D sand begin to dissociate (rise to 2nd peak) and contribution to gas production from the D sand increases during later periods.

Additional sensitivity simulations with reference to Well-L2a as a base case (Figure C-1, Appendix C) showed that higher initial gas rates were achieved in a well completion with tightly perforated intervals (as in the base case), than completions with wider perforated intervals. Essentially the same cumulative gas volume was produced at the end of 30 yr, however, well perforations of the base case may provide the highest economic returns owing to its initial high production volumes. Moreover, if there are appreciable costs associated with more number of perforations, well with an intermediate perforation interval (*ref. x3* in Figure C-1) could be the economically optimal choice.

Evolution of reservoir properties

A study of the evolution of reservoir properties with time provides more insight on the observed characteristics of the gas rate profiles of Figure 3-12. Vertical cross-sections with distributions of hydrate saturation, gas saturation, pressure and temperature in the reservoir for the vertical well (Well-1) and double-lateral well (Well-L2a) are shown in Figure 3-13 and Figure 3-14, respectively.

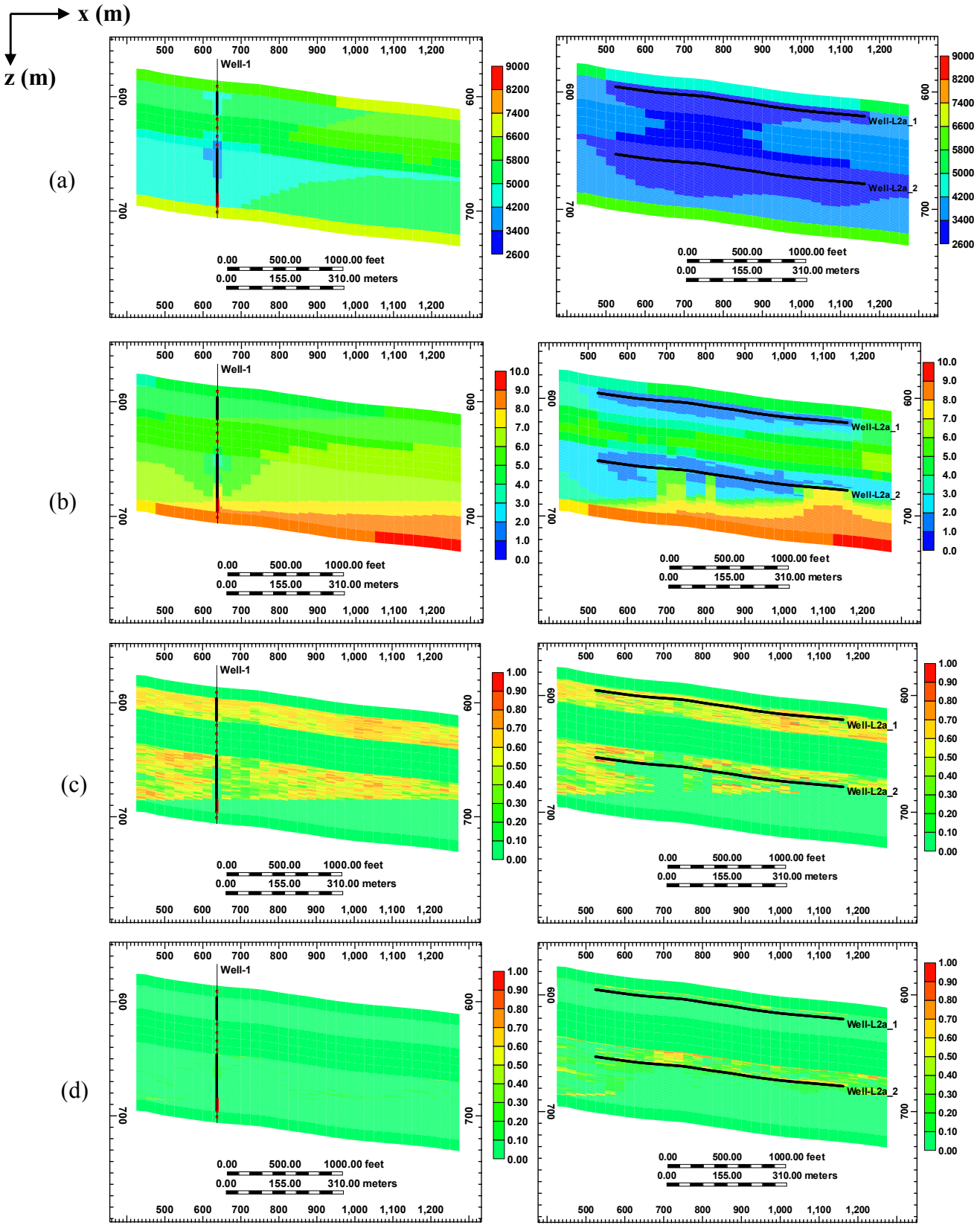

Figure 3-13: (a) Pressure distribution (kPa), (b) temperature distribution (°C), (c) hydrate saturation, and (d) gas saturation in the reservoir with Well-1 (left column) and Well-L2a (right column) well configurations after 2 years of production.

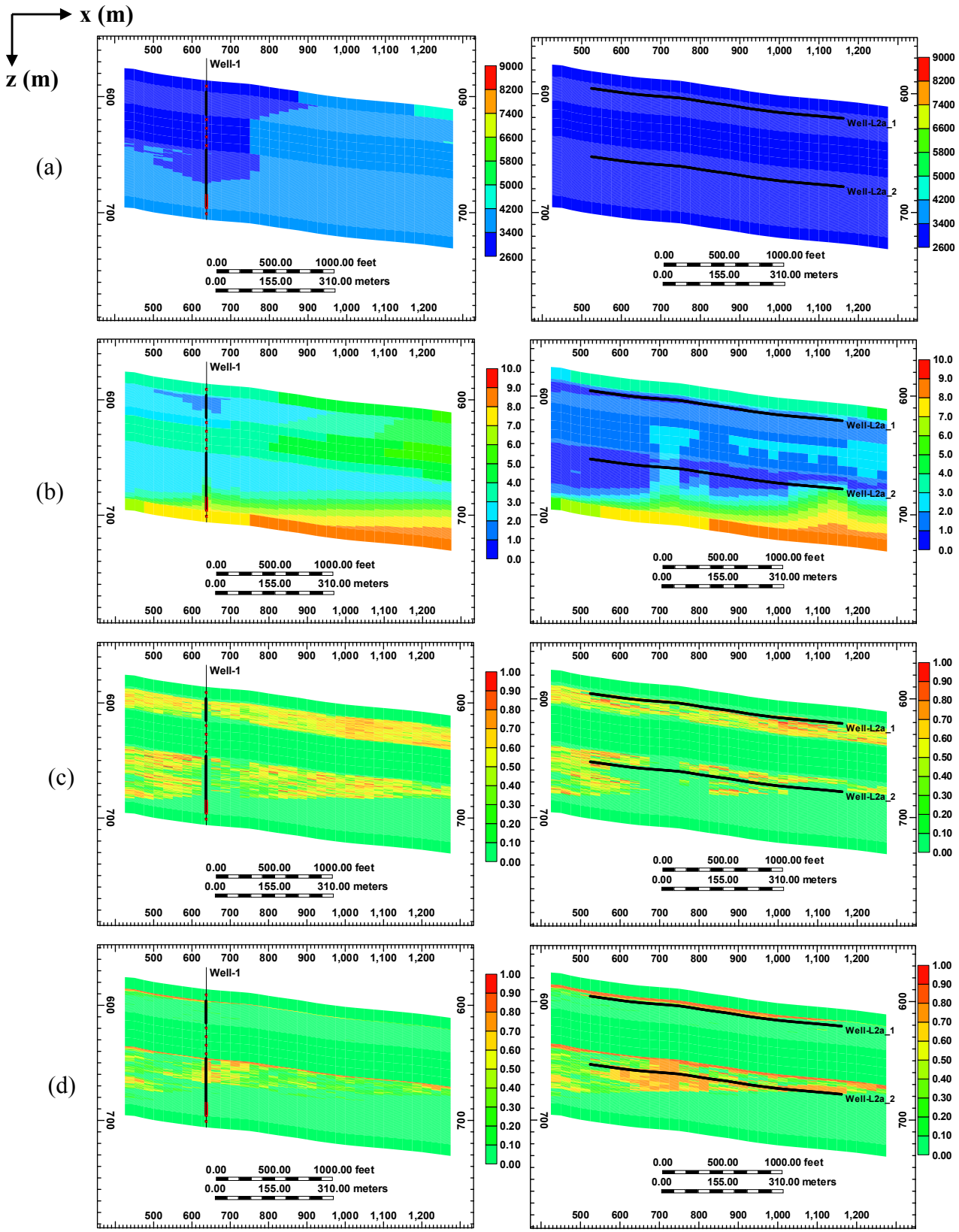

Figure 3-14: (a) Pressure distribution (kPa), (b) temperature distribution (^{o}C), (c) hydrate saturation, and (d) gas saturation in the reservoir with Well-1 (left column) and Well-L2a (right column) well configurations after 15 years of production.

In Figure 3-13, pressure distribution indicates that pressure drop in each of the hydrate units around the lateral sections of Well-L2a is greater than that near the vertical one, which is as a result of a larger contact area of the lateral well with the hydrate, leading to a more effective depressurization. At the onset of production, the mobile phase flow out of the lateral wells creates a pressure front propagation throughout the surrounding formation, which induces hydrate decomposition. Due to the endothermic nature of the hydrate decomposition, the temperature is reduced in the areas with dissociating hydrate. Deeper temperature reduction by the laterals compared to the vertical well confirms more intense hydrate dissociation, as can be inferred from the contrast in distributions of residual hydrate and gas saturation in both well designs at 2 yr. These saturations are a direct evidence of the higher gas rates achieved in the lateral well design at the early stages.

After 15 years of production, Figure 3-14 shows that reservoir pressure declines below 3400 kPa only in a limited area around the vertical well, while it drops below that value in the entire reservoir for the double-leg lateral well. More pronounced reduction of average reservoir pressure in the lateral well design means that the drawdown i.e. the difference between the average reservoir and flowing bottom-hole pressure, which is the driving force for the mobile phase flow to the well has declined. For the vertical well the pressure drop changes more slowly as it is evident comparing the pressure distributions of Figure 3-13 (a) and Figure 3-14 (a). The result of this is the observed lower gas rates from the bi-lateral wells and slower decline of the gas rate from the vertical well, with the gas rate from the vertical well becoming higher well after 13 years of production (Figure 3-10). The corresponding temperature distributions of Figure 3-13 (b) and Figure 3-14 (b) show that temperatures in the hydrate bearing sands are reduced to about 3 – 6 ^{0}C and 1 – 3 ^{0}C for the vertical and bi-lateral well configurations,

respectively. This indicates the availability of more sensible heat available in the reservoir to drive the dissociation process which further corroborates reason for the higher gas rates observed in the vertical well during later part of the production period.

An interesting characteristic of the hydrate distribution shown in Figure 3-13 and Figure 3-14 is the absence of "a dissociating interface" between hydrate-bearing sediment and constantly evolving mobile phase zone that is an inherited feature of all simulations involving homogeneous representations of porosity and hydrate saturation. Also, there is no "protruded areas of fast hydrate decomposition" developing in the lateral direction in the hydrate reservoirs with vertical heterogeneity[5, 6, 10, 23]. The 3D heterogeneous hydrate distribution implemented in these models has led to a highly non-uniform dissociation of hydrates as compared with models based on homogeneous and 2D heterogeneous distributions. Figure 3-13 (c) and Figure 3-14 (c) show the hydrate saturation evolving as "patches" of different saturation values. Therefore, in reality, the true nature of a hydrate dissociating front is determined by a complex interplay of initial and local geophysical properties including porosity and saturations, pore pressure and relative permeability[32].

Gas saturation distribution (Figure 3-13 (d) and Figure 3-14 (d)) show that unproduced dissociated gas, is distributed widely in heterogeneous porous network, which is again unlike the typical observations of a distinct layer of free gas at the boundaries between hydrate-bearing layers and shale, as predicted in homogeneous and 2D heterogeneous models[5, 6, 10, 23]. This is a consequence of the multiple flow pathways provided by the 3D heterogeneous porosity network for mobile phase flow to a producing well. The incorporation of the actual reservoir geometry and geological features also has a major effect on the nature of gas flow in the reservoir. Dissociated gas is driven by buoyancy forces up-dip towards the assumed sealing

fault at the west boundary, as they are being produced. If the fault boundary was non-sealing in reality, it would provide conduits for "leakage" of dissociated gas, thereby reducing reservoir performance. However, the full 3D reservoir structures of Figure 3-7 show that the discontinuity in lithology caused by the fault offset could indeed provide a seal against any gas flow, and therefore the initial assumption seems justified.

Reservoir performance evaluation

Recovery factor is a very important index of reservoir performance. In this study, it is defined as the cumulative volume of gas produced from a well system at a particular time expressed as a percentage of initial gas-in-place (GIP) in form of hydrates. Table 3-6 summarizes the cumulative volumes of gas produced and the recovery factors achieved in each sand unit after 30 years, for the selected four well configurations whose results have been discussed in the previous sections.

Table 3-6: Cumulative gas volumes and recovery factors at 30 yr using different well designs

Sand Unit	Initial Gas in Place, 10^8 ST m^3 (BSCF)	Well Configuration	Cumulative Gas, 10^8 ST m^3 (BSCF)	Recovery Factor (%)
D	7.37 (26.03)	Well-1	2.32 (8.19)	32
		Well-2a	2.70 (9.54)	37
		Well-3a	2.93 (10.35)	40
		Well-L2a_1	2.98 (10.52)	40
C	10.65 (37.61)	Well-1	3.00 (10.59)	28
		Well-2a	3.24 (11.44)	30
		Well-3a	2.72 (9.61)	26
		Well-L2a_2	4.28 (15.11)	40
Overall	18.02 (63.64)	Well-1	5.32 (18.79)	30
		Well-2a	5.93 (20.94)	33
		Well-3a	5.65 (19.95)	31
		Well-L2a	7.27 (25.67)	40

Interestingly, the ranges of recovery factors show that the depressurization seems to be more effective in D compared with C for all well configurations except Well-L2a, despite the warm temperatures of the C sand. One reason for this may due to the presence of the hydrate–water contact along more than a half length of the C unit (Figure 3-8 and Figure 3-9). The water influx during production competes with gas flow and decreases the performance of the unit. The effect of water contact on gas production is discussed in more details later in a subsequent section. Well perforation lengths in the hydrate bearing sands could also be a contributing factor to the higher recovery achieved in D as in the case of Well-3a, where Table 3-3 shows that the length of perforation in the D sand (183 m) is greater that in the C sand (150 m). An estimate of the relationship between the perforation lengths (Table 3-3) and recovery factor (Table 3-6) is shown in Figure 3-15.

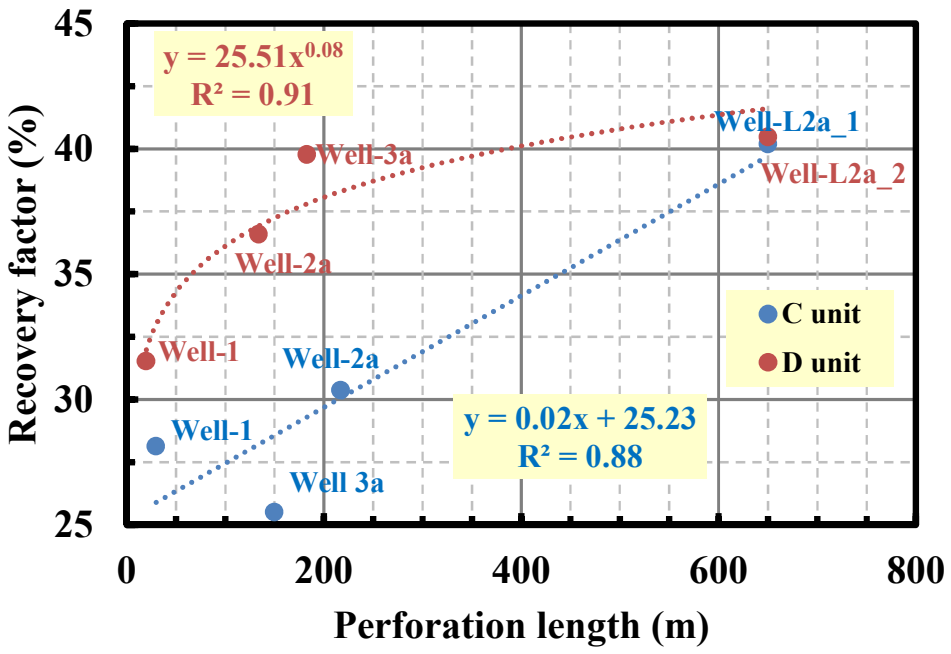

Figure 3-15: Recovery factors with varying well perforation lengths in D and C sands

From the figure, a linear relationship between perforation lengths and recovery factors in the C sand can be inferred, compared with the non-linear relationship in the D sand. Furthermore, comparison of the slopes of the fitted curves suggests that recovery in the D sand would respond more to increase in perforation length for lengths ≤ ~ 150 m. However, stronger dependency of recovery factor on perforation length in the C sand is suggested for lengths > 200 m. Overall recovery factors achieved in all well configurations are in the range of 30 – 40 %. In other words, less than half of the initial GIP is recovered at the end of the production period in the best performing well. This suggests a need for the application of a more advanced recovery technique to enhance reservoir performance within a typical life span of a producing well[32].

Water production

Water production rates and cumulative volumes predicted from all well configurations are compared in Figure 3-16. After a sharp rise in the beginning of production, the rates from all wells monotonically decrease. The bi-lateral wells (Well-L2a) has the highest water production rates with a peak of about 4000 ST m^3/day (~ 25 Mbbl/day) in the early period of production and, after two years, water production rates from Well-2a fall below those from other wells. In the period from 5 yr to the end of the production, water rates from all well configurations drop from a range 200 – 650 ST m^3/day (1300 – 4000 bbl/day) to 20 – 86 ST m^3/day (125 – 540 bbl/day) with the vertical well (Well-1) have the highest water production rates until 20 yr. In the period within the last 10 years, water rates remain fairly constant with the inclined well (Well-2a) having the highest rates. At the end of the 30 yr period, a total of 2.74×10^6, 3.58×10^6, 3.28×10^6 and 3.61×10^6 ST m^3 (17.2, 22.5, 20.6 and 22.7 MMbbl) of water is produced by Well-1, Well-2a, Well-3a and Well-L2a, respectively.

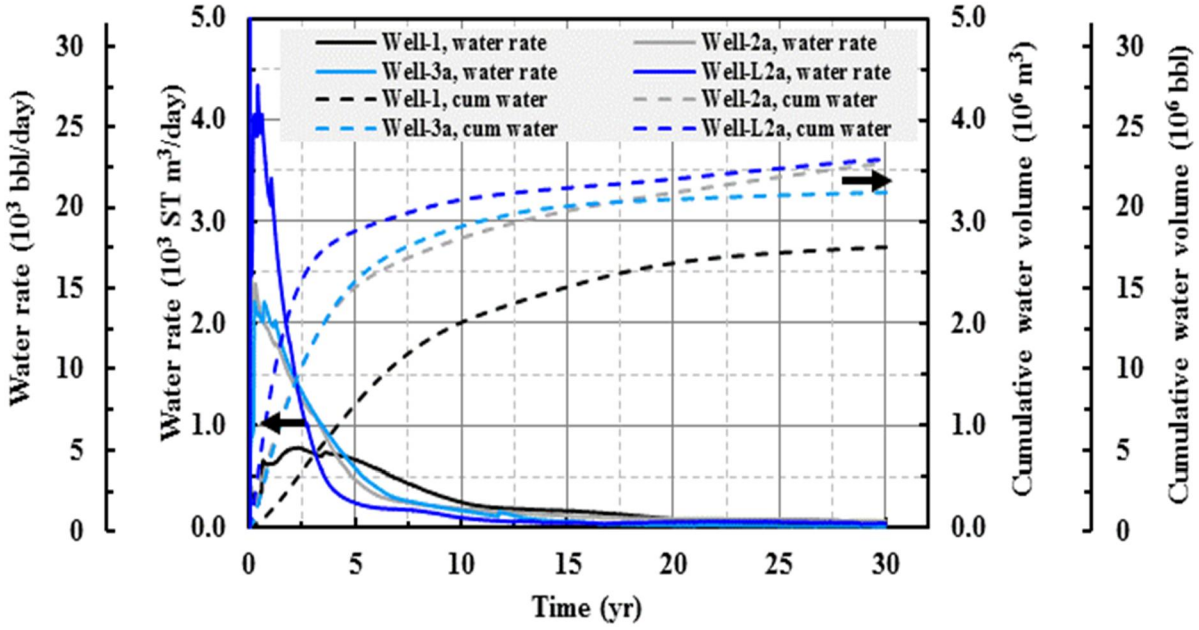

Figure 3-16: Water production rates and cumulative volumes for different well configurations

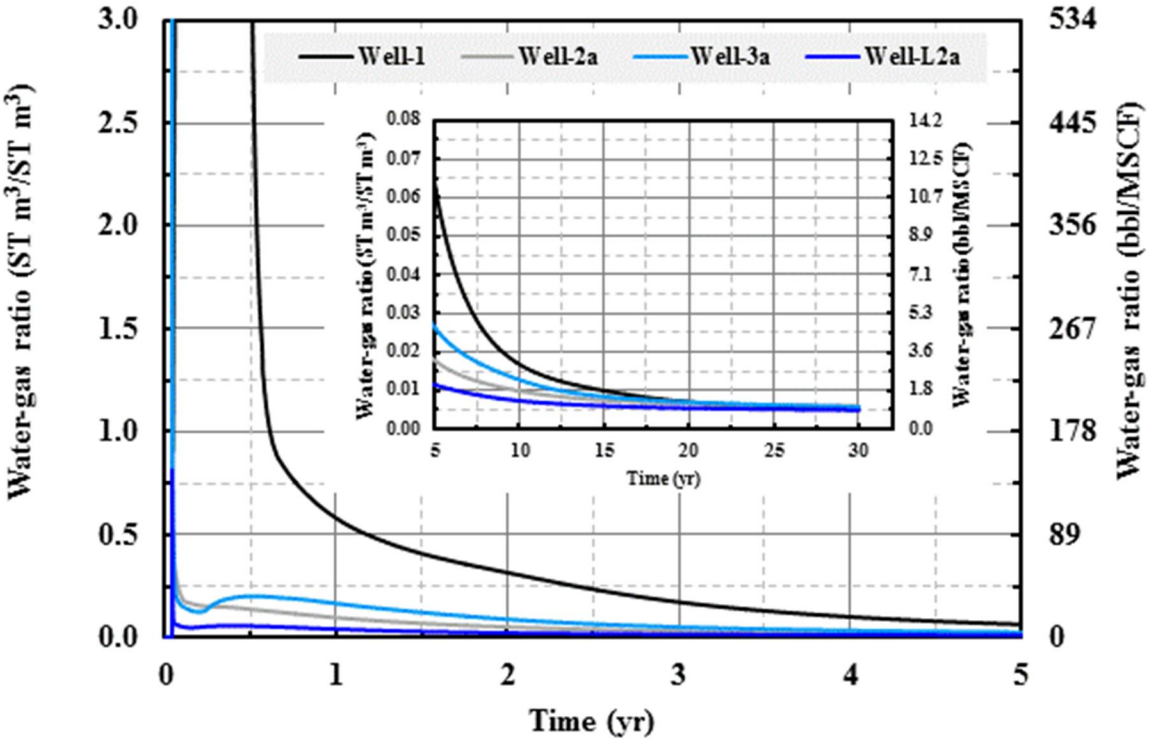

Figure 3-17: Cumulative water-gas ratios obtained using four different well configurations in the first five years of production. Inset graph shows ratios obtained from 5 – 30 yr.

These large amounts of liquid phase suggests a provision for downhole gas-water separation in the wellbore design in order to reduce the load on the production lift system by providing gas and water transportation to the surface using different flow lines.

An important criterion of effectiveness of a certain production scenario is a water-to-gas ratio which can be used together with a gas rate value to conduct technical and economic estimations of production at a selected site. Figure 3-17 shows computed cumulative water-to-gas ratios for the four well configurations as a function of time. At the onset of production the ratios are very high, however, they fall very rapidly to values within the range 0.04 – 0.57 ST m^3/ST m^3 (0.36 – 3.56 bbl/MSCF) in the first year, with Well-1 significantly having the highest ratios at this time. Water-gas ratios remain highest in Well-1 until about 20 yr, however, beyond this time, the ratios in all well configurations converge and remain fairly constant at ~ 0.005 ST m^3/ST m^3 (0.89 bbl/MSCF) for the rest of the production period. The double-lateral (Well-L2a) has the least water-gas ratios during the entire production period. The range of ratios obtained in the vertical well (Well-1) between the period 1 – 2 yr (0.31 – 0.57 ST m^3/ST m^3) can be compared with previously estimates for the same or similar hydrate formations. Moridis et al.[33] used a homogeneous approximation for porosity and hydrate saturation for the PBU L-Pad 2D reservoir model to predict the ratio range within 0.18 – 0.25 during the first 2 years of production (vertical well). The model utilized simplified impermeable shale units precluding water influx into production stream from over- and underburden which effectively decreased the ratio. Predicted production from the vertically-heterogeneous Mount Elbert reservoir model adopting low-permeable shale layers resulted in the ratio spreading from 0.01 to 0.56 during 30 years of reservoir performance (Myshakin et al., 2011). This is very much comparable to the predictions in this study in which the overall range of ratios produced by the

vertical well is in the range 0.005 – 0.57, since after the first year. Apparently, in spite of the differences in initial porosity/saturation/permeability representations, geometry of a reservoir and number of hydrate units involved, the water-to-gas ratio is relatively consistent for those reservoir models. This provides more confidence to the estimates for water management based on the simplified reservoir models.

3.6.3 Effect of Water Contact

The purpose of this section to discuss the implications of the presence of hydrate water contact on the reservoir performance. Gas and water rate predictions from three model scenarios are compared. The reference case (*wc_closed*), described in the previous section, is the model with a hydrate-water contact at 686 m and produces from a vertical well (Well-1) which is not perforated in the free-water zone below 686 m. The second case (*wc_open*) is similar to the reference case except that Well-1 is perforated in the free-water zone. The third case (*no_wc*) assumes an impermeable formation in place of the free-water zone (i.e. a Class 3 reservoir). Figure 3-18 shows *wc_open* produces the highest initial gas production rates within the first 7 years of production, with *no_wc* producing the lowest during this time interval. The reason for the initial high gas rates in *wc_open* can be attributed to the better hydraulic connection between the bottom C sand and the free water zone, therefore making depressurization more effective (which is less so in *wc_closed* and *no_wc*, respectively). Figure 3-20 (a) shows the pressure distributions in wc_open and no_wc, respectively after 7 years.

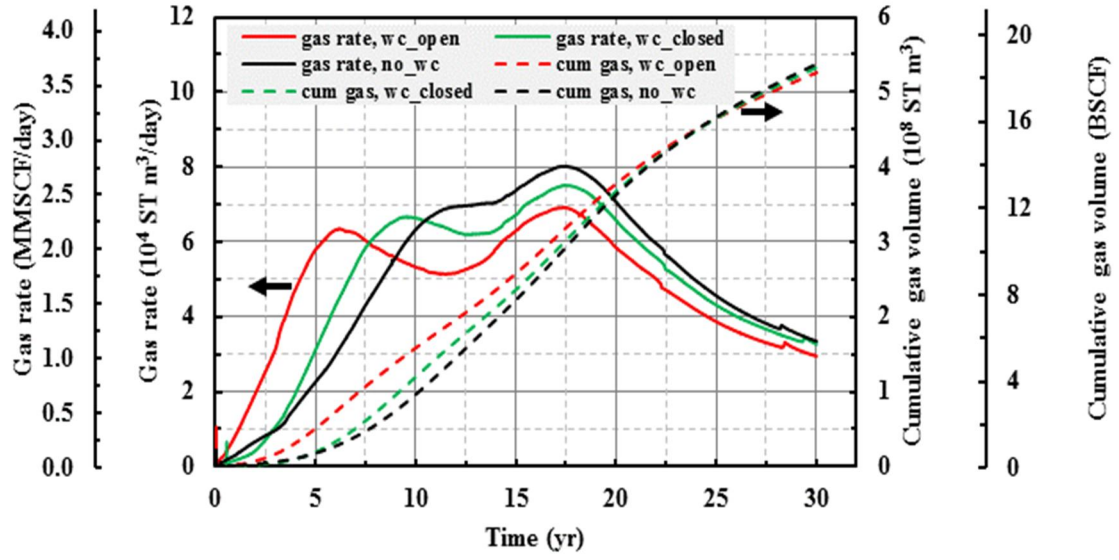

Figure 3-18: Effect of water contact on gas production rate and cumulative gas volume

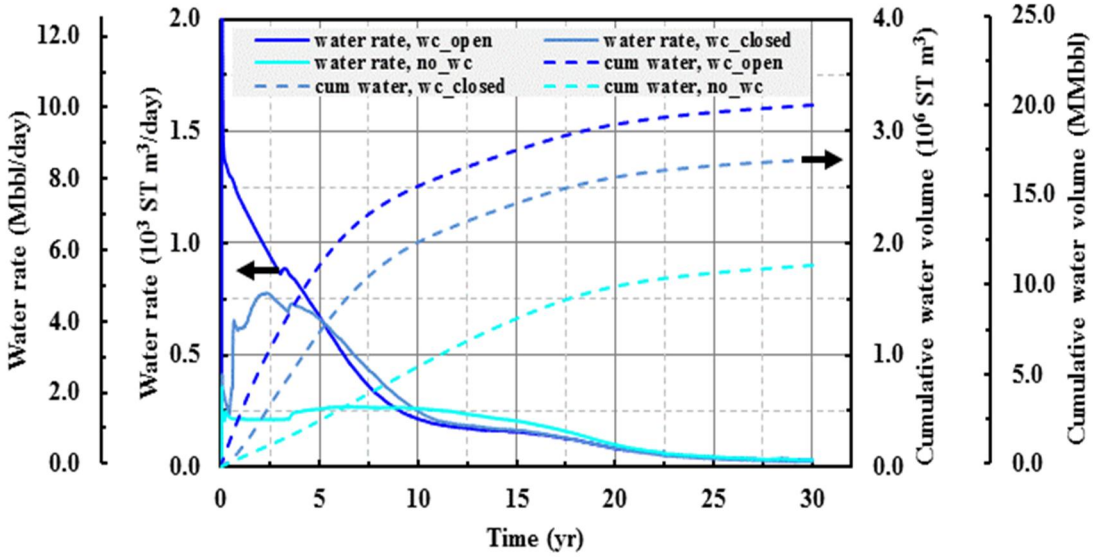

Figure 3-19: Effect of water contact on water production rate and cumulative water volume

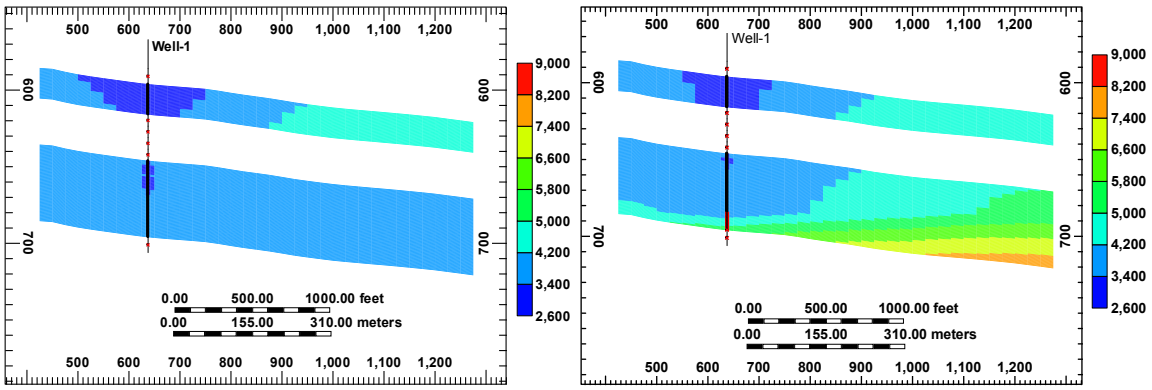

(a)

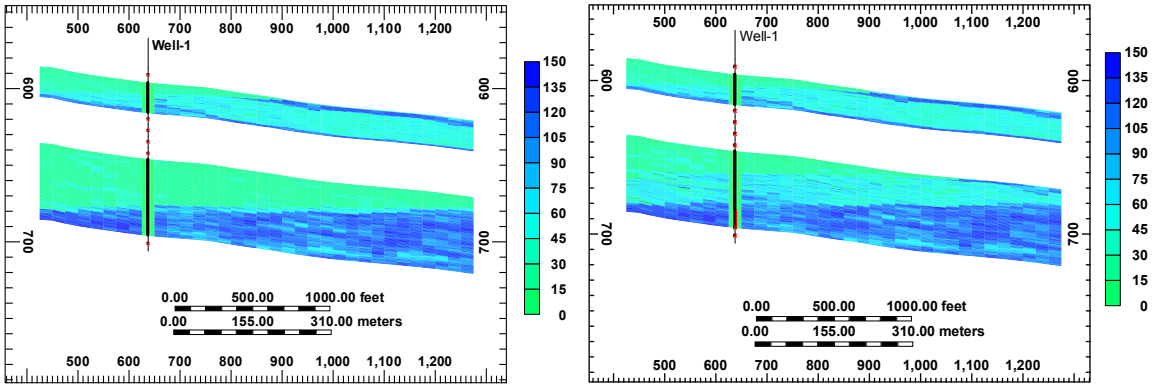

(b)

Figure 3-20: Vertical cross sections across wellbore showing a) pressure distribution (kPa) at 7 yr, (b) residual water volume distribution (m^3) at 30 yr, in models with wells perforated in the free-water zone (*wc_open*, left column) and no water contact (*no_wc*, right column)

The lower reservoir pressures in the cross-section for *wc_open* provide evidence that the ability to propagate the depressurization front from the well farther into the reservoir drives the production rate during the first 7 years. Initial high gas rates in the *wc_open* model is also accompanied high water production rates shown in Figure 3-19. As the free-water is being produced, the hydraulic communication advantage of a perforated free-water zone is reduced and gas rates in *wc_open* begin to drop below those of the other two cases. Furthermore, later in the production period, flow of mobile water begin to 'compete' with gas flow, leading to a reduction in the effective permeability of the reservoir to gas and, consequently, gas production rates. At the end of 30 years, Figure 3-18 shows that cumulative gas volumes produced in all three cases converge to about 5.4 x 10^8 ST m^3 (16.5 BSCF). However, Figure 3-19 shows that cumulative water volume produced in *wc_open* is the highest at 3.25 x 10^6 ST m^3 (~ 20 MMbbl), which is 90 % more than the volume produced (1.7 x 10^6 ST m^3 (~ 11 MMbbl)) in the model with no water contact (*no_wc*). This results to a higher residual water volume in the C sand in *no_wc* than *wc_open*, at the end of the production period (Figure 3-20 (b)).

3.6.4 Gas Flow and Secondary Hydrate Formation

Many researchers have expressed significant concerns about secondary hydrate formation because of its potential adverse effect on production potential[5-7, 9, 11, 12, 15, 23, 34, 35]. In these simulations utilizing 2D models a hydrate barrier evolves around the well bore because the reservoir pressure and temperature conditions are shifted into hydrate stability zone owing to heat absorption by the hydrate lattice decomposition reaction, the Joule-Thomson effect of gas exiting from the well bore, and salinity reduction that shifts the position of the phase equilibrium curve. The barrier impeded gas flow to a well bore causing substantial reduction of gas rate and, in severe cases, completely cut off gas flow to the well.

The 3D heterogeneity introduced in the reservoir model employed in this study delivers a natural possibility for gas flow to divert areas with reforming hydrate (should such occur) and, thus, mitigates its unfavorable effect on gas rate. The heterogeneous permeability model presented in this study allows for the faster hydrate dissociation in the areas with high local permeability values which, in turn, leads to evolution of preferential flow paths for mobile phases in the 3D porous space. Figure 3-21 depicts flow vectors of gas phase (blue arrows) captured after 10 years of production. The red lines indicate streamlines representing the preferential pathways for gas flow calculated from block face-based gas phase velocities. The preferential pathways of maximum velocities for gas flow are not necessarily directly connected to the producing vertical well shown as the point of blue arrow convergence.

Figure 3-22 illustrates gas flow in the region of high hydrate saturation in the reservoir. It reveals that flow directions change reflecting the complexity of pore network and variability in intrinsic permeability. With this kind of flow pattern, it is very much unlikely that possible hydrate reformation in the reservoir would completely cut off mobile phase flow from the reservoir to the wellbore, as predicted by homogeneous 2D models.

To explore possible secondary hydrate formation, a code was developed to scan and analyze time-dependent 3D hydrate saturations in order to identify sustained increase of hydrate accumulations in the reservoir persisted for more than 2 months. The results of analysis show absence of any signs of secondary hydrate formation emerging in the vicinity of vertical and inclined well bore completions. Instead, the only noticeable increases of hydrate saturation level are found in a few areas away from the wells. Their appearance is related to local increase of transient pressure fluctuating within the hydrate stability zone and attributed to gas trapping in those regions[36].

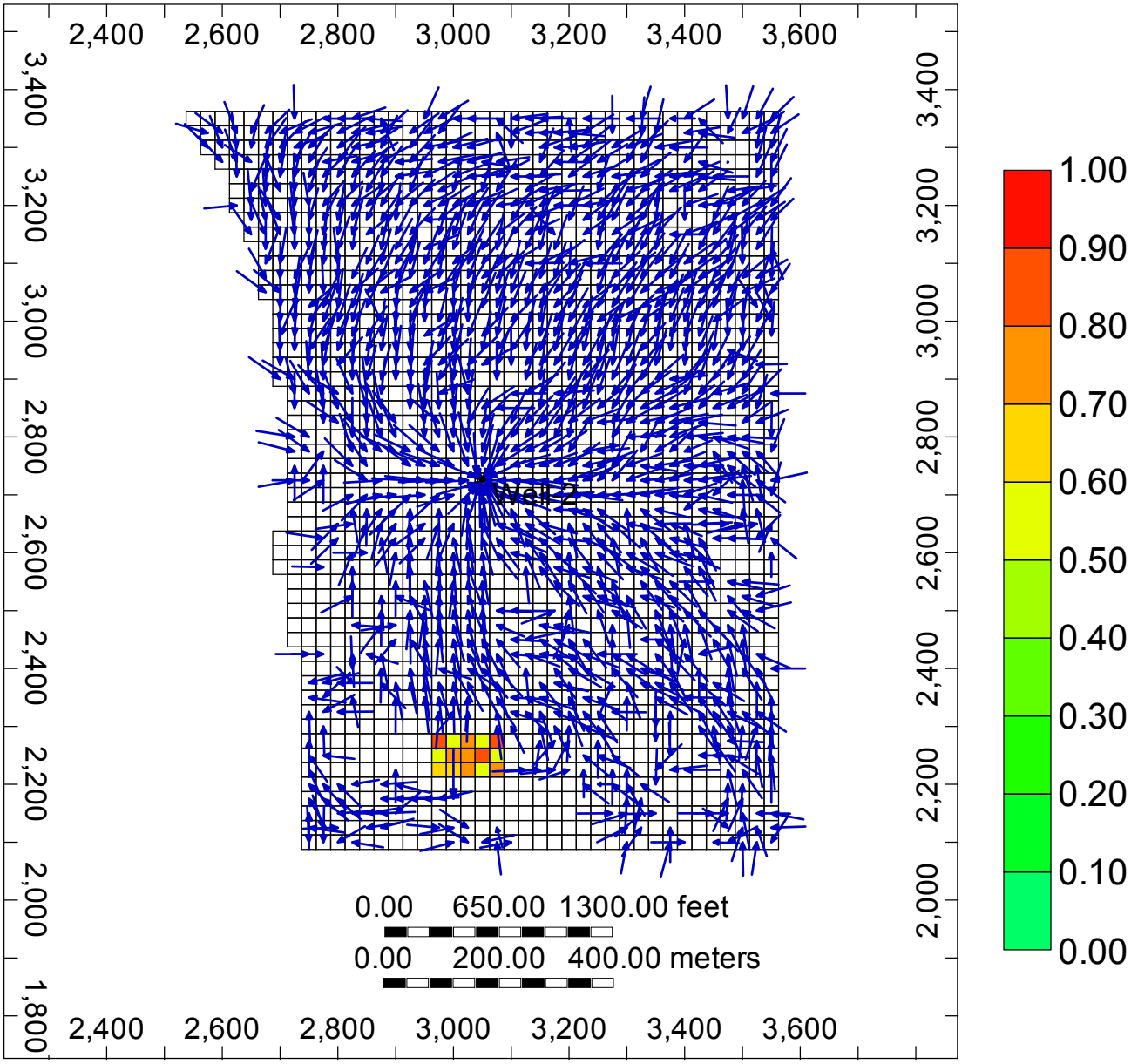

Figure 3-21: Top view of the middle layer of Unit D at 10 yr showing gas flow vectors (blue arrows), streamlines (red lines) pathways and the location of a reformed hydrate patch of blocks

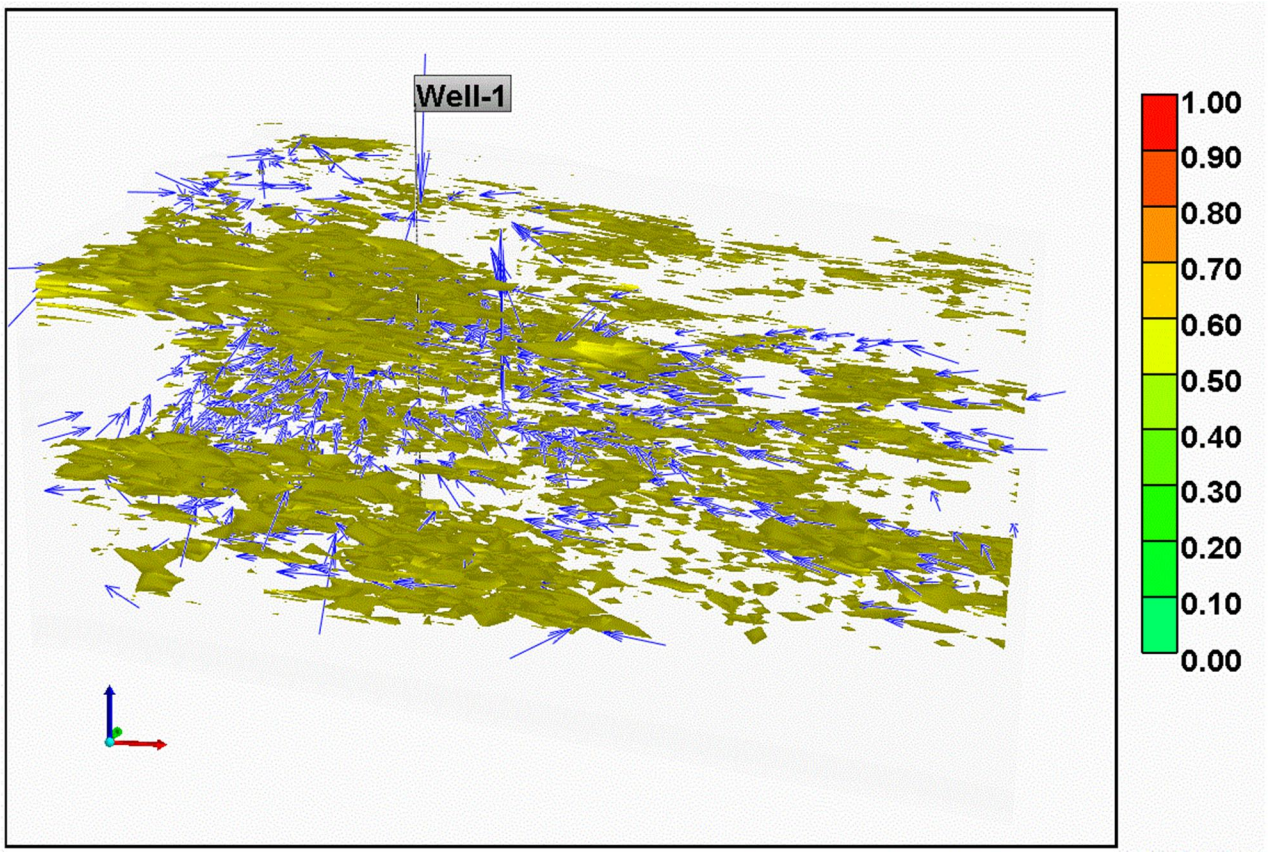

Figure 3-22: Gas flow vectors (blue arrows) around high hydrate saturation regions (S_h > 0.70) in a heterogeneous 3D porous network

As hydrate continuously decomposes in adjacent areas it eventually creates pathways to release trapped gas and initiate dissociation of reformed hydrate. Such secondary hydrate formation is shown in Figure 3-22 (a) as a "patch" of grid blocks with the nearby flow vectors pointing away from or parallel to it. This is an indication that gas flow avoids the area on its way to the producing well. A similar flow pattern is observed in other cross sections (not shown), which reveal short-lived "patches" of secondary hydrate formation throughout the depressurization period. Similar temporarily reformed hydrate areas were predicted during hydrate decomposition in a laboratory-scale reactor[36], where CT images of the hydrate-bearing sample were processed to provide 3D heterogeneous porosity and phase saturations for the reactor model. During depressurization, transient hydrate reformation has occurred inside the dissociating sample in response to local pressure buildup. The result that is also supported in this work suggesting that 3D heterogeneous reactor models of hydrate cores could serve as a valuable instrument to study phenomena developing at a reservoir scale.

Hydrate reformation like that shown in Figure 3-22 does not interfere with sustained gas flow to a well. In the light of the foregoing analyses, secondary hydrate formation as an evolving barrier around a well bore shown by earlier studies[5-7, 9, 11, 12, 15, 23, 33, 34] could be related to the numerical simplifications in the 2D reservoir models rather than to an underlying physical phenomenon. However, the need for additional flow simulation studies using a 3D model similar to those developed in this work, has not been ruled out. Further research is still very much required to explore different scenarios of hydrate depressurization over a broad range of initial conditions before a definitive conclusion can be reached.

3.6.5 Effects of Reservoir Heterogeneity

Dimensionality of reservoir heterogeneity (2D *vs.* 3D)

The previous estimations of production potentials from the PBU L-Pad reservoirs were carried out by Moridis et al.[33] and Gaddipati[13], who utilized 2D models (based on a cylindrical symmetry of the deposit) and a vertical well completion to depressurize hydrate. Moridis et al.[33] used a 2D simplistic model with homogeneous porosity and hydrate saturation and uniform permeability values. The model was based on a subdivided C unit (C1 and C2), as inferred from log data obtained from L-106 and Ignik Sikumi wells. Production potential was estimated only for 2 years which is insufficient to conduct an adequate comparison. Based on Problem 7b of the International Code Comparison Project[23, 24], Gaddipati[13] presented results of a 30-yr flow simulation of gas production from the Unit C1 and C2 sands, with uniform permeability and vertical heterogeneity of hydrate saturation and porosity distributions (based on the composite LWD well log at L-106). These simplified 2D models did not incorporate actual reservoir geometry and geological features (like faults, dips, water contact, etc).

In order to isolate the effects of 3D heterogeneity of hydrate saturation and porosity on model predictions, a model based on a simple 3D rectangular geometry which adopts a geostatistical distribution of porosity and hydrate saturation was developed.

To provide a proper basis for comparison, the model also incorporated the following (mostly according to the description of Problem 7b):

- 18 m thickness each of D, C1 and C2 sands separated by impermeable intermediate shale formations, including 100 m thick each of overburden and underburden shale (Figure 3-23)
- Uniform horizontal and vertical permeability of 1000 mD and 100 mD, respectively
- Vertical well located at the center of the reservoir and perforated only in the C1 and C2 intervals

Other reservoir parameters are the same as those summarized in Table 3-2. A comparison of gas rates and cumulative gas volumes predicted using the 2D model by Gaddipati[13] and the model used in this study is shown in Figure 3-24. In the early stage of production, the gas rate from the 2D model is higher than that obtained from the 3D model and reaches a peak after 8 years. However after 11 years, higher gas rates are predicted by the 3D model which translates into a larger cumulative volume of produced gas after 17 years. At the end of production the 3D model provides about 62 % more gas volume (3.68 *vs.* 2.27 ST m^3 (13 vs 8 BSCF)) in comparison to the 2D model. Thus, using a 2D geometry with vertical heterogeneity of porosity and hydrate saturation significantly underestimates (by ~ 38 %) forecast made with the 3D model employed in this study.

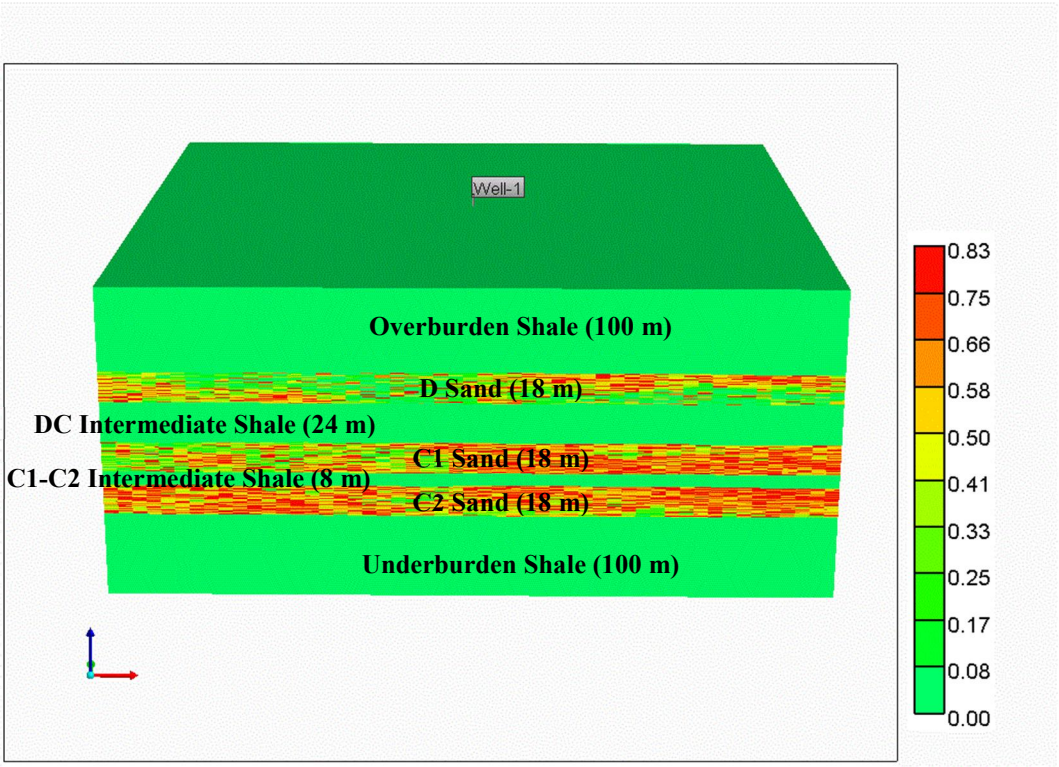

Figure 3-23: Rectangular reservoir model geometry (not to scale) showing 3D porosity-derived heterogeneous hydrate saturation distribution

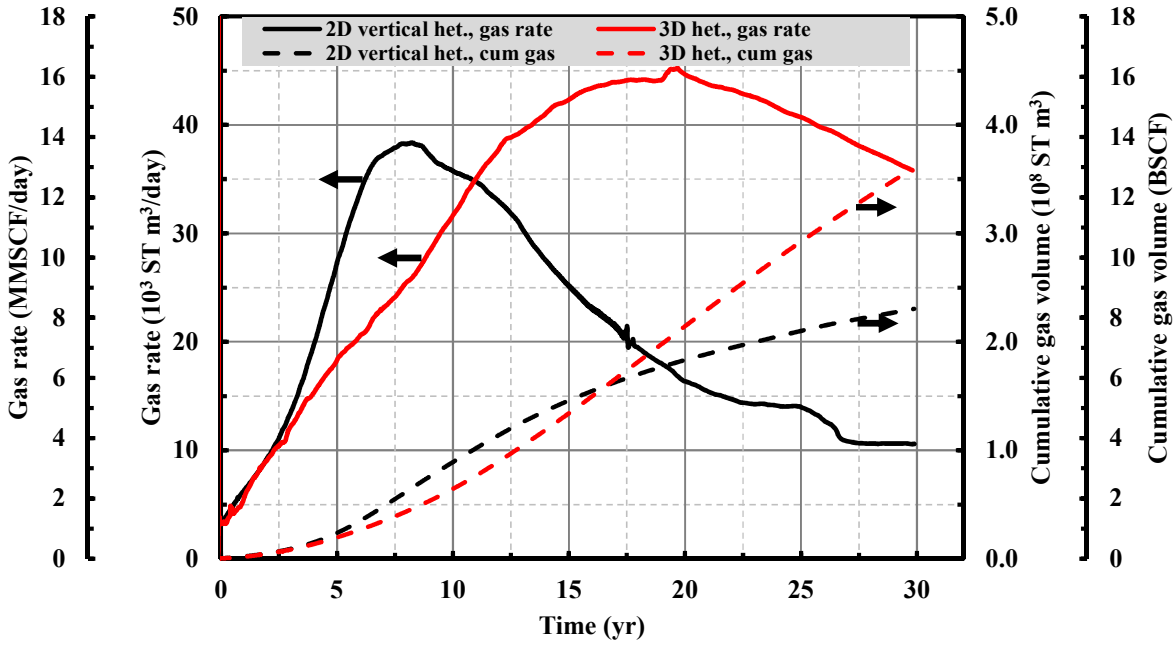

Figure 3-24: Gas rates and cumulative gas volumes using uniform permeability values predicted in this study ("3D") and reported by Gaddipati[13] ("2D").

Heterogeneity of permeability

In this section, the sensitivity analysis of intrinsic permeability representations is conducted to quantify their effect on production potential. Results presented here are based on the reservoir model discussed in the previous section with an inclined well configuration similar to Well-2a. Perforations are open in all three (D, C1 and C2) sand intervals. Two permeability representations were compared for that reservoir model. For the first model, permeability values of the hydrate layers were heterogeneous following the geostatistical 3D porosity distribution. In the uniform permeability model, a constant value of 734 mD is specified for the horizontal permeability in the hydrate-bearing units, which is the pore-volume average of the porosity-correlated permeability distribution in the 3D model. An anisotropic factor of 0.5 is also applied to yield 367 mD for permeability in the vertical direction. In both models, permeability of the shale layers was set at 0.001 mD (horizontal) / 0.0001 mD (vertical). As can be inferred from Figure 3-25, gas rates obtained using the heterogeneous model are consistently lower than rates from the uniform permeability model in the first 25 years of production. This translates into an overestimation of the cumulative gas volume calculated with the uniform model by ~ 40 % when compared with the prediction of the heterogeneous model at a 30-year mark. An explanation of the higher production performance of the reservoir with the heterogeneous model in the last 5 years can be made from the plots of temperature distributions for both models after 25 years of production. During the first 25 years, the ability of the uniform permeability model to deliver more mobile phase flow to a production well dominates the reservoir performance.

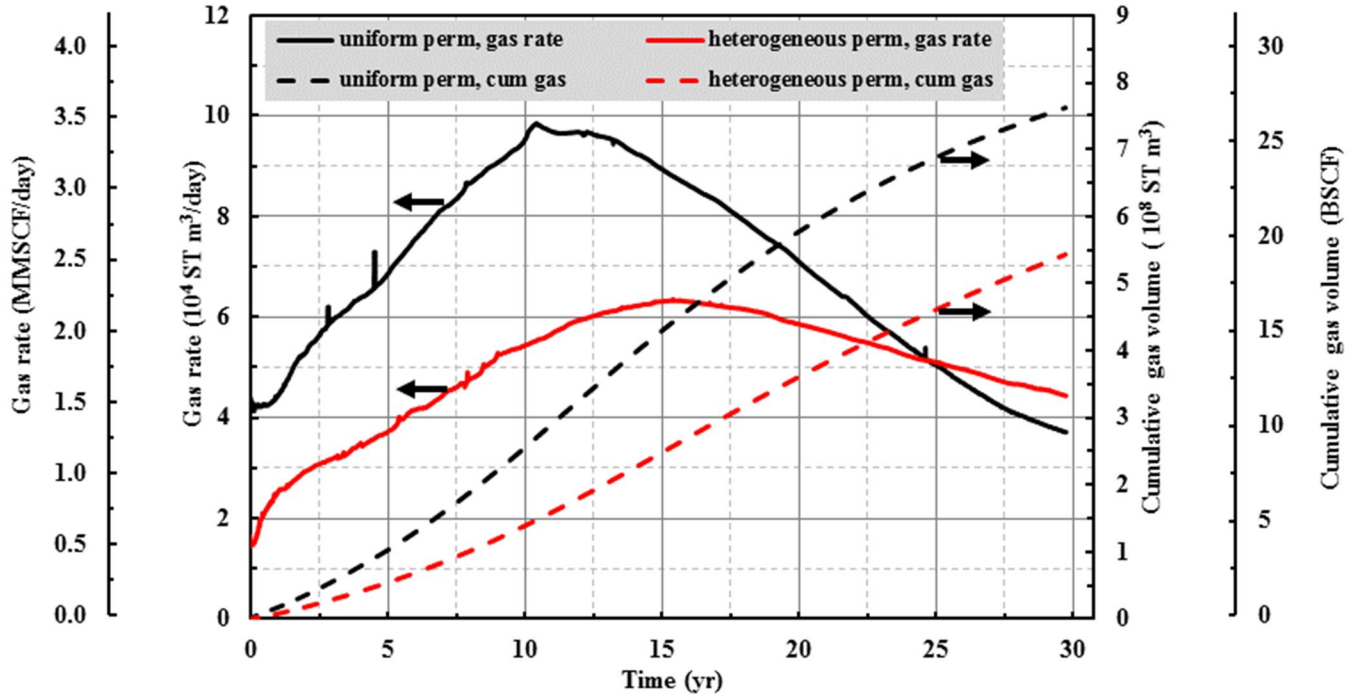

Figure 3-25: Gas rates and cumulative gas volumes produced from the inclined well using heterogeneous and uniform permeability models.

This implies a faster decomposition of the hydrate layers in the reservoir which is accompanied by deeper temperature drop (due to the endothermic nature of the hydrate dissociation reaction) comparing to the heterogeneous model.

Finally, after 25 years of production, temperature in the decomposing hydrate layers drops below 2 ^{0}C for the uniform model providing limiting sensible heat to support the decomposition reaction (Figure 14). As a result, the equilibrium conditions at the dissociating interface between hydrate and mobile phases moves toward the quadruple point that reduces ΔP (the difference between a pressure at the interface and the constant well BHP), the driving force for mobile phase flowing to the producing well. This reduction is greater for the uniform model in comparison to the heterogeneous one which is still capable to maintain dissociation at higher temperature regimes (Figure 3-26). At 25 years that parameter (ΔP) defines the higher gas rate predicted using the heterogeneous model in spite of greater ability to transmit mobile phases in porous media provided by the uniform model. The high transmissibility is a key factor for performance in early years of production when significant gas volumes are released into the reservoir.

An interesting observation can be made from these results and those reported in the previous section. Considering only a simplistic 2D representation of the reservoir domain with vertical heterogeneity for porosity and hydrate saturation distributions, the predicted gas volume at the end of the 30 year-production period is underestimated by about 38 % when compared with the predictions from the 3D reservoir model using a geostatistical realization of porosity coupled with heterogeneous hydrate saturation. Both models were based on a uniform intrinsic permeability distribution.

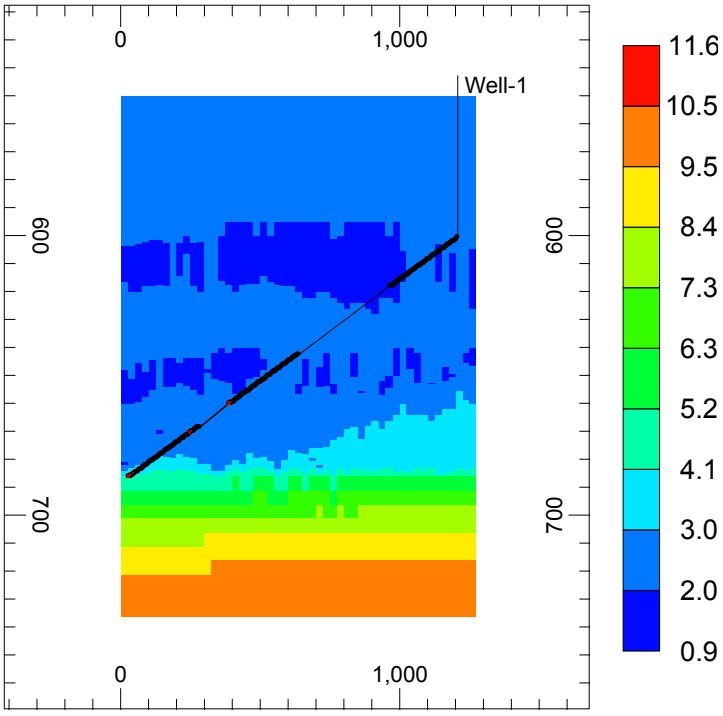

(a)

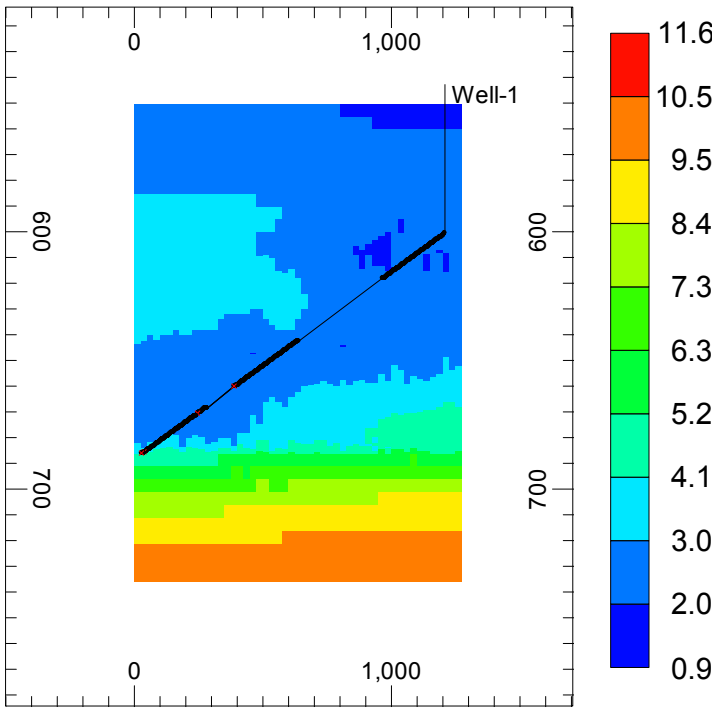

(b)

Figure 3-26: Vertical cross sections of temperature distributions (^{0}C) running along the inclined well after 25 years of production a) uniform permeability b) heterogeneous permeability. Dimensions are in meters.

On another hand, the uniform intrinsic permeability provides about 47 % more cumulative gas volumes than the heterogeneous permeability values based on the 3D porosity distribution. Thus, the production potential deviations, introduced through ignoring spatial complexity of porosity coupled with hydrate saturations and by means of uniform permeability of porous media, occur in the opposite directions. Due to limited field data, in many applications of numerical simulations to estimate production potential of gas hydrate accumulations, a 2D geometry, homogenous or vertical heterogeneous representations of porosity and saturations, and uniform intrinsic permeability are a common choice to describe a reservoir model[5-7, 9, 11, 12, 15, 23, 33, 34]. In light of results obtained in this work, simplification of reservoir models may have been justified owing to the potential cancellation of the errors introduced by approximations. Therefore, homogeneous 2D models are still very much valuable in obtaining first order predictions, particularly in the absence of field data to characterize the reservoir or when a sophisticated numerical simulator capable of handling the complexities associated with heterogeneous models is not available.

3.6.6 Flow Assurance

As mentioned in chapter 1, gas production by depressurization would require an artificial lift system e.g. a pump. Therefore, it is essential to correctly determine the right size of pump which will provide the necessary force to move the produced fluids from the bottom-hole to the wellhead, while also managing the wellbore pressure and temperature conditions to minimize the risk of secondary hydrate formation in wellbore.

CMG STARS provides an explicit means of coupling reservoir flow simulation models with wellbore models using well-established pressure drop and heat loss calculations for multiphase flow[31].

A simple wellbore artificial lift design with schematic shown in Figure 3-27 is proposed, based on the vertical well (Well-1) configuration described in Section 3.6.2. A pump will constantly take in fluid from the reservoir based on the predicted gas and water rates from the reservoir flow simulation model (Section 3.6.2) at a depth of 570 m (20 m above the first perforated hole in the D sand) at the well flowing BHP of 28 bar, and will discharge at the wellhead at the surface (depth = 0 m). The model assumes no water-gas separation occurs at the pump i.e. all reservoir fluids entering at the suction of the pump is produced at the wellhead. Wellbore completion parameters (Table 3-7) similar to the Ignik Sikumi well were assumed[37].

To select a base case design, a simple hydraulic calculation was done to determine a pump power output that will provide the minimum differential pressure required to lift a single-phase water to the wellhead at a flowing wellhead pressure (WHP) of 1.03 bar. This was calculated to be 26.25 kW and therefore, a pump power output of 30 kW was selected as a base case (after allowing for possible additional equipment pressure losses). To simulate production scenarios where desired WHP may be different from atmospheric, two other cases were run with pump power outputs of 50 kW and 100 kW, respectively. Simulations were run for five years.

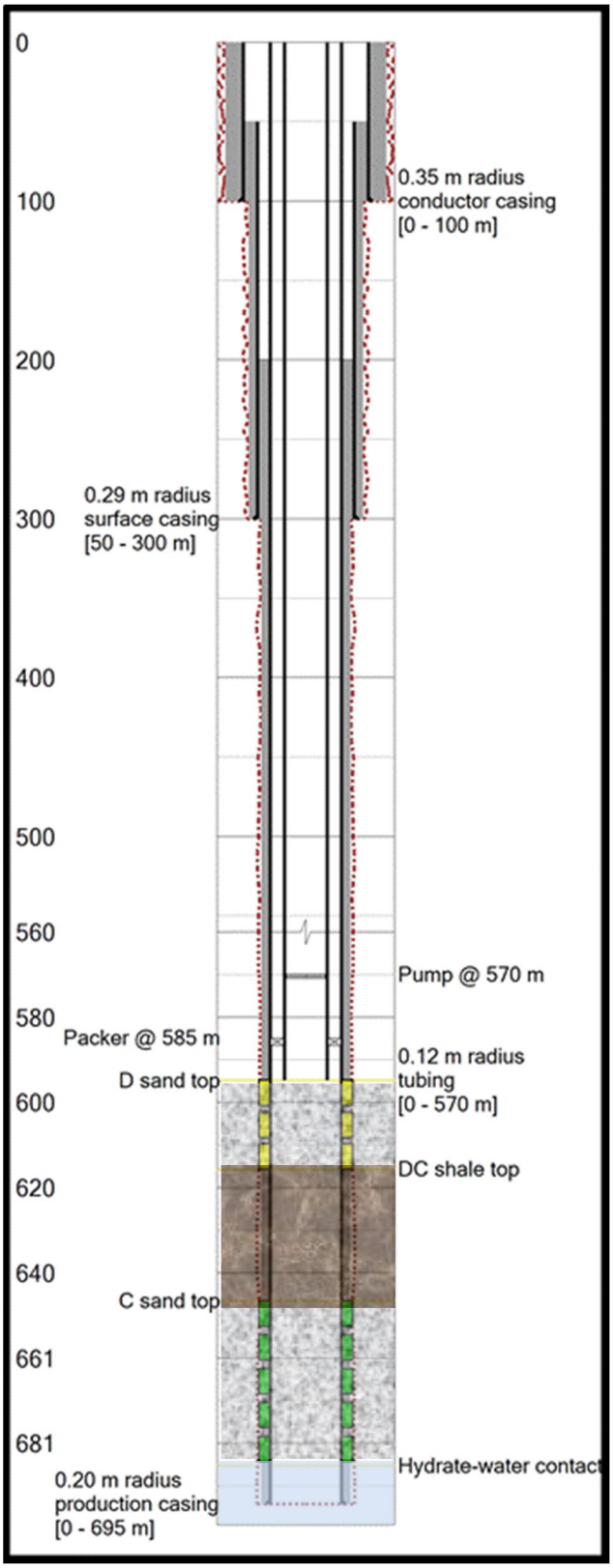

Figure 3-27: Wellbore schematic for artificial lift

Table 3-7: Wellbore completion parameters and formation properties

Wellbore, m		
	Wellbore length	596
	Inner tubing radius	0.11
	Outer tubing radius	0.12
	Inner casing radius	0.19
	Outer casing radius	0.20
	Surface hole radius	0.29
	Tubing relative roughness	0.0001
Thermal conductivity, W/m/K		
	Tubing wall	245
	Casing wall	245
	cement	3.5
	formation	17
Formation properties		
	Heat capacity, J/kg/K	886
	Geothermal gradient, ^{0}C/m	0.038
	Surface temperature, ^{0}C	0

Plots of the temperature-pressure profiles are shown in Figure 3-28, Figure 3-29 and Figure 3-30 for pump hydraulic power outputs of 30, 50 and 100 kW, respectively. A summary of the comparison among the three cases is presented in Table 3-8. Results show that operating with a 30kW output-pump would provide a discharge pressure of about 55 bar (804 psi) initially, and will drop down to 40 bar (587 psi) at 5 yr. Wellhead pressures during the five year period are near atmospheric in the range 1.8 – 3.2 bar (26 – 46 psi) and wellbore conditions are outside the hydrate formation zone for most of the period. However, at 0.5 and 1 yr, there are tendencies for hydrate formation in the bottom-most 81 and 10 m-sections of the wellbore. Observations can be made in a similar fashion about using 50 kW and 100 kW pump power outputs. The following deductions can be made, and are only specific to the gas and water rate predictions from the reservoir model on which the wellbore model is based:

- Production at atmospheric WHP (with 30 kW pump output) means it will take at least 15 days after production begins before ***first gas*** reaches the wellhead.
- Using a pump with 50 kW power output, it will take at least 5 yr of production before the possibility of hydrate formation is eliminated.
- With 100 kW, the wellbore is susceptible to secondary hydrate formation during the 5 yr period, with the entire wellbore length being at risk in the first two years

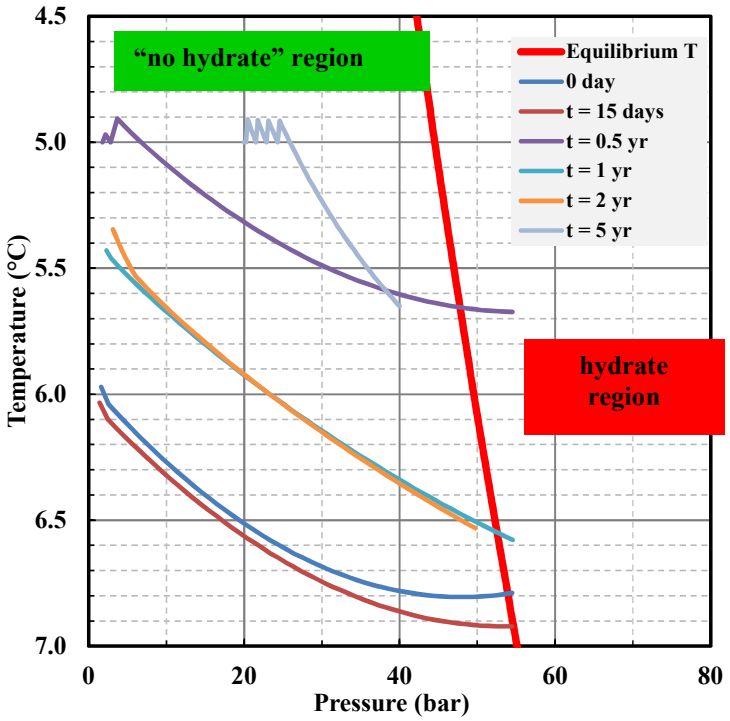

Figure 3-28: Wellbore temperature-pressure profiles with 30kW hydraulic output

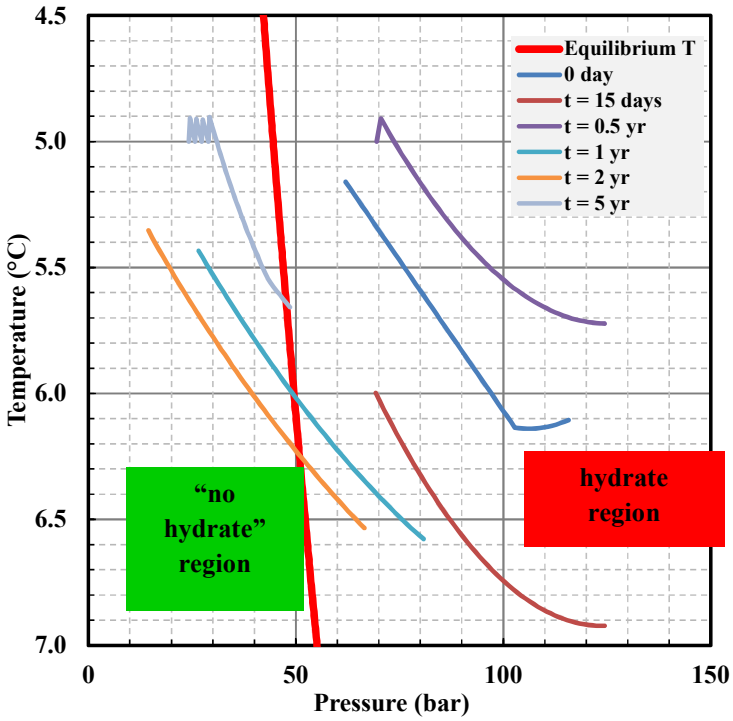

Figure 3-29: Wellbore temperature-pressure profiles with 50kW hydraulic output

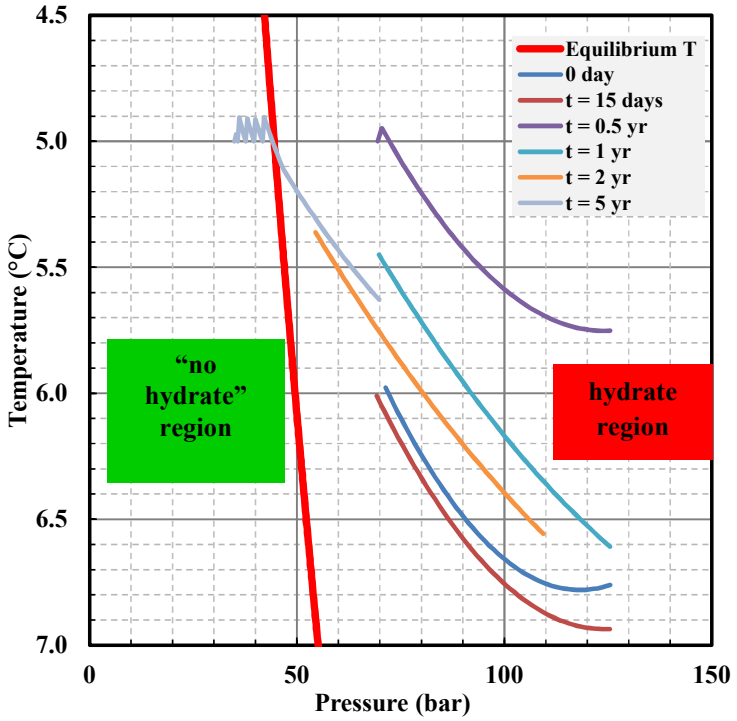

Figure 3-30: Wellbore temperature-pressure profiles with 100kW hydraulic output

Table 3-8: Summary of wellbore artificial lift design performance

Pump power output, kW	Time	Pump discharge pressure, bar (psi)	Wellhead pressure, bar (psi)	Hydrate propensity depth interval (m)
30	0 day	55 (804)	-	-
	15 days	55 (805)	-	-
	0.5 yr	55 (805)	1.8 (26)	489 - 570
	1 yr	56 (805)	2.3 (33)	560 - 570
	2 yr	51 (736)	3.2 (46)	-
	5 yr	40 (587)	2.0 (29)	-
50	0 day	117 (1697)	61 (885)	0 - 570
	15 days	125 (1819)	69 (1004)	0 - 570
	0.5 yr	125 (1820)	70 (1008)	0 - 570
	1 yr	82 (1186)	27 (385)	244 - 570
	2 yr	67 (979)	14 (210)	407 - 570
	5 yr	49 (716)	24 (351)	-
100	0 day	125 (1820)	69 (1006)	0 - 570
	15 days	125 (1819)	69 (1004)	0 - 570
	0.5 yr	125 (1820)	70 (1008)	0 - 570
	1 yr	126 (1821)	70 (1012)	0 - 570
	2 yr	109 (1586)	54 (790)	0 - 570
	5 yr	70 (1013)	35 (507)	244 - 570

- For a given pump power output, the fraction of wellbore length at the risk of secondary hydrate formation generally reduces with time. This suggests a possibility of the use of a higher pump power output as production progresses, without increasing any concerns of secondary hydrate formation.

In flow assurance, hydrate formation prevention measures such as methanol injection and direct electrical heating (DEH) are usually based on a target hydrate formation temperature depression (ΔT_{HYD}), which is the difference between the temperature at any pressure in a hydrate zone and the hydrate formation temperature at the same pressure. Preliminary calculations were done to determine the amount of methanol required and the minimum DEH heating power is required to maintain the wellbore outside hydrate formation conditions and the results are summarized in Table 3-9. The calculations were based on a maximum ΔT_{HYD} of 1.19, 9.28 and 9.25 ^{o}C for 30, 50 and 100 kW pump power outputs, respectively. The hand calculation method of Hammerschmidt[38] was adopted to estimate the minimum methanol injection rates, using the gas production rate at 5 yr (3.0 x 10^4 ST m^3/day (1.05 MMSCF/day), from Figure 3-12 for Well-1) and a water-gas ratio of ~ 0.3 (50 bbl/MSCF), which is the time-averaged value obtained over the period of the first five years (Figure 3-17, Well-1). The estimates were also based on the injection of a 100 wt % (pure) methanol and the assumption of negligible methanol losses to the vapor phase compared with the diluted (Hammerschmidt minimum[38]) methanol concentration in the aqueous phase. Results (Table 3-9) show that very large volumes of methanol need to be injected into the wellbore in order to achieve the required ΔT_{HYD}, making it impractical. These numbers, again emphasize the need for the provision of a downhole water-gas separation during production to reduce the pumping load and methanol injection, if necessary.

Table 3-9: Minimum methanol injection and DEH rates during the first five years of production using pumps with varying hydraulic power outputs

Pump power output, kW	**30**	**50**	**100**
P_{max}, bar	56	125	126
T (P_{max}), ^{o}C	5.67	5.72	5.75
T_{eq} (P_{max}), ^{o}C	6.86	15.00	15.00
ΔT_{HYD}	1.19	9.28	9.25
Methanol injection rate, m^3/day (bbl/day)	> 308 (1938)	> 2403 (15113)	> 2395 (15065)
Heating rate per unit length, W/m	8.73	68.05	67.83
T_w (^{o}C)	8.20	25.39	25.36

Minimum DEH rate calculations were based on the maximum total (gas + water) mass flow rates achieved during the first five years of production and ΔT_{HYD}. Table 3-9 shows that minimum DEH requirements are 8.73, 68.05 and 67.83 W/m heating power per unit length of wellbore, corresponding to the 30, 50 and 100 kW pump power outputs, respectively. Further calculations based on a Nusselt number (Nu) of 3.658 (for cylindrical pipes) show that these heating rates imply that the inside wall temperature of the wellbore (T_w) would be maintained at 8, 25 and 25 ^{0}C, when using a pump with power outputs of 30, 50 and 100 kW, respectively. These results suggest that DEH might be a more suitable alternative than methanol injection, in the absence of downhole water-gas separation.

3.6.7 Long-term Development and Economic Assessment

There is currently a very wide disparity in the understanding of the economic optimum number wells and well density (inter-well spacing) to be used in the development of conventional oil and gas fields[39-43]. However, there is an agreement among investigators that an optimum spacing can only be determined for a specific reservoir in a particular field, and that generalization of results to other fields may not be possible.

In this section, the economic viability of different options of development with multiple wells are evaluated. The main objective here is to conduct a preliminary study on the effects of well spacing, number of wells and type of well configuration on field production rates, cumulative gas volumes and the net present value of development of the L-pad gas hydrate field development over a 30 yr period. The foregoing analysis is based on the simple 3D rectangular reservoir models described in Section 3.6.5. The four different multi-well development scenarios considered are summarized in

Table 3-10 and illustrated in Figure 3-31.

All well configurations are centralized with respect to the boundaries of the reservoir model, and have perforated well sections along the entire interval of the D and C hydrate units. The 4I08 configuration was so designed to minimize well interactions in the colder D sand. Gas rates and cumulative volumes achieved from the entire field are plotted in Figure 3-32 are the results are summarized in Table 3-11.

Table 3-10: Multiple well development scenarios

Case ID	Description	Sensitivity relative to reference
4V30 (reference)	Four vertical wells at 30 acre-spacing	-
4V60	Four vertical wells at 60 acre-spacing	Spacing
9V30	Nine vertical wells at 30 acre-spacing	Number of wells
4I08	Four inclined wells at 8^0 to the horizontal	Well configuration

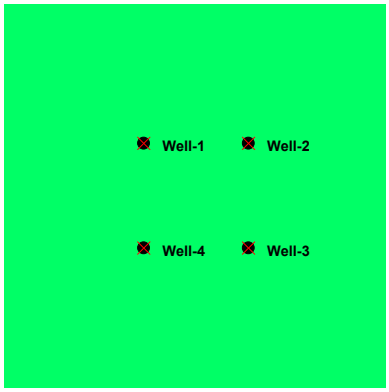

(a)

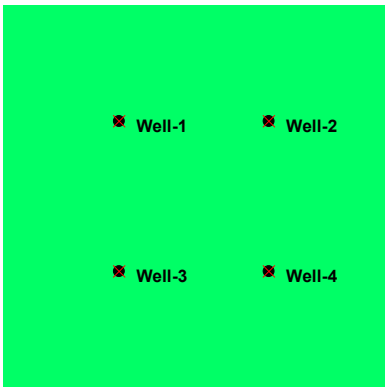

(b)

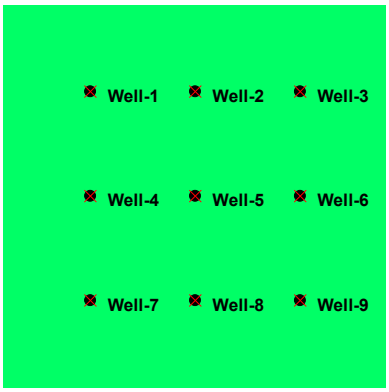

(c)

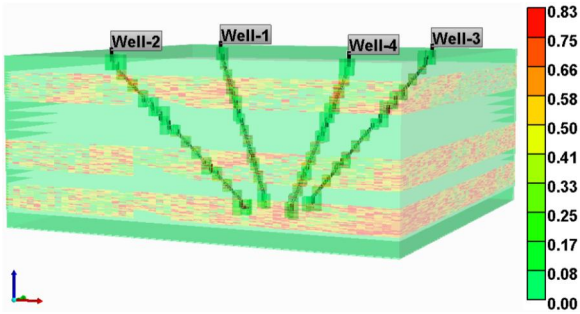

(d)

Figure 3-31: Multi-well development scenarios showing plan views of (a) 4V30, (b) 4V60, and (c) 9V30 and (d) 3D view of 4I08

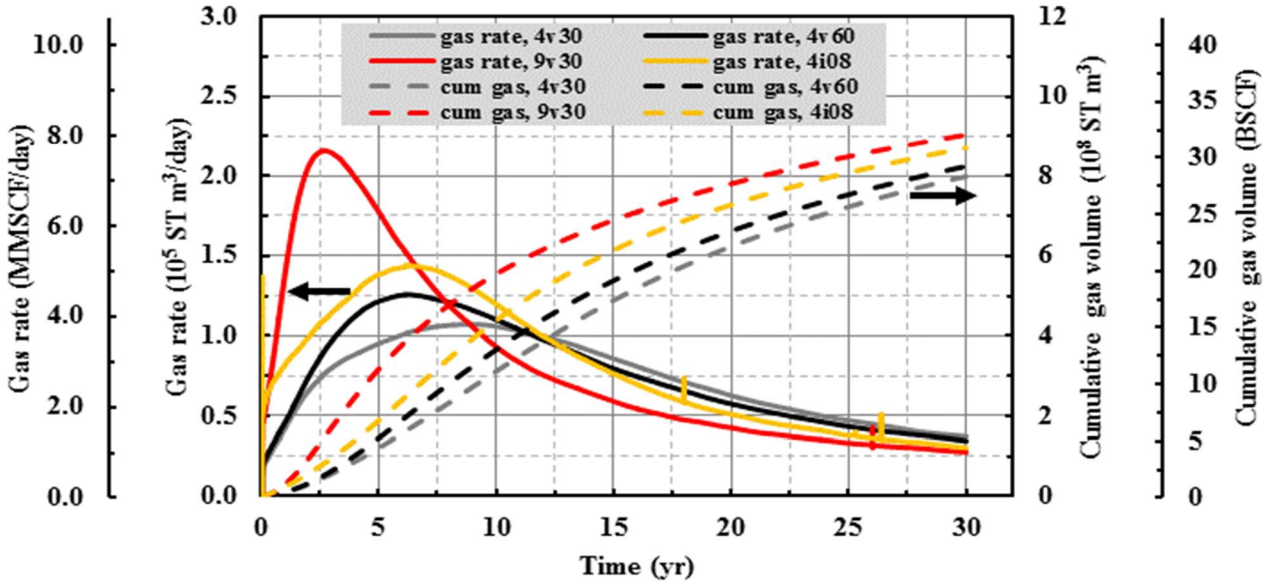

Figure 3-32: Gas rates and cumulative gas volumes produced in the entire field using different multiple well development scenarios

Table 3-11: Summary of results from development using varying field development options with respect to number of wells, well spacing and well configuration

	4V30	**4V60**	**9V30**	**4I08**
Peak rate, 10^5 ST m^3/day (MMSCF)	1.07 (3.78)	1.26 (4.44)	2.16 (7.63)	1.44 (5.10)
Time to peak, yr	~ 9	~ 6	~ 3	~6
Cumulative volume at 30 yr, 10^8 ST m^3 (BSCF)	7.98 (28)	8.25 (29)	9.03 (32)	8.70 (31)

The advantage of higher number of wells in 9V30 is evident only in the first three years during which rates are up to 3 times those from 4V30. After this period, gas rates decline for the remaining period, producing less than the 4V30 case in the last 21 years. Comparison between 4V30 and 4V60 also shows that increased well spacing produces a higher gas rates between 2 – 10 yr. During this period, 60 acre-spacing utilizes the wider drainage area around each well devoid of interference from other wells compared with the 30 acre-spacing, as evident in Figure 3-33.

After 10 years, the lower reservoir pressures surrounding the wells in the 4V60 case (< 4,000 kPa) decreases the flow potential from the reservoir to the wells, consequently leading to a lower gas production rates than 4V30 case which has a higher fluid flow driving force at the time, owing to higher surrounding reservoir pressures (4000 – 4400 kPa). The 4I08 case exhibits its advantage of a larger contact area with the hydrate sands only in the first 10 years, compared with the reference case. At the end of 30 years, cumulative volumes from all development scenarios are within a narrow range of 8 – 9 x 10^8 ST m^3 (28 – 32 BSCF). To provide an economic viewpoint, the net present values (NPV) and breakeven gas prices of each field development scenario are compared based on the parameters given in Table 3-12.

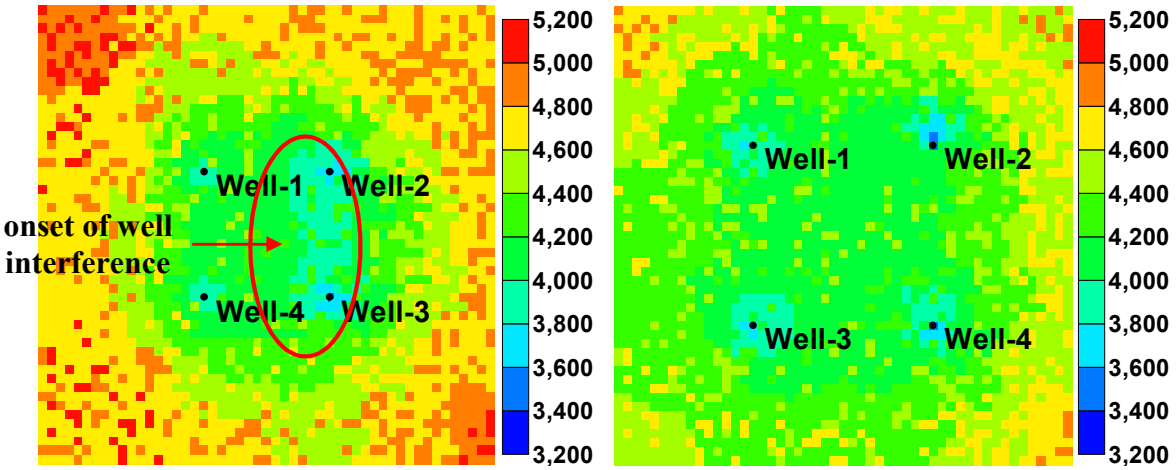

(a)

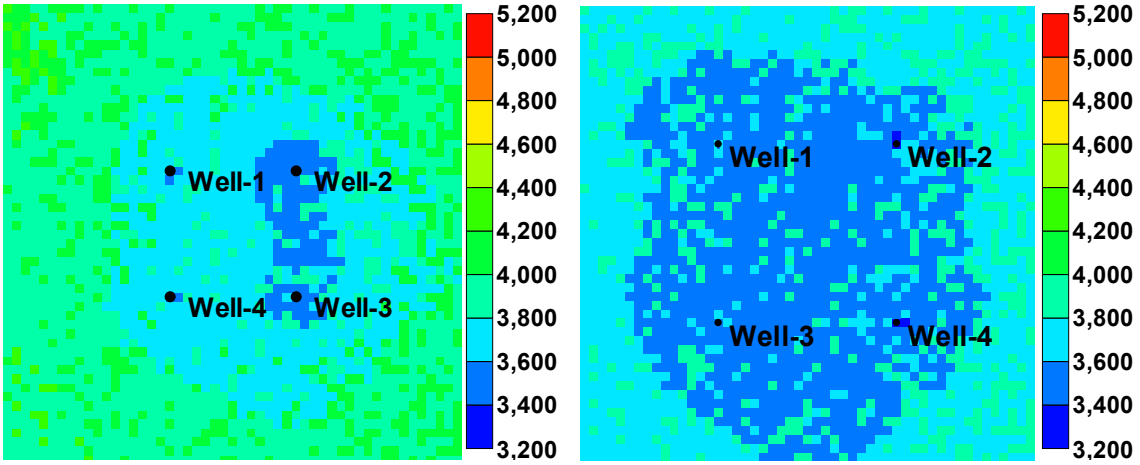

(b)

Figure 3-33: Pressure distribution in a horizontal layer (k = 82) after (a) 4 years, and (b) 10 years with 30 acre-spacing (4V30, left column), and 60 acre-spacing (4V60, right column)

Table 3-12: Parameters for economic assessment

Parameter	Value	Comments/reference
Wellhead gas price, $/MSCF	5.30	10 yr-average US national average[44]
Drilling cost per well, $ 10^6	15	3 yr-average[45]
Fixed costs per year, $ 10^6	1	
Operation costs, $/MSCF	0.15	Nyayapathi[46]
Discount rate, %	15	Myshakin et al[6]
Corporate tax rate, %	35	

The NPVs computed for all cases are plotted as a function of time in Figure 3-34 (a) and is expressed as a fraction of the reference case in Figure 3-34 (b). The NPVs and the breakeven gas wellhead prices at 30 yr are given in Table 3-13. Among the four scenarios considered, the most promising field development option is the use of four inclined wells (4I08), however, all of the options remain economically unattractive. Therefore an aggressive enhanced recovery method may be required to improve on the economic viability of long term production from this particular site.

Alternatively, focus may be shifted to investigating productivity from probable hydrate accumulations located downdip and to the east of the L-pad region. In the light of this, two models were developed to simulate production from reservoirs 50 and 100 m deeper (depth of Problem 7c[23]), which translates to reservoir temperatures 1.9 and 3.8 ^{0}C warmer than the original L-pad region (based on a geothermal gradient of 0.038 ^{0}C/m), respectively. These areas would be located 1.10 and 2.20 km, respectively, to the east of the original L-pad location (based on an approximate W-E dip of 2.6 ^{0}). The well configuration of 4V30 was used in order to facilitate a quick comparison to the reference case.

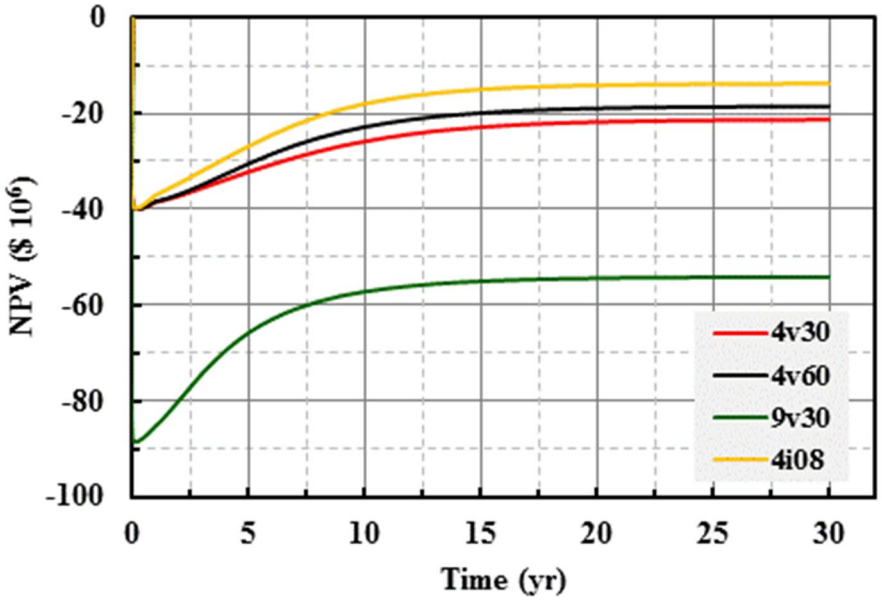

(a)

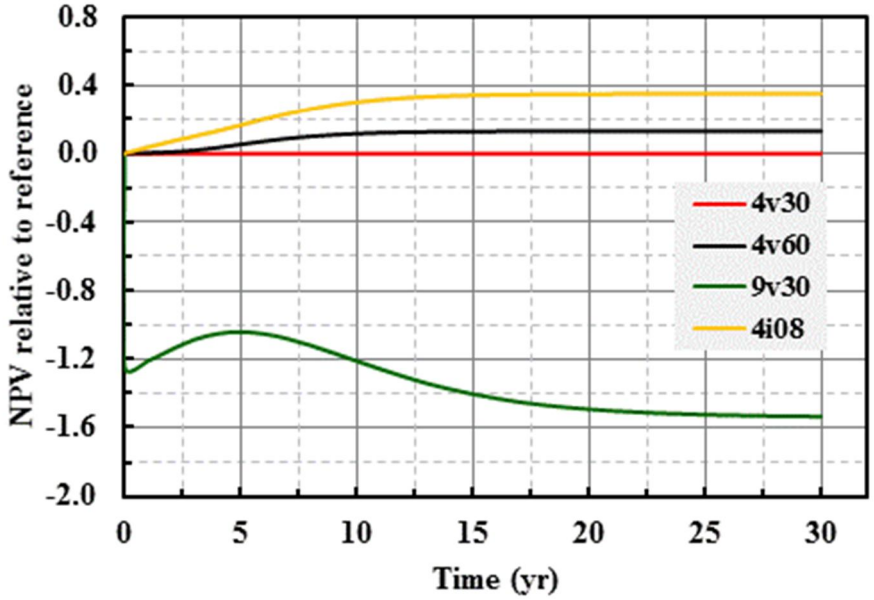

(b)

Figure 3-34: (a) NPV, and (b) NPV expressed as a fraction relative to reference case, for all field development scenarios

Table 3-13: NPV and breakeven gas wellhead prices at 30 yr

Case	NPV, $ 10^6	Breakeven price, $ / MSCF
4V30	-21.3	10.30
4V60	-18.5	9.16
9V30	-54.1	12.65
4I08	-13.8	7.71

Maximum gas rates achieved are 2.19 and 3.62 x 10^5 ST m^3/day (7.7 – 12.8 MMSCF/day) for the 50 and 100 m downdip models, which are 1.1 and 2.4 times more than the maximum production rate achieved from the original L-pad (4V30), respectively. Cumulative volumes achieved at the end of 30 yr (Figure 3-35), are 45 and 76 % more than the reference case for the 50 and 100 m-downdip models respectively. Using the parameters of Table 3-12, Figure 3-36 shows that the downdip models breakeven at ~ 22 and ~ 5 yr, corresponding to the 50 and 100 m models, respectively. At 30 yr, NPVs are $ 0.28 and $ 21.69 million, and breakeven gas wellhead prices are $ 5.27 and $ 3.58 per MSCF for reservoir depths 50 and 100 m, respectively.

While these results show that the L-pad downdip accumulations are much more promising production targets than the original L-pad, there is an increase in uncertainties in predictions owing to the geological risks associated with the site[2].

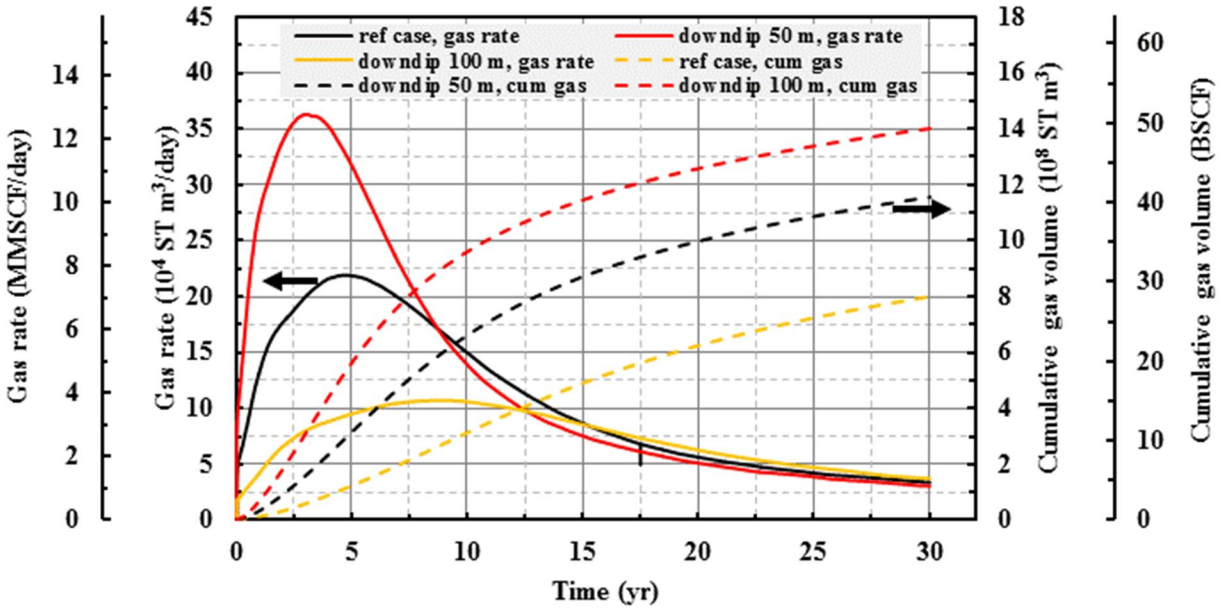

Figure 3-35: Gas rates and cumulative volumes of production from L-Pad Downdip

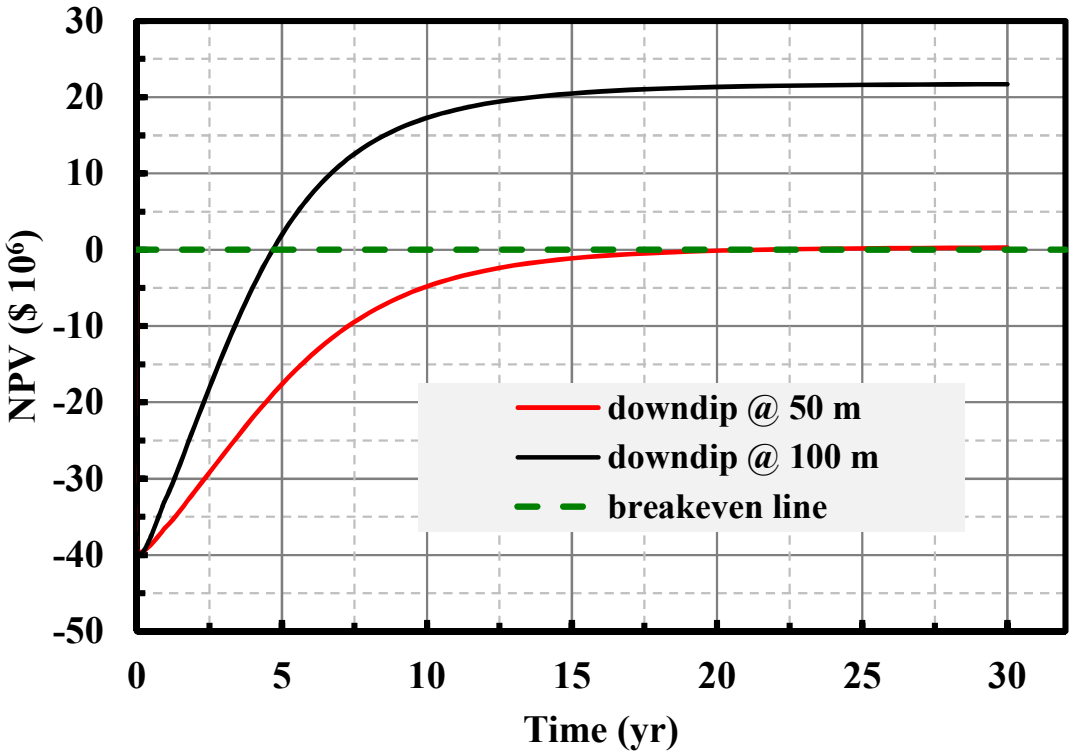

Figure 3-36: NPV vs time for L-pad downdip development

3.7 Conclusions

Numerical simulations were used to evaluate gas production potential of the reservoir based on the L-Pad methane hydrate deposit at Prudhoe Bay Unit on Alaska's North Slope. In order to incorporate the true nature of distribution of the reservoir geophysical properties, geostatistical porosity models of the hydrate-bearing D and C sand units were developed based on 78 well log data, from which distribution of porosity-dependent hydrate saturation and intrinsic permeability were estimated. Using reservoir models which account for the actual geological features (reservoir geometry, fault and hydrate water contact), simulations were first conducted to quantify the uncertainties associated with predictions from this model based on production from vertical and inclined wells, respectively. Uncertainties in predictions based on this model were only about 1.7 % and 0.5 % of the mean values $5.33\pm0.09 \times 10^8$ ST m^3 (18.82 ± 0.32 BSCF) and $6.07\pm0.03 \times 10^8$ ST m^3 (21.44 ± 0.11 BSCF)) for the vertical and inclined wells, correspondingly. The results are an indication of the reliability of the data driven model and provides an indication that the amount of well log data used for the study is sufficient to adequately characterize the reservoir.

Sensitivity of reservoir performance to well design showed that the maximum overall recovery achievable were in the range 30 – 40 % of the original GIP in form of hydrates, with the well configuration having two lateral sections each penetrating the D and C sands having the highest recovery. This indicates a need for the application of a more advanced recovery technique to enhance reservoir performance within a typical life span of a producing well. Large amounts of liquid phase produced ($2.74 – 3.61 \times 10^6$ ST m^3 or $1.72 – 2.27 \times 10^7$ bbl)) suggest a need for the provision for downhole gas-water separation in the wellbore design in order to reduce the load on the production lift system. Study also showed that the presence of

hydrate-water contact did not have any significant impact on the cumulative gas volume produced at the end of 30 years. However, a model with water contact produced 90 % more volume of water compared with that without water contact. From a water production management perspective, this result may have substantiated a basis for the consideration of a production method which would involve an initial injection of CO_2 into the free-water zone just below the hydrate-water contact to form CO_2 hydrates, which would now be followed by the production phase using the depressurization technique.

Using a generalized 3D rectangular geometry, sensitivity analysis was conducted to explore effects of reservoir dimensionality, heterogeneity of porosity, hydrate saturation, and intrinsic permeability on production potential. A simplified 2D geometry for a hydrate reservoir model and assumption of vertical heterogeneity in porosity and hydrate saturation led to underestimation of reservoir productivity by about 38 % in comparison with the model employed in this study. Modeling gas production from the hydrate sand units using uniform intrinsic permeability (734 mD in the horizontal and 367 mD in the vertical direction) overestimates the cumulative gas volume produced at the vertical well by around 40 % comparing with the heterogeneous permeability representation.

Secondary hydrate formation around a well bore predicted in previous simulations utilizing 2D geometry and homogeneous or vertical heterogeneous porosity and hydrate saturation distributions severely hinders gas production. In this study, the secondary hydrate formation was confirmed away from a producing well as short-lived patches of increased or sustained hydrate saturations. The reason of their appearance was attributed to local pressure fluctuations caused by temporal gas trapping during mobile phase flow in complex 3D porous network containing dissociating hydrate. This is another evidence of the profound importance

of a 3D heterogeneous representation of a reservoir system which captures details of actual geological settings.

Based on the current predictions of water production, flow assurance studies show that very large volumes of methanol (> 308 m^3 /day or 1938 bbl/day) need to be injected into the wellbore in order to inhibit the secondary formation of hydrates in the wellbore , making it impractical. These numbers, again emphasize the need for the provision of a downhole water-gas separation during production to reduce the pumping load and methanol injection, if necessary. In the consideration of a possible alternative, calculations show that minimum DEH requirements are 8.73, 68.05 and 67.83 W/m heating power per unit length of wellbore, corresponding to the 30, 50 and 100 kW pump power outputs, which translates to a requirement that the wellbore wall temperature (T_w) should be maintained at 8, 25 and 25 ^{0}C, when using a pump with power outputs of 30, 50 and 100 kW, respectively. These results suggest that DEH might be a more suitable alternative than methanol injection, in the absence of downhole water-gas separation.

The economic viability of different options of long-term field development were evaluated using a generalized 3D rectangular geometry. Among the four scenarios considered, the most promising field development option is the use of four inclined wells (4I08), however, all of the options remain economically unattractive with NPVs in the range -$ 21.3 – -$ 13.8 million. Therefore, an aggressive enhanced recovery method may be required to improve on the economic viability of long term production from this particular site.

The productivity of a probable hydrate deposit downdip and to the east of the L-Pad was also studied for reservoirs with depths 50 and 100 m, respectively. The maximum gas rates achieved were 1.1 and 2.4 times more than the maximum production rate achieved from the

original L-pad, respectively for the 50 and 100 m-depth models. Cumulative volumes achieved at the end of 30 yr (Figure 3-35), are 45 and 76 % more than the reference case for the 50 and 100 m-downdip models respectively. At 30 yr, NPVs are $ 0.28 and $ 21.69 million, and breakeven gas wellhead prices are $ 5.27 and $ 3.58 per MSCF for reservoir depths 50 and 100 m, respectively. These show that the L-Pad downdip would be a much more favorable production site than the L-Pad, however, geological risks associated with the site make predictions less reliable.

References

1. Hunter, R.B., Digert, S.A., Boswell, R., and Collett, T.S., *Alaska gas hydrate research and stratigraphic test preliminary results*, in *The Arctic Energy Summit*. 2007: Anchorage, Alaska.

2. Collett, T.S., Boswell, R., Lee, M.W., Anderson, B.J., Rose, K., and Lewis, K.A., *Evaluation of long-term gas-hydrate-production testing locations on the alaska north slope.* SPE Reservoir Evaluation & Engineering, 2012. **15**(02): p. 243-264.

3. Collett, T.S., *Natural gas hydrates of the prudhoe bay and kuparuk river area, north slope, alaska.* AAPG bulletin, 1993. **77**(5): p. 793-812.

4. Anderson, B.J., Wilder, J.W., Kurihara, M., White, M.D., Moridis, G.J., Wilson, S.J., Pooladi-Darvish, M., Masuda, Y., Collett, T.S., and Hunter, R. *Analysis of modular dynamic formation test results from the mount elbert 01 stratigraphic test well, milne point unit, north slope, alaska*. in *6th International Conference on Gas Hydrates (ICGH 2008)*. 2008. Vancouver, British Columbia, Canada.

5. Anderson, B.J., Kurihara, M., White, M.D., Moridis, G.J., Wilson, S.J., Pooladi-Darvish, M., Gaddipati, M., Masuda, Y., Collett, T.S., and Hunter, R.B., *Regional long-term production modeling from a single well test, mount elbert gas hydrate stratigraphic test well, alaska north slope.* Marine and petroleum geology, 2011. **28**(2): p. 493-501.

6. Myshakin, E.M., Anderson, B.J., Rose, K., and Boswell, R., *Simulations of variable bottomhole pressure regimes to improve production from the double-unit mount elbert, milne point unit, north slope alaska hydrate deposit.* Energy & Fuels, 2011. **25**(3): p. 1077-1091.

7. Kurihara, M., Funatsu, K., Ouchi, H., Masuda, Y., Yasuda, M., Yamamoto, K., Numasawa, M., Fujii, T., Narita, H., and Dallimore, S.R., eds. *Analysis of the jogmec/nrcan/aurora mallik gas hydrate production test through numerical simulation*. Scientific results from the mallik 2002 gas hydrate production research well program, mackenzie delta, northwest territories, canada, ed. S.R. Dallimore and T.S. Collett. Vol. 585. 2008, Geological Survey of Canada, Bulletin.

8. Kurihara, M., Sato, A., Ouchi, H., Narita, H., Ebinuma, T., Suzuki, K., Masuda, Y., Saeki, T., Yamamoto, K., and Fujii, T. *Prediction of production test performances in eastern nankai trough methane hydrate reservoirs using 3d reservoir model*. in *Offshore Technology Conference, Houston, Tex*. 2010.

9. Reagan, M., Moridis, G.J., and Zhang, K., *Sensitivity analysis of gas production from class 2 and class 3 hydrate deposits*, in *2008 Offshore Technology Conference*. 2008: Houston, Texas, USA.

10. Reagan, M.T., *The effect of reservoir heterogeneity on gas production from hydrate accumulations in the permafrost.* Lawrence Berkeley National Laboratory, 2010.

11. Moridis, G.J., Kowalsky, M.B., and Pruess, K., *Depressurization-induced gas production from class-1 hydrate deposits.* SPE Reservoir Evaluation & Engineering, 2007. **10**(05): p. 458-481.

12. Moridis, G. and Reagan, T., *Strategies for gas production from oceanic class 3 hydrate accumulations, paper otc 18865 presented at the offshore technology conference.* Am. Assoc. of Pet. Geol., Houston, Tex, 2007. **30**.

13. Gaddipati, M., *Reservoirs modeling of gas hydrate deposits in north slope of alaska and gulf of mexico*. 2014, West Virginia University: Ann Arbor. p. 136.

14. Gaddipati, M. and Anderson, B.J., *3d reservoir modeling of depressurization-induced gas production from gas hydrate reservoirs at the walker ridge site northern gulf of mexico*, in *Offshore Technology Conference*. 2012.

15. Myshakin, E.M., Gaddipati, M., Rose, K., and Anderson, B.J., *Numerical simulations of depressurization-induced gas production from gas hydrate reservoirs at the walker ridge 313 site, northern gulf of mexico.* Marine and Petroleum Geology, 2012. **34**(1): p. 169-185.

16. Reagan, M.T., Moridis, G.J., Johnson, J.N., Pan, L., Freeman, C.M., Boyle, K.L., Keen, N.D., and Husebo, J., *Field-scale simulation of production from oceanic gas hydrate deposits.* Transport in Porous Media, 2014. **108**(1): p. 151-169.

17. Anderson, B., Boswell, R., Collett, T., Farrell, H., Ohtsuka, S., and White, M.D., *Review of the findings of the iġnik sikumi co2-ch4 gas hydrate exchange field trial*. 2014, Pacific Northwest National Laboratory (PNNL), Richland, WA (US).

18. Archie, G.E., *The electrical resistivity log as an aid in determining some reservoir characteristics.* 1942.

19. Bigelow, E., *Introduction to wireline log analysis: Western atlas international.* Inc., Houston, Texas, 1992.

20. Crain, E.R. *Crain's petrophysical handbook*. Porosity from density log model 2015 [cited 2015.

21. Koltermann, C.E. and Gorelick, S.M., *Fractional packing model for hydraulic conductivity.* Water Resources Research, 1995. **31**(12): p. 3283-3297.

22. Marion, D., Nur, A., Yin, H., and Han, D.-H., *Compressional velocity and porosity in sand-clay mixtures.* Geophysics, 1992. **57**(4): p. 554-563.

23. Wilder, J.W., Moridis, G.J., Wilson, S.J., Kurihara, M., White, M.D., Masuda, Y., Anderson, B.J., Collett, T.S., Hunter, R.B., and Narita, H., *An international effort to*

compare gas hydrate reservoir simulators, in *Proceedings of the 6th International Conference on Gas Hydrates (ICGH 2008)*. 2008: Vancouver, CANADA.

24. Gaddipati, M., *Code comparison of methane hydrate reservoir simulators using cmg stars*. 2008: West Virginia University.

25. Clayton, V. and Journel, A.G., *Gslib-geostatistical software library and user's guide.* Technometrics, 1998.

26. Anderson, B., Hancock, S., Wilson, S., Enger, C., Collett, T., Boswell, R., and Hunter, R., *Formation pressure testing at the mount elbert gas hydrate stratigraphic test well, alaska north slope: Operational summary, history matching, and interpretations.* Marine and Petroleum Geology, 2011. **28**(2): p. 478-492.

27. van Genuchten, M.T., *A closed-form equation for predicting the hydraulic conductivity of unsaturated soils.* Soil science society of America journal, 1980. **44**(5): p. 892-898.

28. Stone, H.L., *Probability model for estimating three-phase relative permeability.* Journal of Petroleum Technology, 1970. **22**(02): p. 214-218.

29. Wright, J., Dallimore, S., and Nixon, F., *Influences of grain size and salinity on pressure-temperature thresholds for methane hydrate stability in japex/jnoc/gsc mallik 2l-38 gas hydrate research-well sediments.* BULLETIN-GEOLOGICAL SURVEY OF CANADA, 1999: p. 229-240.

30. Burt, J., Hupp, D., Elfouly, M., Heath, R., and Wu, J., *Ignik sikumi #1 interpretation report*. 2011, Schlumberger.

31. CMG, *Advanced processes & thermal reservoir simulator (stars) user's guide*. 2014, Calgary, Alberta Canada: Computer Modelling Group Ltd.

32. Ajayi, T.A., Anderson, B., Seol, Y., and Myshakin, E., *Numerical simulations of depressurization-induced gas production from the 3d heterogeneous l-pad, prudhoe bay unit, alaska north slope hydrate reservoir model.* Journal of Natural Gas Science and Engineering (to be submitted), 2016.

33. Moridis, G.J., Reagan, M.T., Anderson-Kuzma, H., Zhao, Y., Boyle, K., and Rector, J.W. *Evaluation of the hydrate deposit at the pbu l-106 site, north slope, alaska, for a long-term test of gas production*. in *OTC Arctic Technology Conference*. 2011. Offshore Technology Conference.

34. Li, X.-S., Li, B., Li, G., and Yang, B., *Numerical simulation of gas production potential from permafrost hydrate deposits by huff and puff method in a single horizontal well in qilian mountain, qinghai province.* Energy, 2012. **40**(1): p. 59-75.

35. Li, X.-S., Yang, B., Li, G., and Li, B., *Numerical simulation of gas production from natural gas hydrate using a single horizontal well by depressurization in qilian*

mountain permafrost. Industrial & Engineering Chemistry Research, 2012. **51**(11): p. 4424-4432.

36. Seol, Y. and Myshakin, E., *Experimental and numerical observations of hydrate reformation during depressurization in a core-scale reactor.* Energy & Fuels, 2011. **25**(3): p. 1099-1110.

37. Schoderbek, D., Martin, K.L., Howard, J., Silpngarmlert, S., and Hester, K. *North slope hydrate fieldtrial: Co2/ch4 exchange*. in *OTC Arctic Technology Conference*. 2012. Offshore Technology Conference.

38. Hammerschmidt, E., *Preventing and removing gas hydrate formations in natural gas pipe lines.* Oil Gas J., 1939. **37**: p. 66.

39. Barlow, W. and Bewald, W. *Optimum oil-well spacing*. in *Drilling and Production Practice*. 1945. New York, New York: American Petroleum Institute.

40. Craze, R.C. and Buckley, S.E., *A factual analysis of the effect of well spacing on oil recovery*, in *Drilling and Production Practice*. 1945, American Petroleum Institute: New York, New York.

41. MacRoberts, D.T., *Relation of gas-well spacing to ultimate recovery.* Trans. AIME, 1938. **127**(01): p. 146 - 158.

42. Muskat, M., *Principles of well spacing.* Trans. AIME, 1940. **136**(01): p. 37 - 56.

43. Vietti, W.V., Thornton, O.F., Mullane, J.J., and Van Everdingen, A.F., *The relation between well spacing and recovery*, in *Drilling and Production Practice*. 1945, American Petroleum Institute: New York, New York.

44. Administration, U.S.E.I. *Independent statistics and analysis: Natural gas*. 2008; Available from: https://www.eia.gov/dnav/ng/hist/n9190us3a.htm.

45. Institute, A.P., *Joint association survey on drilling costs*. 1976-2012.

46. Nyayapathi, L., *Performance and economics of methane hydrate reservoirs*. 2010: West Virginia University.

4. Mount Elbert-Like Models

4.1 Introduction

In February 2007, the US Department of Energy (DOE), BP Exploration Alaska (BPXA) and the USGS embarked on a study which was primarily aimed at confirming the nature of reservoir occurrence and collecting reservoir data in order to support reservoir simulation modeling and long-term production test design. This led to the *Mount Elbert Gas Hydrate Stratigraphic Test* drilling program. The Mount Elbert (or Mt. Elbert) prospect is located in the Milne Point Unit (MPU) of the Alaska North Slope (Figure 4-1). Its hydrate accumulations have been identified as part of the Eileen Trend[1]. Assessment have shown that the Mt. Elbert prospect is the highest-ranked MPU gas hydrate prospect[2]. Further evaluation by Inks et al.[3] also predicted the gas-in-place volumes of the Mt. Elbert prospect to be ~ 4.1 x 10^9 ST m^3 (~ 145 BSCF), which are trapped in two sand units (C and D) and located in stratigraphically highest portions of those sands. A series of formation pressure (drawdown and buildup) tests was conducted at various depth intervals to obtain a measure of the effective permeability of the reservoir. Results of the formation pressure tests and history matching efforts are detailed in the works by Anderson et al.[4], Kurihara et al.[5] and Pooladi-Darvish and Hong[6].

The Mt. Elbert hydrate prospect has been evaluated as a candidate for long-term production tests by Collett et al.[7]. The assessment shows that the site has minimal risks associated with ownership structure and interference with existing conventional oilfield production operations, when compared with the L-Pad prospect.

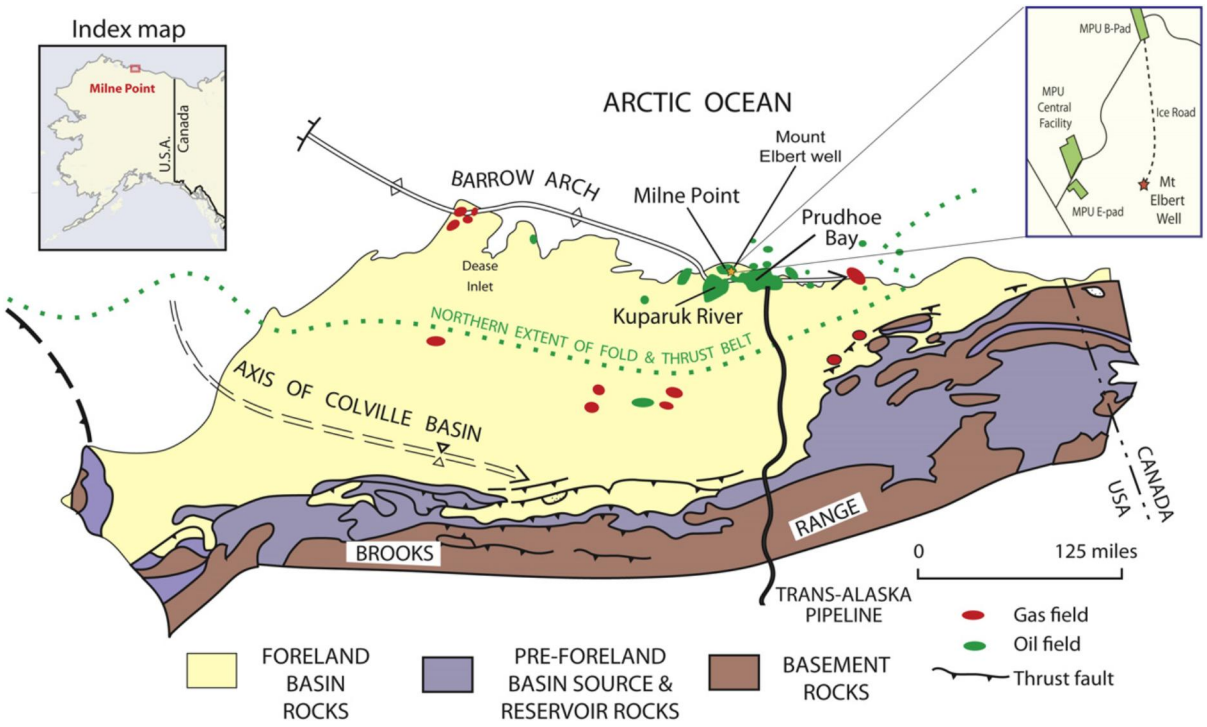

Figure 4-1: The location of the Mount Elbert well within the Milne Point Unit (MPU) on the North Slope of Alaska. Inset shows the position of the nearest offset wells on the MPU E and MPU B production pads.

4.2 Model Objectives

The goal of the models discussed in this chapter is to evaluate alternative production sites with deeper hydrate accumulations and minimal geological risks within the MPU. The hydrate-bearing D sand of the MPU, being close to the permafrost with temperatures ranging between 2.3 – 2.6 ^{0}C[8], are too cold for production. The hydrate-bearing C sand is at least 1 ^{0}C warmer than the D sand, which makes it a better production target than the D sand, however, previous studies[7, 9, 10] have also shown that temperatures of the C sand hydrates are not adequately warm enough for viable production. In the light of the foregoing, production potential from 3D reservoir models of the hydrate-bearing C sand of the Mt. Elbert-like "Site 2" models will be assessed with the aim of obtaining predictions from deeper hydrate accumulations having geological and petro-physical features similar to the Mt. Elbert region. Furthermore, as an improvement to existing models, the model developed in this study would also incorporate as much as possible the structural and geophysical heterogeneities of the reservoir by maximizing the utilization of the available field data. Using the Mt. Elbert model as a reference case, sensitivity of predictions of gas rates and cumulative volumes to reservoir depths (hence temperature) will be determined. The study would also obtain a qualitative measure of the sensitivity of predictions to uncertainties in the approximation of reservoir quality (hydrate saturation, porosity, intrinsic permeability and irreducible water saturation).

4.3 Previous Modeling Efforts

Studies on gas production from the Mt. Elbert hydrate prospect have been mostly based on homogeneous models or models with incorporation of vertical heterogeneity. Problem 7a of the International Code Comparison[11, 12] is a model with homogeneous approximations of reservoir properties which describes production from the hydrate-bearing C unit of a Mt.

Elbert-like site. Moridis[8] investigated production from the Mt. Elbert D unit-hydrate with the assumption of homogeneous distribution of properties and the absence of water contact at the base of the hydrate (a Class 3 reservoir). However, the works of Anderson[9] and Myshakin et al.[10] introduced vertical heterogeneities in the distribution of porosity, permeability, hydrate saturation and irreducible water saturation. While Anderson's model described production only from the C sand hydrates, Myshakin et al. modeled production from the hydrates of both the D and C units with variable bottom-hole pressures. All these reservoir models are based on a 2D cylindrical geometry. There is no known model (at least to the author) of the Mt. Elbert prospect which incorporates a full 3D heterogeneous distribution of properties and the actual reservoir geometry. The importance of the incorporating the heterogeneities in reservoir models have been extensively discussed in the previous chapter (Section 3.6.5) and, therefore, will not be repeated in this chapter. Overall, predictions from all of these models showed consistency in terms of low gas production rates and cumulative volumes achieved from the cold reservoir.

4.4 Reservoir Characterization and Model Development

In 2003, the USGS embarked on a study to develop seismic interpretive methods to characterize gas hydrate accumulations in the MPU. Detailed analysis and interpretation of 3D seismic data led to the identification of the extent of hydrate accumulations in the Mt. Elbert region[3, 13]. The seismic-inferred reservoir depths to the top of the C sand shows that the Mt. Elbert well is drilled in the region of highest stratigraphy.

Well log data (Figure 4-2[14]) and retrieved core sections show that the entire C unit at the Mount Elbert location is comprised of two primary lithologic units.[15] The formation within depth interval 650 – 663 m (2133 – 2176 ft) represents the upper portion of the C unit sand

with hydrates (C-GH1 in Figure 4-2) filling that section from 650 – 661 m (2133 – 2168.0 ft) while the remaining part is highly saturated with water[10, 11], which essentially makes this upper section a Class 2 reservoir[14, 16]. The upper portion of the C sand is characterized by a succession of thin, fining upwards sequences of very-fine sand, silt, fine silt and clay layers.[16] The lower section, found in the interval 663 – 729 m (2176 – 2391 ft) makes up the most part, with hydrates (C-GH2 in Figure 4-2) filling only the depth interval 663 – 666 m (2176 – 2185 ft), leaving an underlying thick section of high-reservoir quality sands with no gas hydrate present. The bottom C unit characterized with by a thick sequence of fine to very-fine sands with rare shale inter-beds and exhibits an overall upward increase in reservoir quality[16]. The entire C unit is overburdened by a low permeable high-clay content section.

In the models developed in this study, the following data provided by the USGS were processed to describe the nature of hydrate occurrences within the Mt. Elbert vicinity:

- Seismic-interpreted depth to top of C sand unit (Figure 4-3 (a))
- Seismic-interpreted 2D map of hydrate saturation in the C unit (Figure 4-3 (b))
- Density log-derived porosity, NMR log-derived hydrate saturation and irreducible water saturation data obtained from the Mt. Elbert well

Figure 4-5 shows that the Mt Elbert well was drilled at a high stratigraphic point in the region of high hydrate saturation. The Milne Point 3-D seismic gas hydrate prospecting effort also revealed the lateral nature of the well log inferred gas hydrate-bearing sedimentary units.

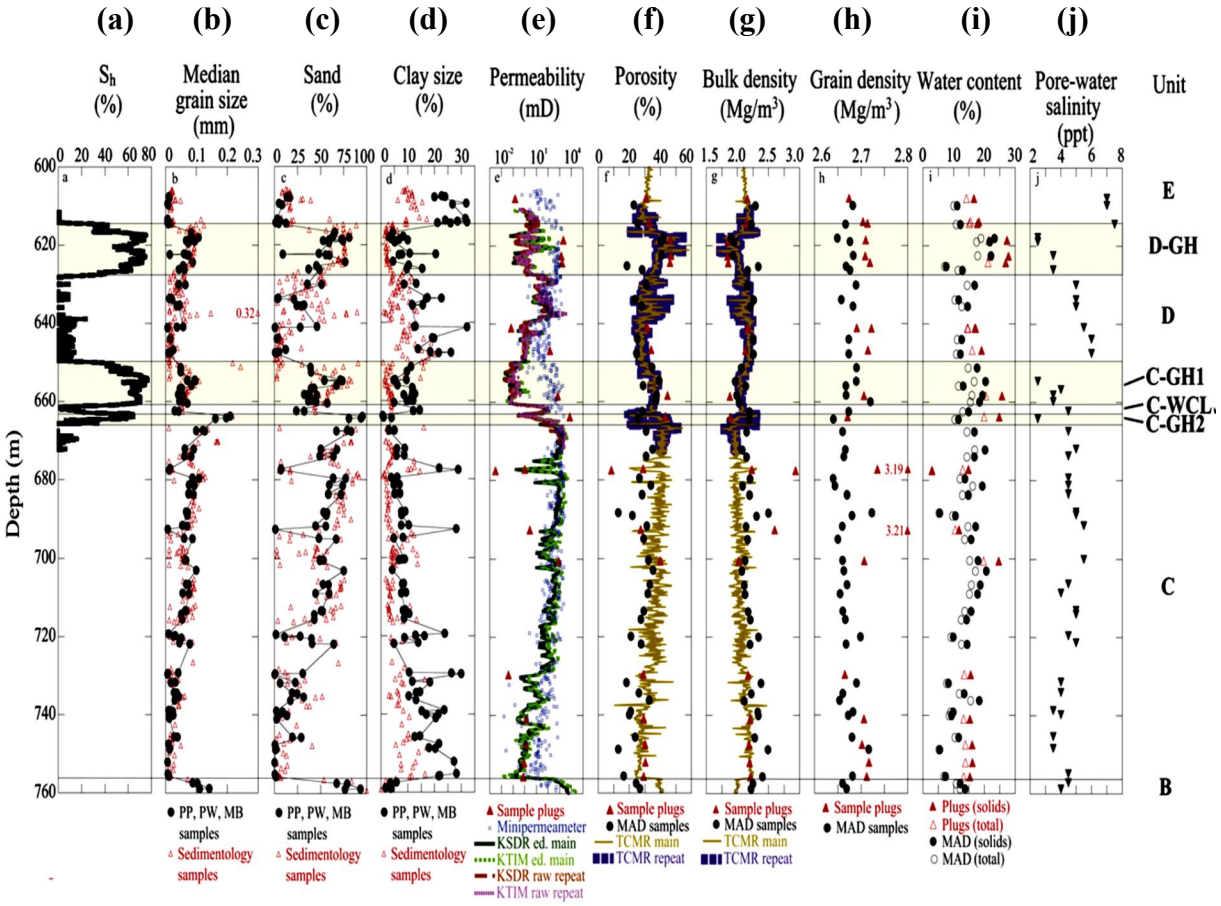

Figure 4-2: Mt. Elbert Well log profiles of sediment properties including: (a) NMR+density porosity-derived hydrate saturation (S_h)[17], (b), (c), and (d) median grain size, percent sand, and percent clay-size determined from laser-grain-size analyses on physical property (PP), pore water (PW), microbiology (MB), and sedimentology samples[15], (e) permeability measurements from core plugs, slabbed core using a mini-permeameter, and well logs[16], (f) moisture and density (MAD) + combinable magnetic resonance (CMR)-derived porosity (g) MAD+CMR-derived bulk density[16] (h) MAD-derived grain density[16], (i) water content[16], and (j) pore water salinity[18]

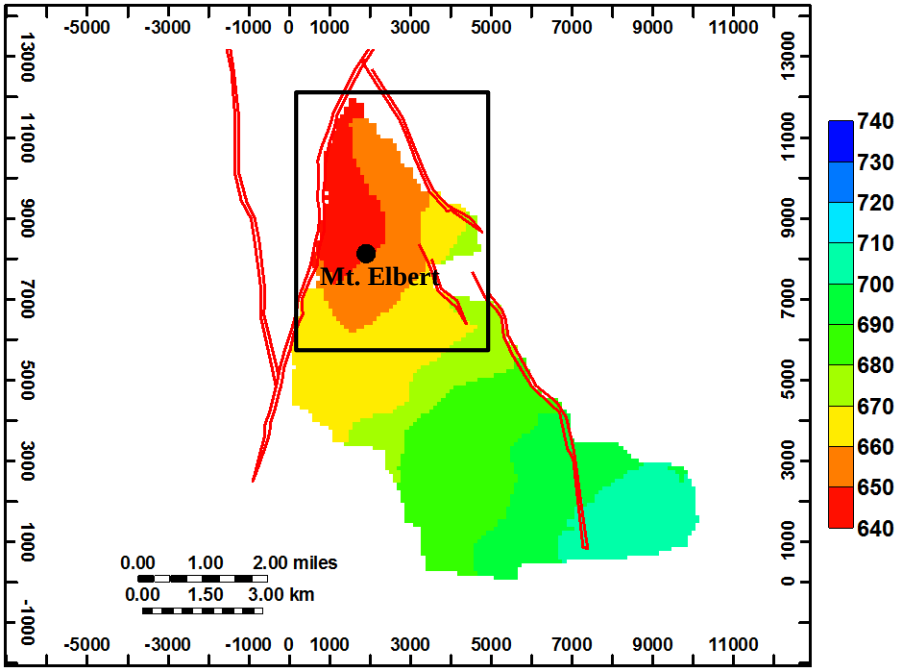

(a)

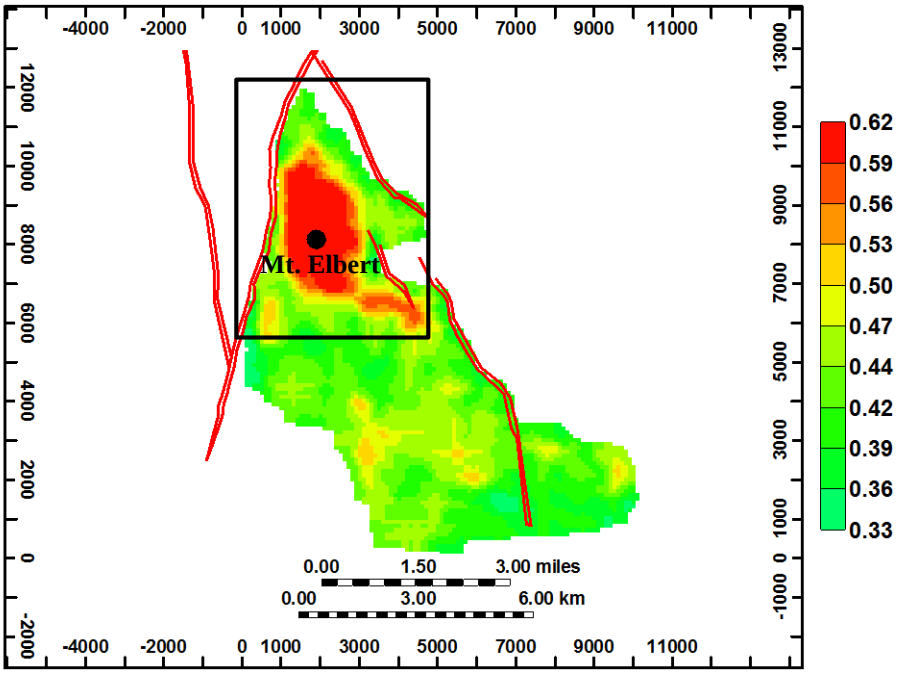

(b)

Figure 4-3: a) Structure contour maps of depth to top of C sand with color bar representing true vertical depth from sea level, and b) 2D S_h map in the C sand with color bar representing hydrate saturation, showing faults (red lines), Mt. Elbert well location and model area (black line-bounded box, 5 km x 6 km)

A summary of the geometry and discretization of the flow simulation model shown in Figure 4-4 is presented in Table 4-1. The vertical grid divisions is based on the heterogeneous model of Problem 7a[9]. It has a total of 50 hydrate layers with each layer being 0.25 m-thick. It also has 50 m-thick (each) low-permeable overburden and underburden shale formation which provide constant temperature-boundary conditions at the top and bottom of the hydrate-bearing sand, respectively. The bounding faults are assumed to be sealing and non-conducting, therefore, there is no flow to mass or heat at the north, east and west boundaries. Owing to the huge computational demand by the size of the original domain of the Mt. Elbert, a southern boundary of the modeled area (black box in Figure 4-3) was defined (based on preliminary simulations) with a prediction that the hydrate dissociation front will not hit the southern boundary within the simulated production time of 30 yr. This also implies no flow to heat or mass across the southern boundary. As shown by the inset figure of Figure 4-4 (a), the original size (100 m x 100 m) of the grid blocks in the horizontal plane was refined to the smaller grid blocks (0.6 m x 0.6 m) around the wellbore to improve accuracy of numerical computation. The size of the refined grid block at the wellbore is such that their effective radii is at least 10 % larger than the wellbore radius of 0.11 m to ensure numerical convergence[19].

Characterization of the reservoir proceeded with estimating a 3D distribution of hydrate saturation in the C unit. The vertical hydrate saturation (S_h) profile (from well log) and surface hydrate saturation distribution (from seismic) were combined to give a first order estimate of the 3D hydrate distribution in the reservoir volume. The high resolution vertical profiles of the properties obtained from the well log (at every 0.5 ft or 0.15 m) has been coarsened to fit the model discretization in the vertical direction within depth range of the C sand thickness[9].

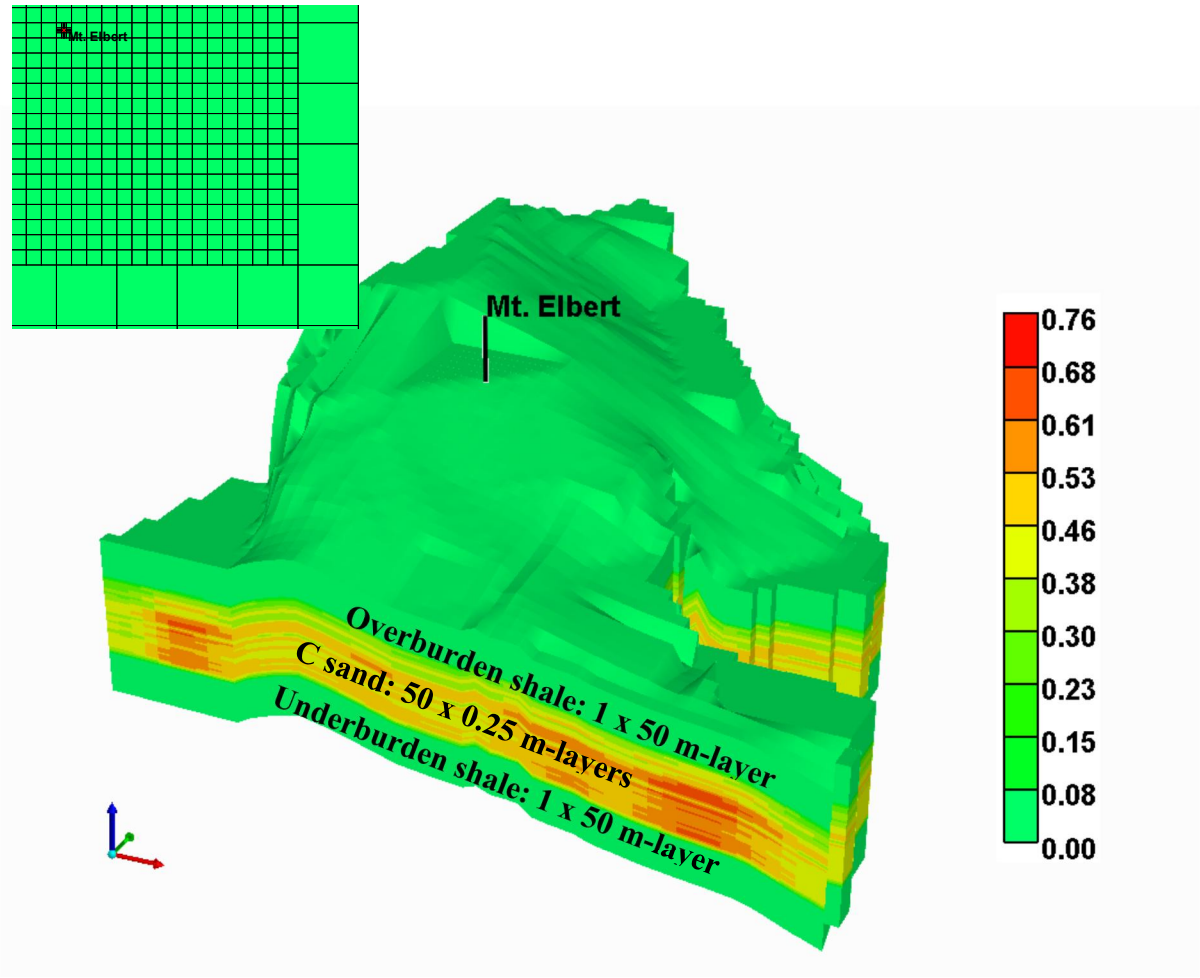

Figure 4-4: 3D geometry of flow simulation model showing Sh distribution (color bar). Inset figure shows the horizontal grid refinement within the vicinity of the wellbore.

Table 4-1: Model geometry details

Formation	Top (m)	Thickness (m)	Layer Range (Number of Layers)	Simulation Layer Thickness (m)
Shale	638 – 670	5 (x 10)*	1 (1)	50*
C Sand	643 – 675	12.5	2 – 51 (50)	0.25
Shale	655 – 687	5 (x 10)*	52 (1)	50*

*Grid thickness was multiplied by a volume modifying factor of 10, so that effective simulation layer thickness = 50 m

The vertical S_h profile obtained from the log ($S_{h,\,log}$) was normalized by dividing each of the S_h log values by the maximum value from the 2D surface S_h distribution ($S_{h,\,2D\_max}$). The normalized profile was used as a multiplication factor by which the original surface hydrate saturation distribution ($S_{h,\,2D}$) was multiplied to give an estimate of the surface hydrate saturation distribution in each layer. These steps are illustrated in Figure 4-5.

Porosity (ϕ) and irreducible water saturation distributions (S_{wir}) were estimated by establishing a correlation between their log-derived vertical profiles and that of S_h. The development of these correlations are shown in Figure 4-6 and the relationships are given by Equations (4-1) and (4-2)

$$\phi = 0.20\,S_h + 0.22 \tag{4-1}$$

$$S_{wir} = -0.88\,S_h + 0.84 \tag{4-2}$$

Intrinsic "hydrate-free" permeability was calculated from the correlation developed by Myshakin et al[10], as previously given by Equation (3-4).

4.5 Reservoir Model Parameters and Initial Conditions

A summary of the reservoir properties and initial conditions are given in Table 4-2. As a result of the variation in the 3D distribution of S_{wir} and the dependency of relative permeability on S_{wir}, each grid block in the model has a unique relative permeability model associated with it. The nature of the initial distributions of S_h and S_{wir} ensured that the initial free water saturation in reservoir was not more than 16 % of the total pore space. The pressure in the sediment subsurface was assumed to follow a hydrostatic pore pressure distribution and thermal distribution was based on a geothermal gradient of 0.038 °C/m, derived from the MPU D-02 well temperature log.[20]

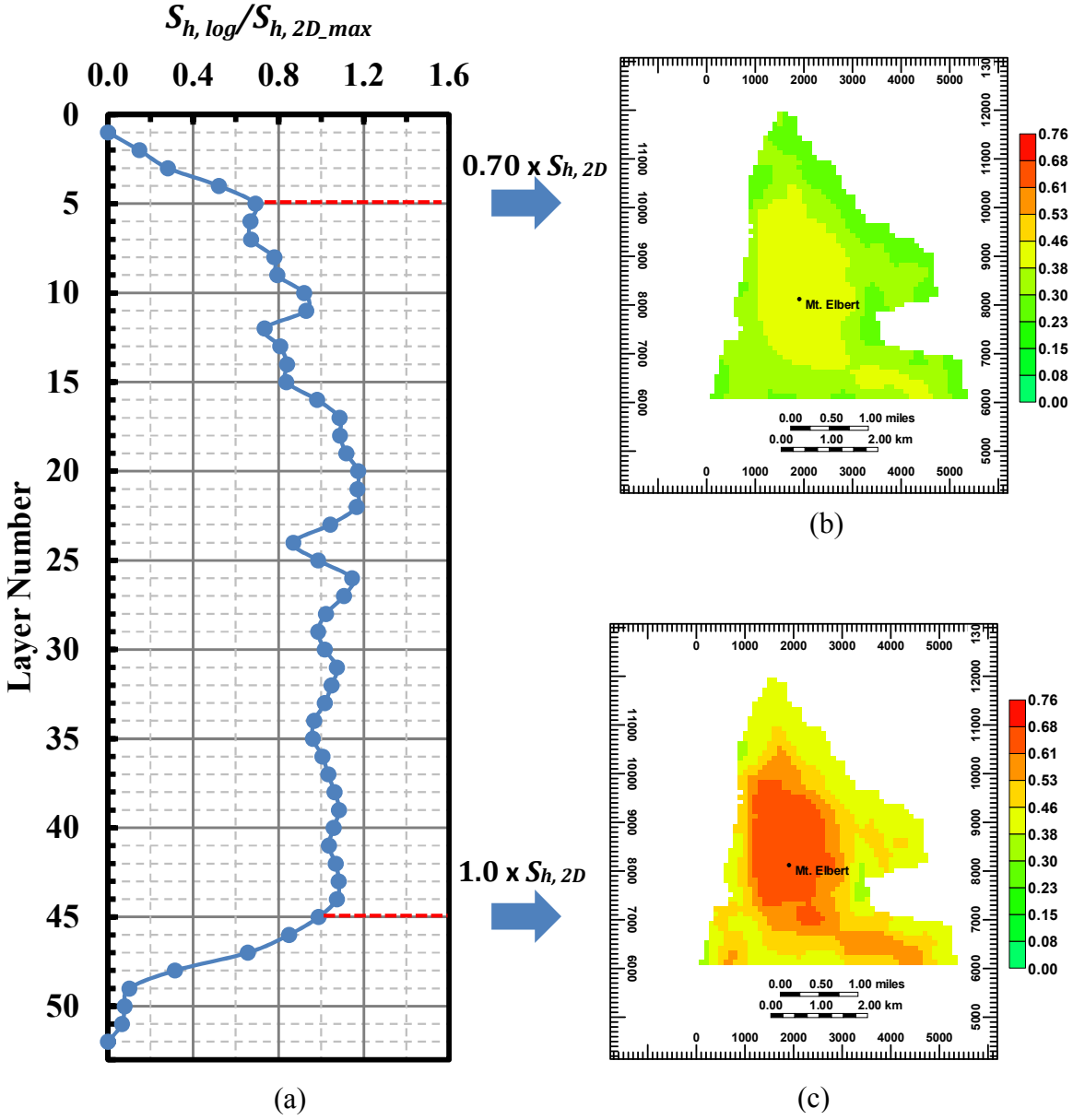

Figure 4-5: Well log and seismic-inferred (a) normalized vertical S_h distribution within the C sand interval, (b) Surface 2D S_h distribution in the 5th layer, and (c) surface 2D S_h distribution in the 40th layer

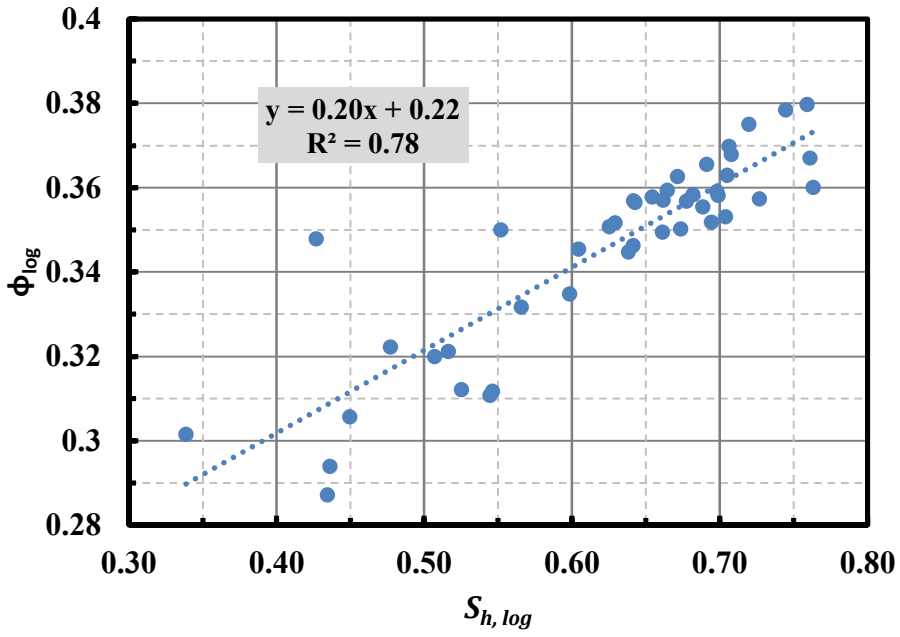

(a)

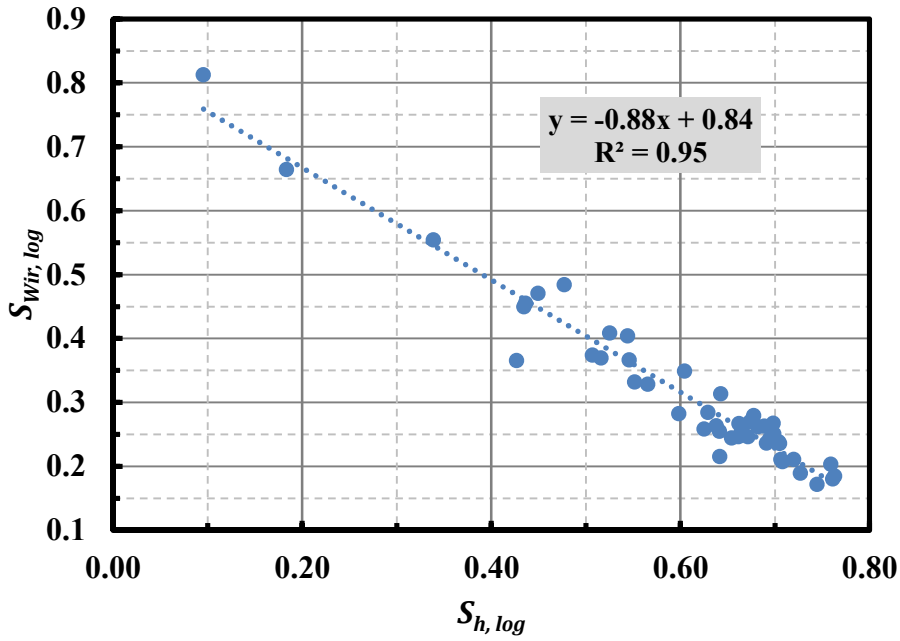

(b)

Figure 4-6: Correlation between well log-derived hydrate saturation ($S_{h,log}$) and (a) well log-derived-porosity (ϕ_{log}), and (b) well log-derived irreducible water saturation ($S_{wir,log}$)

Table 4-2: Reservoir properties, initial conditions, and pertinent model parameters.

Parameter	Value
Porosity of sand units, ϕ	0.23 – 0.37
Initial hydrate saturation	0.03 – 0.76
Intrinsic permeability of sand units, k_{sand}, *mD*	102 – 562, horizontal and 51 – 281, vertical permeability (0.5 anisotropic factor)
Intrinsic permeability of the shale layers, k_{shl}, *mD*	0.001, horizontal and 0.0005, vertical
Porosity of shale layers, ϕ	0.22, from Equation (4-1) with $S_h = 0$
Pore compressibility, α_p, Pa^{-1}	$5 \cdot 10^{-10}$
Thermal conductivity of hydrate-bearing sand, k_{sand}, *W/m K*	2
Thermal conductivity of shale, k_{sand}, *W/m K*	2
Capillary pressure model[21]	$P_{cap} = -P\left[(S^*)^{-1/\lambda} - 1\right]^{1-\lambda}$ $S^* = \frac{(S_w - S_{wcap})}{(S_{w,\max} - S_{wcap})}$
Capillary-bound water, S_{wcap}	0.10 (see note below)
λ[9, 12]	0.77437
$S_{w,max}$	1
P_{max}, *Pa*	10^4
Pore water salinity, *ppt*	5
Relative permeability Modified Stone 3-phase model[22]	$k_{rw} = (S_w^*)^{nw}$; $k_{rw} = (S_G^*)^{nG}$ $S_w^* = \frac{(S_w - S_{wir})}{(1 - S_{wir})}$; $S_G^* = \frac{(S_G - S_{Gir})}{(1 - S_{Gir})}$
n[9, 23]	$n_w = 5.04$; $n_G = 3.16$
Irreducible gas saturation, S_{Gir}	0
Irreducible (total bound) water saturation, S_{wir}	0.20 – 0.82, from Equation (4-2)
Rock density, kg/m^3	2650

Note: S_{wcap} = ~ 50 % (arbitrarily set) of the minimum value of the irreducible (total bound) water saturation distribution (S_{wir}) with the balance ($S_{wir} - S_{wcap}$) assumed to be clay-bound. A sensitivity study on this property is discussed in Section 4.6.2.

This resulted in average pressure and temperature of 7.13 MPa and 3.67 °C, respectively, in the C sand. For the layers of the reservoir model, the initialization of P/T conditions (pressure and temperature gradients throughout the vertical dimension of the domain) were carried out to achieve hydraulic, thermal, thermodynamic, and chemical equilibrium and ensure correct pressure and temperature conditions of the layers relative to the base of gas hydrate stability. Production by depressurization using the Mt. Elbert well was simulated with CMG STARS for a 30 year-period, with a minimum well flowing bottom-hole pressure (BHP) of 2.8 MPa.

4.6 Flow Simulation Results and Discussions

Previous simulations have shown that the Mt. Elbert hydrate prospect may be too cold to be economically viable. Therefore, a sensitivity study was carried with respect to reservoir depth to simulate scenarios where hydrates deposits (hereby named "Site 2") similar to Mt Elbert may exist in deeper sediments. This analysis is followed by an uncertainty assessment to determine the range of production potential with respect to uncertainties in the distribution of hydrate saturation coupled with porosity, intrinsic permeability and irreducible water saturation.

4.6.1 Sensitivity to depth

Using the original Mt. Elbert model described in the previous section as a reference case, additional four "Site 2" models were developed, with reservoir depths to the top of the C sand (at the Mt Elbert well) of 700, 750, 800 and 850 m. It is to be noted that the base of hydrate stability is at ~ 900 m in the MPU. More details about the range of reservoir depths, temperatures and pressures are given in Table 4-3.

Table 4-3: Reservoir depths, temperature and pressure in Mt. Elbert and Site 2 models

Model	Depth to C sand (m)	Temperature (^{0}C)	Pressure (kPa)
Mt. Elbert (reference)	638 – 670	3.03 – 4.67	6936 – 7404
Site 2 @ 700	688 – 720	4.91 – 6.53	7475 – 7943
Site 2 @ 750	738 – 770	6.78 – 8.41	8015 – 8483
Site 2 @ 800	788 – 820	8.66 – 10.28	8554 – 9022
Site 2 @ 850	838 – 888	10.53 – 12.16	9094 – 9562

Figure 4-7 shows the gas production rates and cumulative volumes for all cases including the reference model. Very low production rate and cumulative volumes are obtained in the Mt. Elbert over the 30 year-period and this further substantiates earlier predictions of the productivity of the region. Gas rates increase with increase in reservoir depth, with the highest gas rate being 4.08 x 10^5 ST m^3/day (14.4 MMSCF/day), as predicted by the *Site 2 @ 850* model. The highest cumulative gas volume produced at the end of 30 years is 2.66 x 10^9 ST m^3 (~ 94 BSCF). Based on the cost data of Table 3-12, evaluation of NPVs at the end of 30 yr (Figure 4-8) show that only the *Site 2 @ 800* and *Site 2 @ 850* models would have positive net cash inflow at the end of 30 yr with breakeven wellhead gas prices of $ 3.57 and $ 2.06 per MSCF. A Site 2 hydrate prospect that will breakeven exactly at 30 yr would have a reservoir depth between 750 – 800 m.

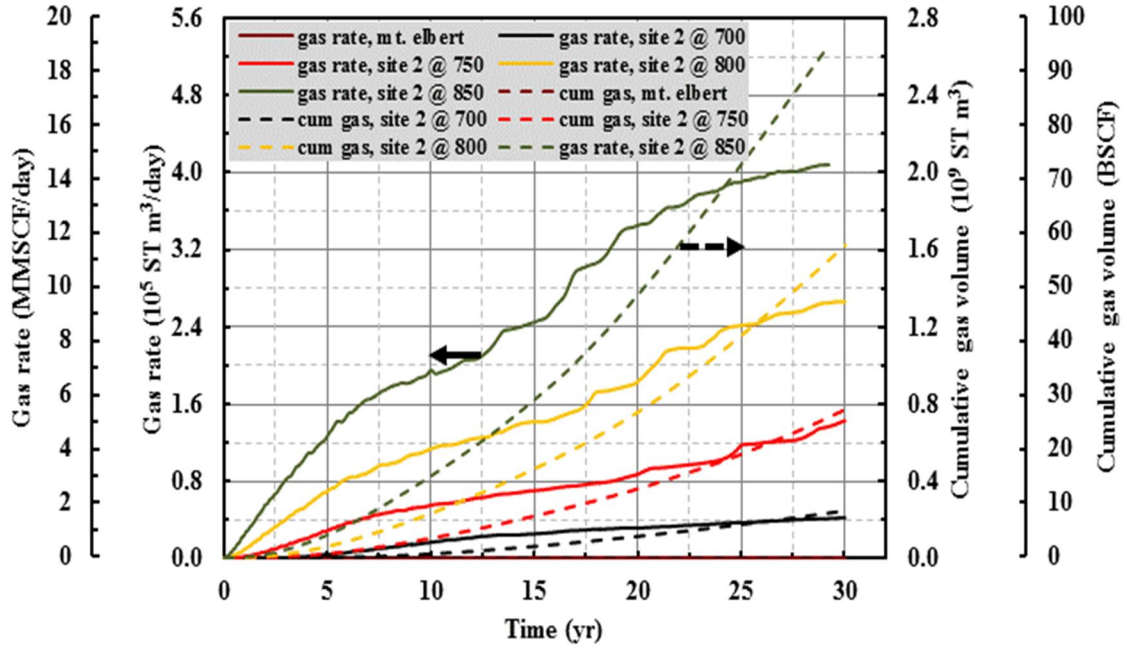

Figure 4-7: Sensitivity of gas rates and cumulative volumes to reservoir depth

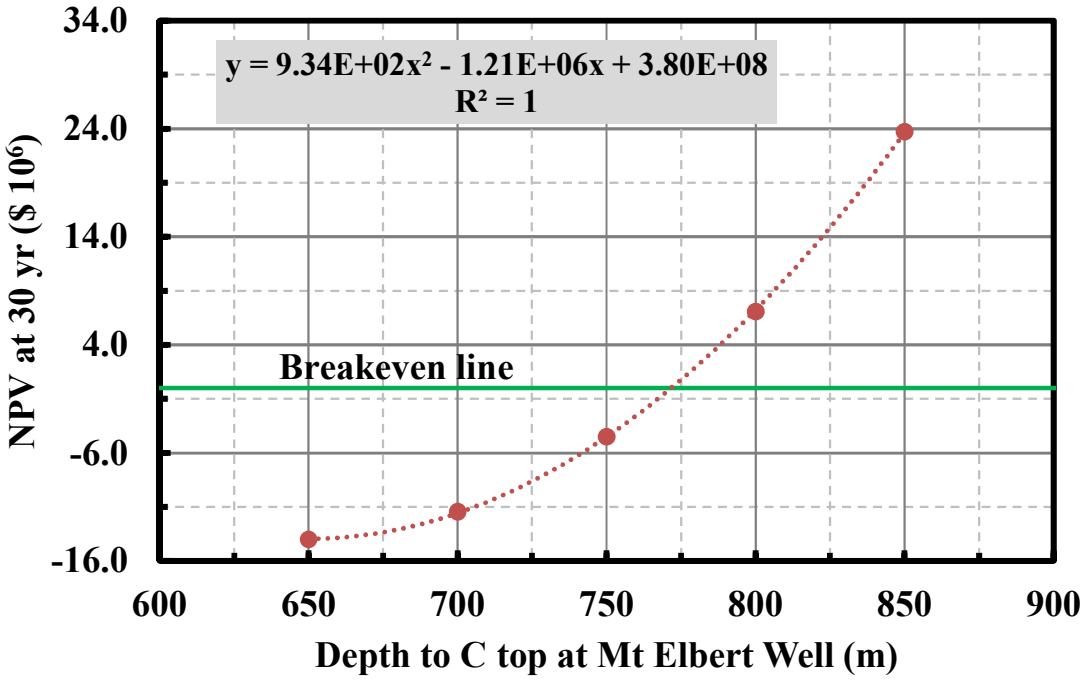

Figure 4-8: Sensitivity of NPV to reservoir depth

4.6.2 Effect of capillary-bound water

The purpose of this section is to investigate the sensitivity of gas rate prediction to the capillary-bound water. Figure 4-9 compares the gas rates obtained from the model with an assumed capillary-bound water equal to 10 % of the total pore volume (reference case) with another model which assumes that the total irreducible water (or total bound water) is all capillary-bound. i.e. $S_{wir} = S_{wcap}$, implying no clay-bound water.

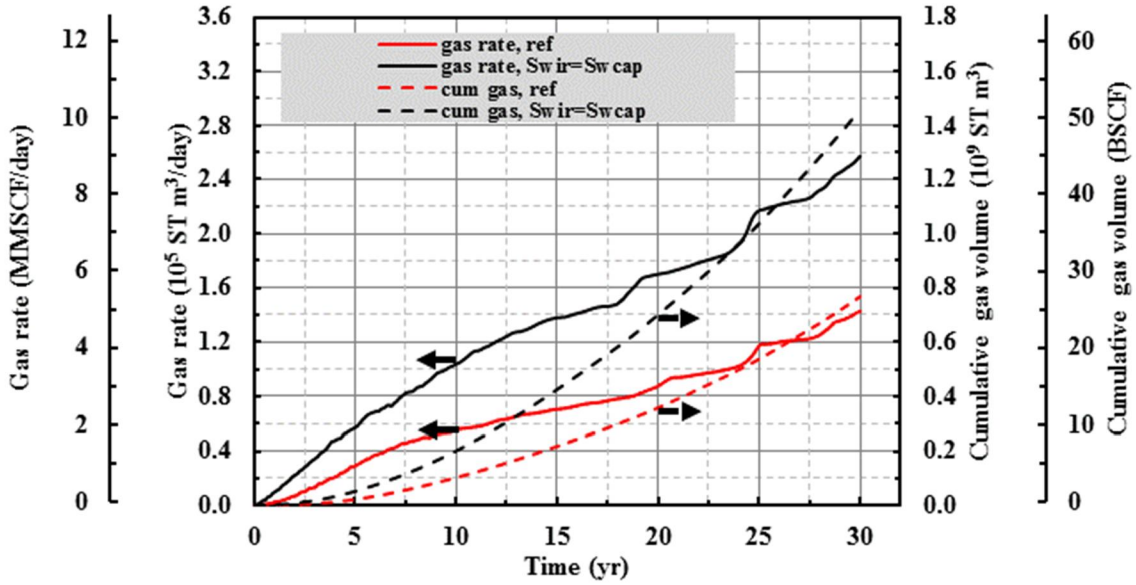

Figure 4-9: Effects of capillary-bound water on gas rates and cumulative volume

Significantly higher gas production rates are predicted for the model with no clay-bound water with a prediction of cumulative volume at the end of 30 yr being 85 % more than the reference case having a fixed 10 % capillary-bound water. A more realistic prediction of gas rates and cumulative volumes will likely lie in the interval between the respective curves shown in Figure 4-9. The results further emphasizes the importance of ongoing studies to accurately describe the relative permeability and capillary pressure models of the hydrate bearing sands of the Alaska North Slope.

4.6.3 Sensitivity to reservoir quality

The purpose of this section is to obtain a measure of reservoir response to the uncertainties in the approximated hydrate saturation distribution coupled with irreducible water saturation, porosity and intrinsic permeability of the reservoir. Using the *Site 2 @ 750* model as a base case, hydrate saturation (coupled with porosity, permeability and irreducible water saturation) were varied. Four additional simulation cases were developed by varying the original (base case) vertical S_h profile. To develop Case 1a, the base case vertical S_h distribution was randomly perturbed such that the resulting mean was 15 % higher, while maintaining the same distribution variance (or standard deviation). Case 1b was developed in a similar fashion but with a mean 15 % less than the base case. Cases 2a and 2b had the same mean as the base case but with standard deviations which are 25 % more and 25 % less than the base case, respectively. The percentage increases in the mean and standard deviation were chosen such that the resulting distribution had a realistic upper bound of S_h at 0.85. The perturbations are graphically illustrated using normalized vertical S_h profiles in Figure 4-10 and the resulting vertical S_h profiles are shown for all five cases in Figure 4-11. A summary statistics of the 3D distributions of hydrate saturation (S_h), porosity (ϕ), intrinsic horizontal permeability (k) and irreducible water saturation (S_{wir}) in the reservoir models in all five cases is presented in Table 4-4. The average properties are based on pore-volumes of each grid block, however, for permeability, the harmonic average of the permeability of all grid blocks is shown.

The gas rates and cumulative gas volume produced are plotted in Figure 4-12 and the cumulative probability distribution of the cumulative gas volumes produced at the end of 30 yr is shown in Figure 4-13. Both figures show that predictions are within narrow ranges with a mean cumulative volume of $1.49 \pm 0.08 \times 10^9$ ST m^3 (52.6 ± 2.8 BSCF).

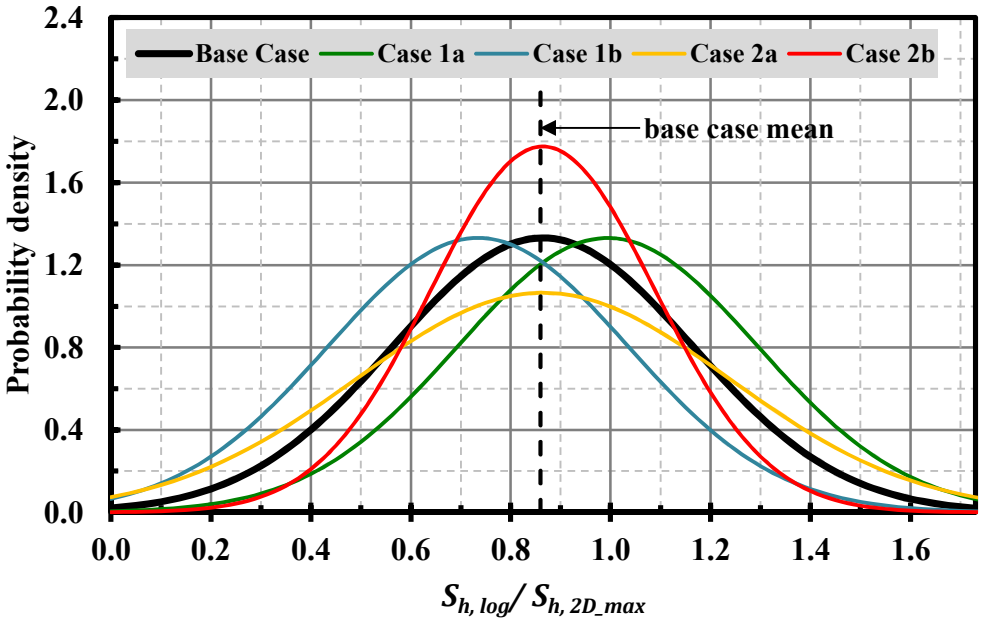

Figure 4-10: Standard normal distribution of normalized vertical S_h profiles for 5 cases

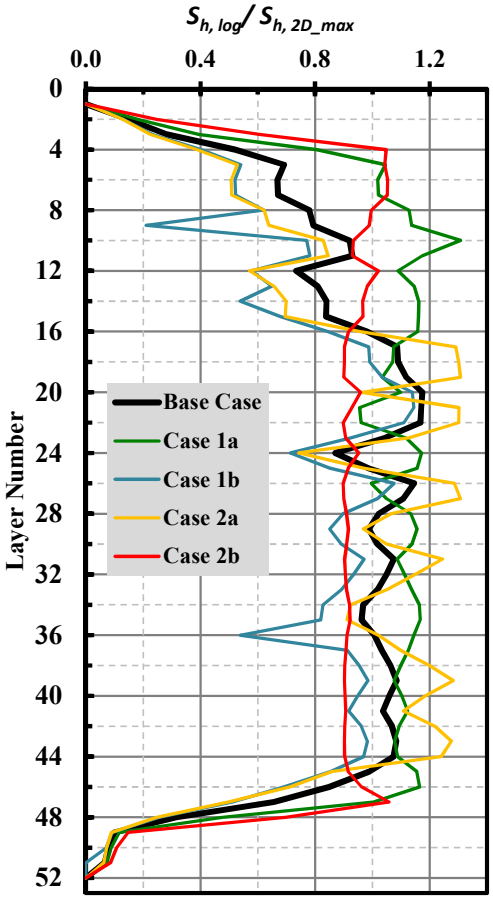

Figure 4-11: Vertical S_h profiles at the Mt. Elbert well location for Site 2

Table 4-4: Summary statistics of varied properties in Site 2 models

Property		Base case	Case 1a	Case 1b	Case 2a	Case 2b
S_h	minimum	0.03	0.03	0.00	0.02	0.03
	maximum	0.76	0.83	0.72	0.82	0.67
	average	0.46	0.53	0.39	0.47	0.45
ϕ	minimum	0.23	0.23	0.22	0.23	0.23
	maximum	0.37	0.39	0.36	0.39	0.35
	average	0.31	0.33	0.30	0.32	0.31
k, mD	minimum	102	102	96	101	104
	maximum	562	693	537	693	475
	average	267	311	228	262	271
S_{wir}	minimum	0.20	0.12	0.21	0.12	0.26
	maximum	0.82	0.82	0.84	0.82	0.81
	average	0.44	0.38	0.50	0.43	0.44

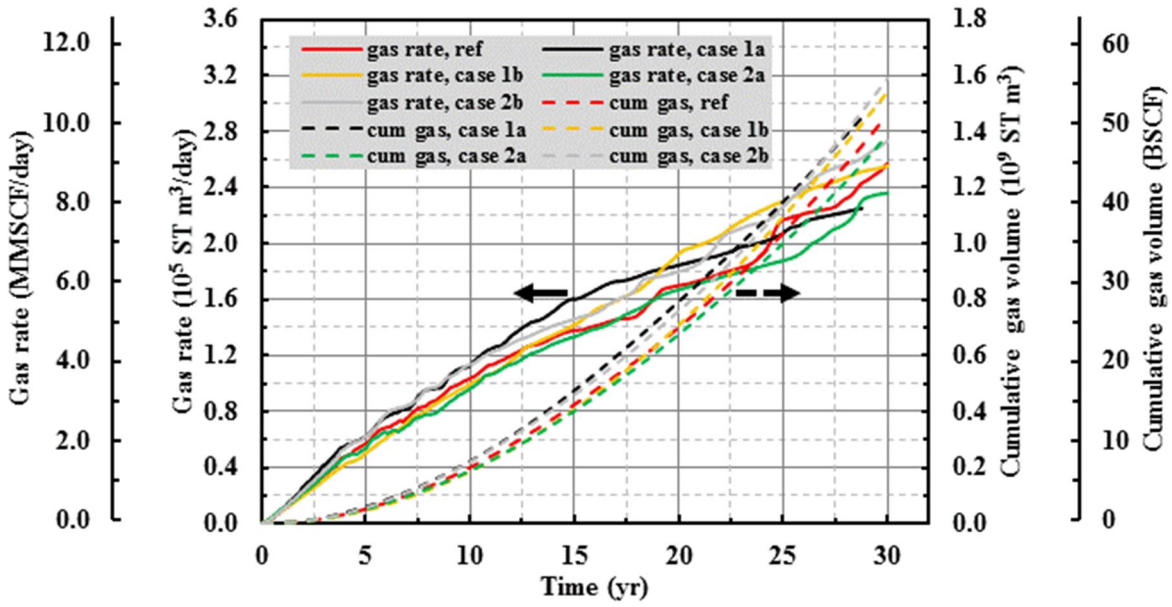

Figure 4-12: Sensitivity of gas rates and cumulative gas volumes to initial hydrate saturation, irreducible water saturation, porosity and intrinsic permeability distribution

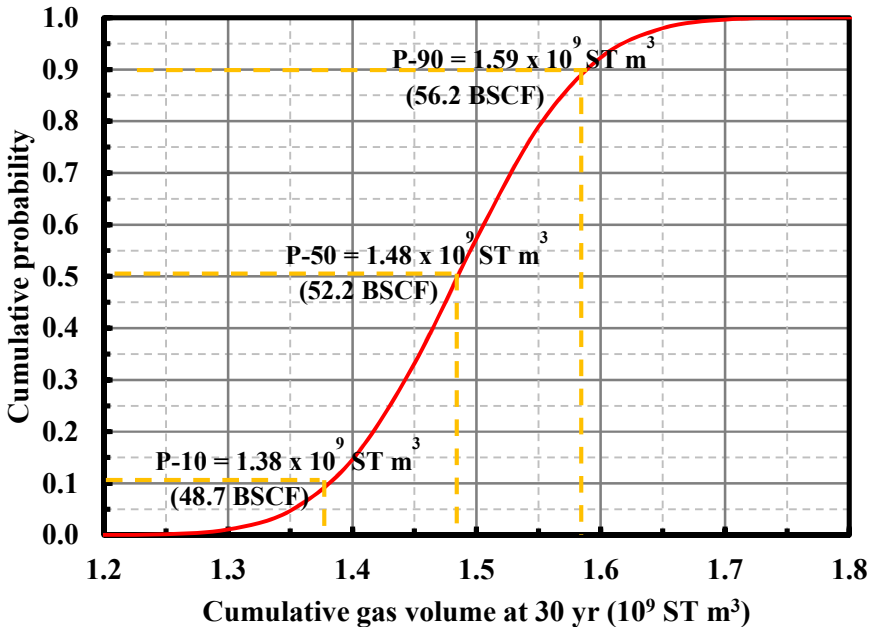

Figure 4-13: Cumulative probability distribution of cumulative volumes produced at 30 yr

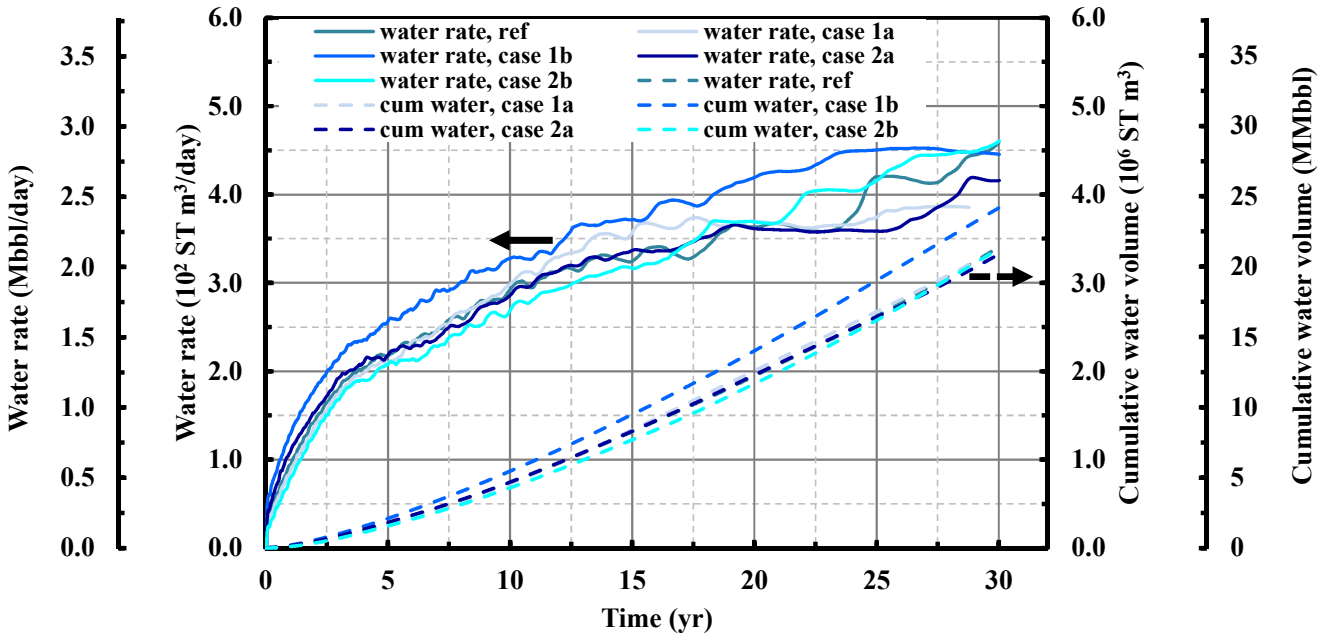

Figure 4-14: Sensitivity of water rates and cumulative volumes to initial distributions of hydrate saturation, irreducible water saturation, porosity and intrinsic permeability

The mean recovery factor computed based on initial volume of gas in place present as hydrate in the reservoir is 22 ± 1 %. Again, this low recovery factor (in spite of the warm reservoir temperatures) suggests the need to investigate more effective ways to enhance the productivity of the hydrate deposits in this region. Plots of water production rates and cumulative volumes shown in Figure 4-14, indicates that range of the cumulative volume of water produced at the end of 30 years is 3.33 – 3.85 x 10^6 ST m^3 or 21 – 24 MMbbl).

Figure 4-15 (a) shows the propagation of the depressurized zone from the wellbore into the reservoir for Case 1b. It indicates that after 10 years, less than half of the reservoir cross-section have been depressurized to 50 % of the initial average reservoir pressure (~ 8200 kPa). Meanwhile, Figure 4-15 (b) shows that the hydrate dissociation potential, indicated by the difference between the reservoir pressure ($P(t)$) and hydrate equilibrium pressure at the prevailing reservoir temperature ($P_{eq}(T(t))$ decreases with time. It is an evidence that during the proximity to hydrate equilibrium becomes more significant as the rate controlling factor as production progresses. Consequently, in the absence of any reservoir stimulation, hydrates will dissociate less readily in the later part of a production period. Figure 4-16 (a) shows the visualization of the hydrate dissociation front as the reservoir is being depressurized while Figure 4-16 (b) shows the increase in the residual gas saturation trapped in the reservoir as the dissociated gas are being produced.

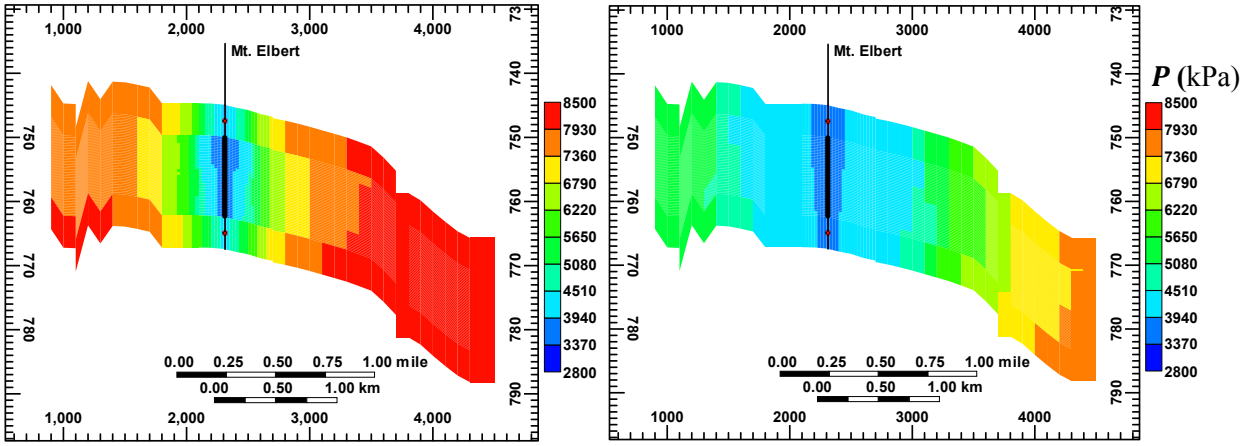

(a)

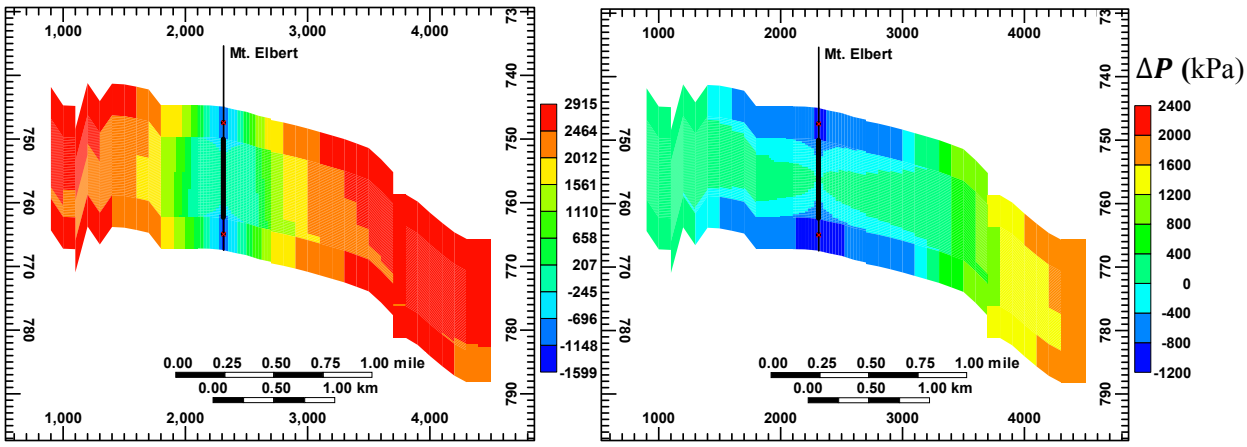

(b)

Figure 4-15: Vertical cross section across the wellbore showing distribution of (a) pressure (P), and (b) difference between reservoir pressure and equilibrium pressure at the current reservoir temperature ($\Delta P = P - P_{eq}(T)$ at $t = 2\ yr$ (left column) and at $t = 10\ yr$ (right column), for Case 1b

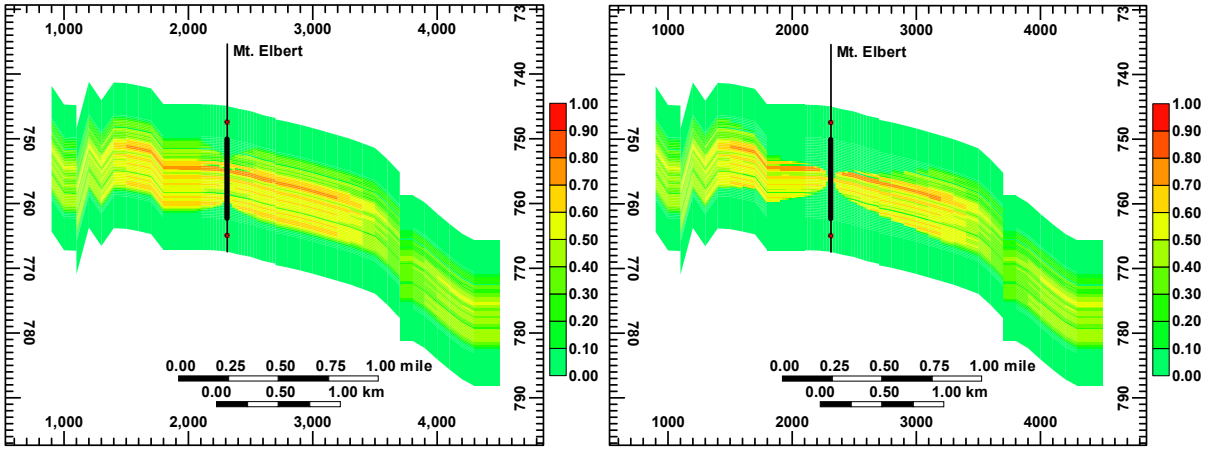

(a)

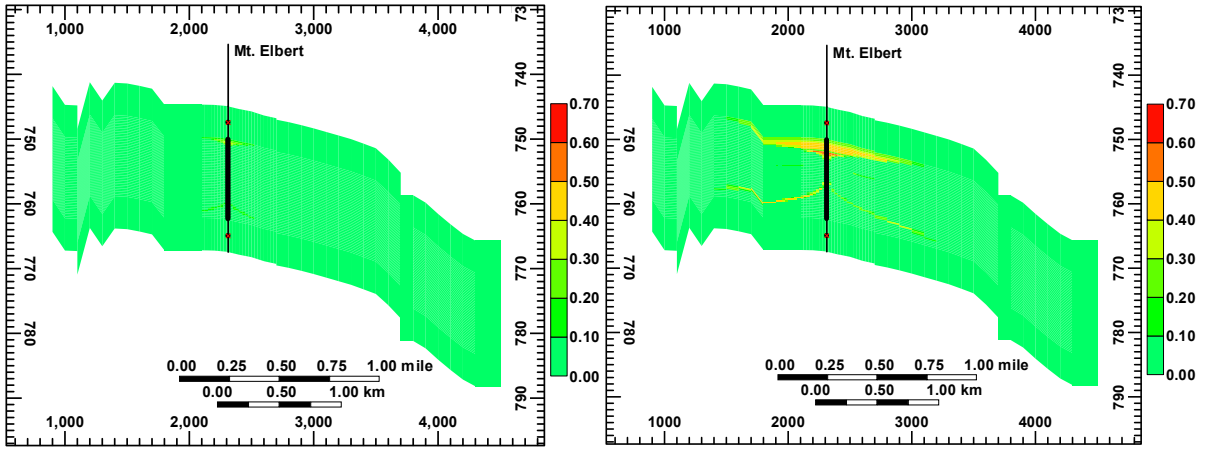

(b)

Figure 4-16: Vertical cross section across the wellbore showing distribution of residual (a) hydrate saturation, and (b) gas saturation, at $t = 2\ yr$ (left column) and at $t = 10\ yr$ (right column), for Case 1b

4.7 Conclusions

Numerical simulations were used to evaluate gas production potential of the reservoir based on the Mt. Elbert methane hydrate deposits of the Milne Point Unit on Alaska's North Slope. In the absence of extensive well log data, reservoir characterization was based mostly on seismic-interpreted reservoir 2D structural maps and S_h distribution, combined with vertical S_h variation derived from the log data of the Mt. Elbert well.

Poor productivity related to the cold temperatures of the original Mt. Elbert formation, necessitated sensitivity simulations on deeper Mt. Elbert-like ("Site 2") hydrate reservoir models with varying depths. As expected, gas rates from the original Mt. Elbert were very low (0 – 10 ST m^3/day), while the deepest Site 2 model (which is 200 m deeper and 7.5 ^{0}C warmer than original Mt. Elbert) produced the highest gas rate (4.07 x 10^5 ST m^3/day or 14.4 MMSCF/day) and cumulative gas volumes (2.66 x 10^9 ST m^3 or 94 BSCF) at the end of 30 years. Economic analysis show that only the deepest two Site 2 models would have a positive net cash inflow at the end of 30 years, with breakeven wellhead gas prices of $ 3.57 and $ 2.06 per MSCF. A Site 2 hydrate prospect that will breakeven exactly at 30 yr would have a reservoir depth between 750 – 800 m (at least 100 – 150 m deeper than the original Mt. Elbert). A quick sensitivity study carried out on capillary-bound water identified it as a very crucial property of the reservoir which needs to be accurately determined because of its significant impact on gas production rates and cumulative volumes.

To obtain a measure of the effect of the uncertainties in the distribution of S_h, ϕ, k and S_{wir} on predictions, four different simulations (Cases 1a, 1b, 2a and 2b) were run by using different statistically perturbed sets of property distributions, with the *Site 2 @ 750* model (100 m deeper than original Mt. Elbert) as a reference case. The narrow range of predictions of gas

and water rates and cumulative volumes further supports the conclusion that the deeper Site 2 prospects, if found, would be more economically viable in the limit of minimal geological uncertainties.

References

1. Collett, T.S., *Natural gas hydrates of the prudhoe bay and kuparuk river area, north slope, alaska.* AAPG bulletin, 1993. **77**(5): p. 793-812.

2. Hunter, R.B., Collett, T.S., Boswell, R., Anderson, B.J., Digert, S.A., Pospisil, G., Baker, R., and Weeks, M., *Mount elbert gas hydrate stratigraphic test well, alaska north slope: Overview of scientific and technical program.* Marine and Petroleum Geology, 2011. **28**(2): p. 295-310.

3. Inks, T., Lee, M., Agena, W., Taylor, D., Collett, T., and Hunter, M.Z.R., *Seismic prospecting for gas-hydrate and associated free-gas prospects in the milne point area of northern alaska.* AAPG Hedberg Special Publication, 2009.

4. Anderson, B., Hancock, S., Wilson, S., Enger, C., Collett, T., Boswell, R., and Hunter, R., *Formation pressure testing at the mount elbert gas hydrate stratigraphic test well, alaska north slope: Operational summary, history matching, and interpretations.* Marine and Petroleum Geology, 2011. **28**(2): p. 478-492.

5. Kurihara, M., Sato, A., Funatsu, K., Ouchi, H., Masuda, Y., Narita, H., and Collett, T.S., *Analysis of formation pressure test results in the mount elbert methane hydrate reservoir through numerical simulation.* Marine and Petroleum Geology, 2011. **28**(2): p. 502-516.

6. Pooladi-Darvish, M. and Hong, H., *Use of formation pressure test results over a hydrate interval for long-term production forecasting at the mount elbert gas hydrate stratigraphic test well, alaska north slope: Implications of uncertainties.* Marine and Petroleum Geology, 2011. **28**(2): p. 535-545.

7. Collett, T.S., Boswell, R., Lee, M.W., Anderson, B.J., Rose, K., and Lewis, K.A., *Evaluation of long-term gas-hydrate-production testing locations on the alaska north slope.* SPE Reservoir Evaluation & Engineering, 2012. **15**(02): p. 243-264.

8. Moridis, G.J., Silpngarmlert, S., Reagan, M.T., Collett, T., and Zhang, K., *Gas production from a cold, stratigraphically-bounded gas hydrate deposit at the mount elbert gas hydrate stratigraphic test well, alaska north slope: Implications of uncertainties.* Marine and Petroleum Geology, 2011. **28**(2): p. 517-534.

9. Anderson, B.J., Kurihara, M., White, M.D., Moridis, G.J., Wilson, S.J., Pooladi-Darvish, M., Gaddipati, M., Masuda, Y., Collett, T.S., and Hunter, R.B., *Regional long-term production modeling from a single well test, mount elbert gas hydrate stratigraphic test well, alaska north slope.* Marine and petroleum geology, 2011. **28**(2): p. 493-501.

10. Myshakin, E.M., Anderson, B.J., Rose, K., and Boswell, R., *Simulations of variable bottomhole pressure regimes to improve production from the double-unit mount elbert,*

milne point unit, north slope alaska hydrate deposit. Energy & Fuels, 2011. **25**(3): p. 1077-1091.

11. Gaddipati, M., *Code comparison of methane hydrate reservoir simulators using cmg stars*. 2008: West Virginia University.

12. Wilder, J.W., Moridis, G.J., Wilson, S.J., Kurihara, M., White, M.D., Masuda, Y., Anderson, B.J., Collett, T.S., Hunter, R.B., and Narita, H., *An international effort to compare gas hydrate reservoir simulators*, in *Proceedings of the 6th International Conference on Gas Hydrates (ICGH 2008)*. 2008: Vancouver, CANADA.

13. Lee, M., Agena, W., Collett, T., and Inks, T., *Pre-and post-drill comparison of the mount elbert gas hydrate prospect, alaska north slope.* Marine and Petroleum Geology, 2011. **28**(2): p. 578-588.

14. Winters, W., Walker, M., Hunter, R., Collett, T., Boswell, R., Rose, K., Waite, W., Torres, M., Patil, S., and Dandekar, A., *Physical properties of sediment from the mount elbert gas hydrate stratigraphic test well, alaska north slope.* Marine and Petroleum Geology, 2011. **28**(2): p. 361-380.

15. Rose, K., Boswell, R., and Collett, T., *Mount elbert gas hydrate stratigraphic test well, alaska north slope: Coring operations, core sedimentology, and lithostratigraphy.* Marine and Petroleum Geology, 2011. **28**(2): p. 311-331.

16. Boswell, R., Rose, K., Collett, T.S., Lee, M., Winters, W., Lewis, K.A., and Agena, W., *Geologic controls on gas hydrate occurrence in the mount elbert prospect, alaska north slope.* Marine and Petroleum Geology, 2011. **28**(2): p. 589-607.

17. Lee, M. and Collett, T., *In-situ gas hydrate hydrate saturation estimated from various well logs at the mount elbert gas hydrate stratigraphic test well, alaska north slope.* Marine and petroleum Geology, 2011. **28**(2): p. 439-449.

18. Torres, M., Collett, T., Rose, K., Sample, J., Agena, W., and Rosenbaum, E., *Pore fluid geochemistry from the mount elbert gas hydrate stratigraphic test well, alaska north slope.* Marine and Petroleum Geology, 2011. **28**(2): p. 332-342.

19. CMG, *Advanced processes & thermal reservoir simulator (stars) user's guide*. 2014, Calgary, Alberta Canada: Computer Modelling Group Ltd.

20. Hunter, R.B., Digert, S.A., Boswell, R., and Collett, T.S., *Alaska gas hydrate research and stratigraphic test preliminary results*, in *The Arctic Energy Summit*. 2007: Anchorage, Alaska.

21. van Genuchten, M.T., *A closed-form equation for predicting the hydraulic conductivity of unsaturated soils.* Soil science society of America journal, 1980. **44**(5): p. 892-898.

22. Stone, H.L., *Probability model for estimating three-phase relative permeability.* Journal of Petroleum Technology, 1970. **22**(02): p. 214-218.

23. Anderson, B.J., Wilder, J.W., Kurihara, M., White, M.D., Moridis, G.J., Wilson, S.J., Pooladi-Darvish, M., Masuda, Y., Collett, T.S., and Hunter, R. *Analysis of modular dynamic formation test results from the mount elbert 01 stratigraphic test well, milne point unit, north slope, alaska*. in *6th International Conference on Gas Hydrates (ICGH 2008)*. 2008. Vancouver, British Columbia, Canada.

5. Overall Conclusions and Recommendations

5.1 Conclusions

The overall goal of this work was to obtain an advanced assessment of the gas production from hydrated reservoirs based true geologically representative reservoir models. The primary subject areas of study were the hydrate accumulations of the PBU "L-Pad" and MPU "Mount Elbert" regions of the Alaska North Slope. It involved comprehensive reservoir characterization to incorporate data-driven 3D heterogeneities of the distribution of geophysical properties of the reservoir in flow simulation models. Depressurization was used to obtain predictions of gas and water production rates, and reservoir response under varying field scenarios were studied.

In the L-Pad models, geostatistical porosity distribution models of the hydrate-bearing D and C sand units were developed based on 78 well log data, from which distribution of porosity-dependent hydrate saturation and intrinsic permeability were estimated. The resulting reservoir models accounted for the actual geological features (reservoir geometry, fault and hydrate water contact). Numerical flow simulations were conducted using CMG STARS.

The first set of simulations were done to quantify the uncertainties associated with predictions from this model using vertical and inclined production wells using 10 geostatistical realizations of porosity distribution.

This was followed by a study on the sensitivity of reservoir performance to well configuration and completion. Further sensitivity studies included efforts to obtain a measure of the effect of reservoir dimensionality and heterogeneity on gas rate predictions. Extensive study of gas flow and patterns provided a clearer explanation and better understanding of the

phenomenon and effect of secondary hydrate formation on gas production. Flow assurance studies were conducted to determine how wellbore conditions need to be managed to prevent secondary formation of hydrates in the well during production. Finally, economic assessment was carried out to determine the viability of a long-term field development using multiple wells. The following are the summary of the conclusions reached

- Uncertainties in predictions based on this model were only about 1.7 % and 0.5 % of the mean values 5.33±0.09 x 10^8 ST m^3 (18.82±0.32 BSCF) and 6.07±0.03 x 10^8 ST m^3 (21.44±0.11 BSCF)) for the vertical and inclined wells, correspondingly. The results are an indication of the reliability of the data driven model and provides an indication that the amount of well log data used for the study is sufficient to adequately characterize the reservoir.
- Sensitivity of reservoir performance to well design showed that the maximum overall recovery achievable were in the range 30 – 40 % of the original GIP in form of hydrates, with the well configuration having two lateral sections each penetrating the D and C sands having the highest recovery. This indicates a need for the application of a more advanced recovery technique to enhance reservoir performance within a typical life span of a producing well.
- Large amounts of liquid phase produced (2.74 – 3.61 x 10^6 ST m^3 or 1.72 – 2.27 x 10^7 bbl) in all well configurations suggest a need provision for downhole gas-water separation in the wellbore design in order to reduce the load on the production lift system.
- Study also showed that the presence of hydrate-water contact did not have any significant impact on the cumulative gas volume produced at the end of 30 years.

However, a model with water contact produced 90 % more volume of water compared with that without water contact. From a water production management perspective, this result may have substantiated a basis for the consideration of a production method which would involve an initial injection of CO_2 into the free-water zone just below the hydrate-water contact to form CO_2 hydrates, which would now be followed by the production phase using the depressurization technique.

- A simplified 2D geometry for a hydrate reservoir model and assumption of vertical heterogeneity in porosity and hydrate saturation led to underestimation of reservoir productivity by about 38 % in comparison with the 3D model employed in this study. On another hand, modeling gas production from the hydrate sand units using uniform intrinsic permeability (734 mD in the horizontal and 367 mD in the vertical direction) overestimates the cumulative gas volume produced at the vertical well by around 40 % comparing with the heterogeneous permeability representation.
- Based on the 3D heterogeneous models, secondary hydrates were formed away from the producing well and were seen as short-lived patches of increased or sustained hydrate saturations. The reason of their appearance was attributed to local pressure fluctuations caused by temporal gas trapping during mobile phase flow in complex 3D porous network containing dissociating hydrate. This was another evidence of the profound importance of a 3D heterogeneous representation of a reservoir system which captures details of actual geological settings.
- Based on the current predictions of water production, flow assurance studies show that very large volumes of methanol (> 308 m^3 /day or 1938 bbl/day) need to be injected into the wellbore in order to inhibit the secondary formation of hydrates in the wellbore,

making it impractical. These numbers, again, emphasize the need for an effective water production management. As a possible alternative, calculations show that minimum DEH requirements are 8.73, 68.05 and 67.83 W/m heating power per unit length of wellbore, corresponding to the 30, 50 and 100 kW pump power outputs, which translates to a requirement that the wellbore wall temperature (T_w) should be maintained at 8, 25 and 25 ^{0}C, when using a pump with power outputs of 30, 50 and 100 kW, respectively. These results suggest that DEH might be a more feasible alternative than methanol injection, based on the predicted water production rates.

- The economic viability of different options of long-term field development were evaluated using a generalized 3D rectangular geometry. Among the four scenarios considered, the most promising field development option is the use of four inclined wells, however, all of the options remain economically unattractive with NPVs in the range -$ 21.3 – -$ 13.8 million at the end of the production period. Therefore, an aggressive enhanced recovery method may be required to improve on the economic viability of long term production from this particular site.

- The productivity of a probable hydrate deposit downdip and to the east of the L-Pad was also studied for reservoirs with depths 50 and 100 m, respectively. The maximum gas rates achieved were 1.1 and 2.4 times more than the maximum production rate achieved from the original L-pad, respectively for the 50 and 100 m-depth models. Cumulative volumes achieved at the end of 30 yr, are 45 and 76 % more than the reference case for the 50 and 100 m-downdip models respectively. At 30 yr, NPVs are $ 0.28 and $ 21.69 million, and breakeven gas wellhead prices are $ 5.27 and $ 3.58 per MSCF for reservoir depths 50 and 100 m, respectively. These show that the L-Pad

downdip would be a much more favorable production site than the L-Pad, however, geological risks associated with the downdip sites make predictions less reliable.

The primary goal of the Mt. Elbert models was to evaluate alternative production sites with deeper hydrate accumulations and minimal geological risks within the MPU, with the C unit hydrates being the production target. In the absence of extensive well log data (unlike the L-Pad), reservoir characterization was based mostly on seismic-interpreted reservoir 2D structural maps and S_h distribution, combined with vertical S_h variation derived from the log data of the Mt. Elbert well. Low reservoir productivity related to the cold temperatures of the Mt. Elbert formation (as shown by previous studies), necessitated sensitivity simulations on deeper Mt. Elbert-like ("Site 2") hydrate reservoir models with varying depths. The models incorporated, as much as possible, the structural and geophysical heterogeneities of the reservoir by maximizing the utilization of the available field data. Using the Mt. Elbert model as a reference case, sensitivity of predictions of gas rates and cumulative volumes to reservoir depths (hence temperature) was determined. The study obtained a qualitative measure of the uncertainties in the approximation of reservoir quality (hydrate saturation, porosity and intrinsic permeability) and its implication on gas production. The following are the specific conclusions reached from the results of the flow simulations:

- As expected, gas rates from the original Mt. Elbert were very low (0 – 10 ST m^3/day), while the deepest Site 2 model (which is 200 m deeper and 7.5 ^{0}C warmer than original Mt. Elbert) produced the highest gas rate (2.67 x 10^5 ST m^3/day or 9.4 MMSCF/day) and cumulative gas volumes (1.62 x 10^9 ST m^3 or 57 BSCF) at the end of 30 years. Economic analysis show that only the deepest Site 2 model would have a positive net

cash inflow at the end of 30 years, with a breakeven wellhead gas price of $ 3.57 per MSCF. A Site 2 hydrate prospect that will breakeven exactly at 30 yr would have a reservoir depth between 750 – 800 m (at least 100 – 150 m deeper than the original Mt. Elbert).

- To obtain a measure of the effect of the uncertainties in the distribution of S_h, ϕ, k and S_{wir} on predictions, four different simulations (Cases 1a, 1b, 2a and 2b) were run by using different statistically perturbed sets of property distributions, with the *Site 2 @ 750* model (100 m deeper than original Mt. Elbert) as a reference case.
- From the uncertainty assessments of distribution of S_h, ϕ, k and S_{wir}, it was observed, interestingly, that the cumulative volume of gas produced from all sensitivity cases were all significantly (80 – 100 %) higher than the reference case. The observed higher gas rates was attributed its ability to a) achieve a more effective depressurization to its higher average effective permeability of the reservoir, b) allow more of the dissociated gas to flow from the reservoir to the wellbore which is related to the higher average S_{wir}, that provides less impedance due to free water flow, when compared with the reference case.
- The results gave an indication that optimum reservoir performance is strongly dependent on reservoir quality (Q), defined by a complex relationship between S_h, ϕ, k and S_{wir}, and that local variations of this reservoir quality, especially around a production well, may further impact on the productivity of reservoir. Furthermore, the results emphasize that the model predictions of production potential from a Site 2 (if found) would be valid, only if it has similar petro-physical characteristics as the Mt Elbert prospect.

While information obtained from this work would be most beneficial to support the planning of the proposed long term hydrate production tests and subsequent field development of the ANS, results may also be useful in the planning and development of other hydrate prospects in other locations.

5.2 Recommendations

It is recommended that future work in the development of a hydrate resource focus on improving on the characterization and reliability of the reservoir models, investigating advanced recovery techniques to enhance production and providing solutions to operational challenges associated with hydrate production. A lifecycle assessment should also be conducted, which would involve addressing environmental concerns associated with hydrate production and establishing the utilization of the produced gas on site. Specific examples of these future areas of study include:

- Incorporating depositional trends in the geostatistical models of the L-Pad models that will result into more geologically representative models. Ideally, a seismic survey of the L-Pad region would also provide more information on the lateral continuity of the hydrate accumulations
- Continuous improvements should be made on the reservoir models by validating the model predictions with field production data through history matching, as soon as it is available
- Investigation of several production techniques which will enhance recovery from hydrates and / or lead to a more effective water production management should be studied. For instance, a combination of producer wells and heat injection (circulating)

wells can be designed to enhance recovery. Also, depressurization can be preceded by injection of CO_2 in free-water zones below a production target to form CO_2 hydrates, in order to minimize volume of water produced.

- Further flow assurance studies need to be conducted in order to address operational issues like blockage of equipment due to sand accumulation, ice and secondary hydrate formation during temporary shutdowns, etc. This would help to develop working startup and shutdown procedures.
- Geomechanical studies would provide information about reservoir subsidence due to compaction as a result of hydrate dissociation, integrity of the wellbore during production and volumes of sand produced. Other environmental concerns such as carbon footprint, leakage of gases in the reservoir and gas emissions to the atmosphere need to be addressed.
- Establishing the utilization of produced gas on field would help in the determination of the location of production pads and gathering lines in the planning stage of field development

Appendix

A. L-Pad Geostatistical Analysis of Porosity

This section provides more details on the geostatistical development discussed in Section 3.4. The original well log-derived porosity values within the sand intervals were trimmed to be within the range of 0.16 – 0.45, which includes about 96 % of the all original porosity values (Figure A-1 – Figure A-3). Trimming was necessary to reduce the variability of the hydrate-bearing sand porosity, because preliminary simulations showed that significant porosity fluctuations at adjacent grid blocks might lead to numerical convergence problems. Figure A-4 shows a gridded location map of the intersection of the L-Pad wells with the top of the D sand. It reveals some "clustering" nature of the well positions / porosity data in the x-y plane. Clustering introduces some "bias" in the distribution; therefore, in an attempt to remove bias and to have a representative porosity histogram of the entire area, a cell declustering technique was used[1-3]. The main idea of cell declustering is to assign a weight, w_i, to each data value as the reciprocal of the product of the number of occupied cells (L_0) and the number of data in the same cell, $n_c(i)$. Therefore, values in cells with more data receive less weight than those in sparsely sampled area. By varying the cell sizes, a "declustered" mean ($\bar{x}$) was calculated using Equation (A-1).

$$\bar{x} = \sum_{i=1}^{n} w_i x_i , \qquad where\ w_i = \frac{1}{L_0 n_c(i)} \tag{A-1}$$

$i = 1 \ldots n$, with n = total number of data points.

The declustered mean was calculated for each cell size and the cell size with the minimum was selected. The declustered mean were 0.36, 0.25 and 0.36 for D, DC shale and C units, respectively.

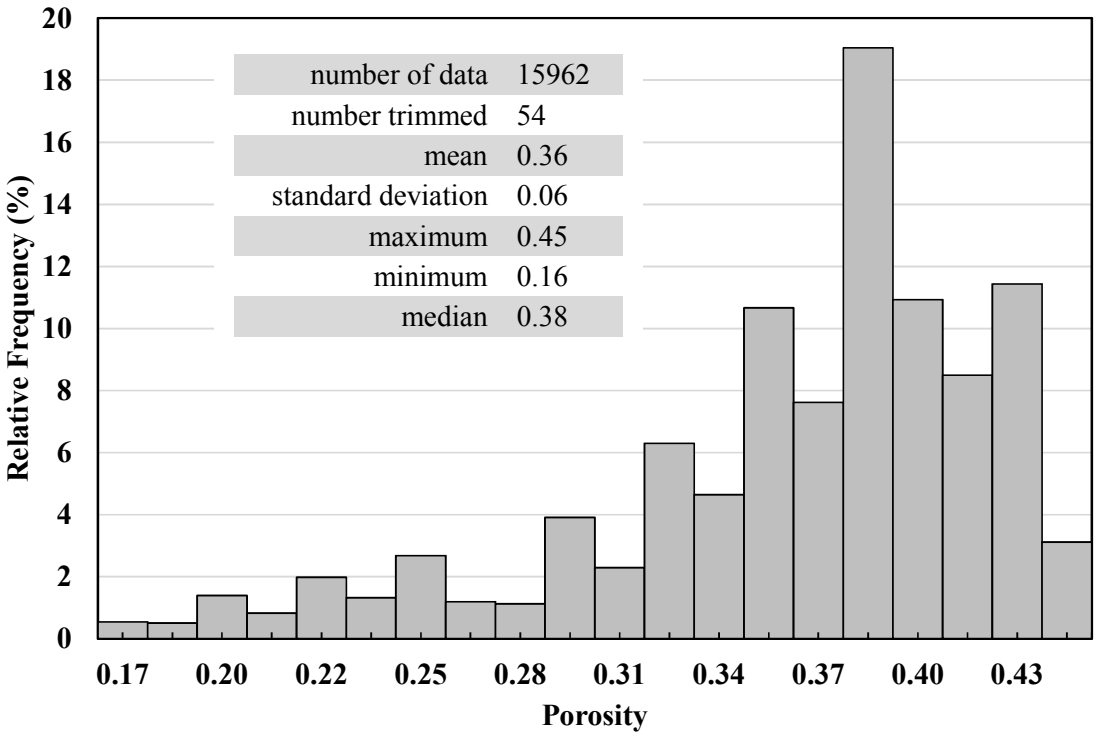

Figure A-1: Relative frequency histogram of trimmed originally estimated porosity values in the D sand interval

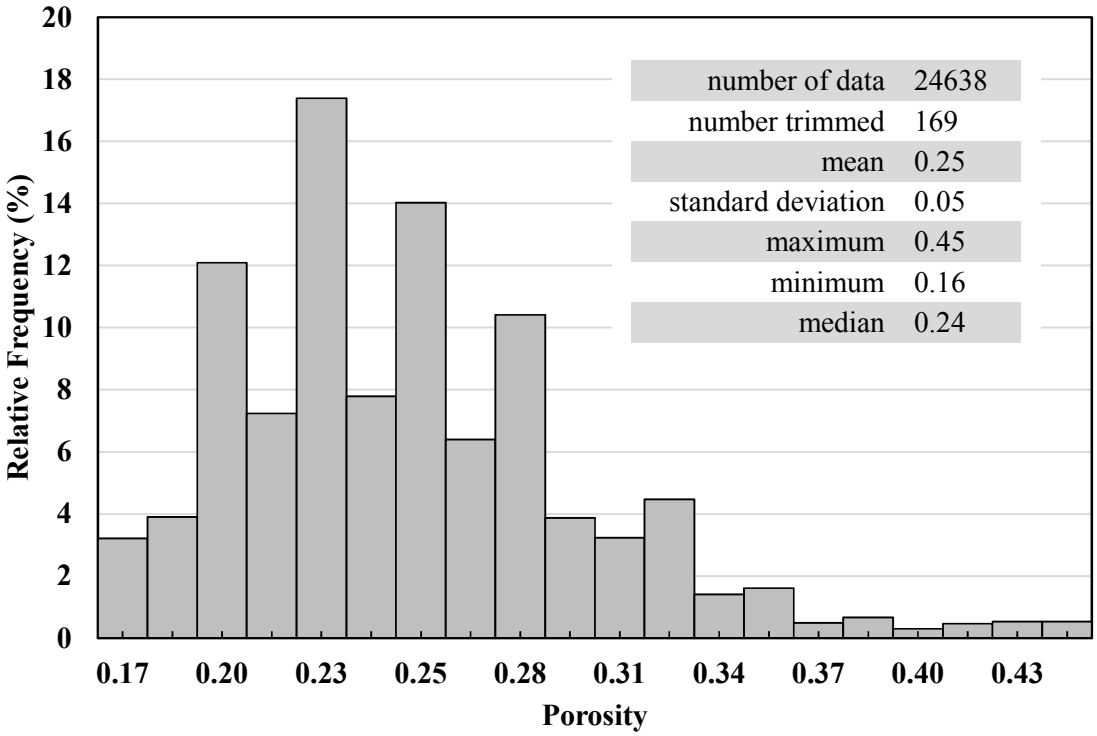

Figure A-2: Relative frequency histogram of trimmed originally estimated porosity values in the DC shale interval

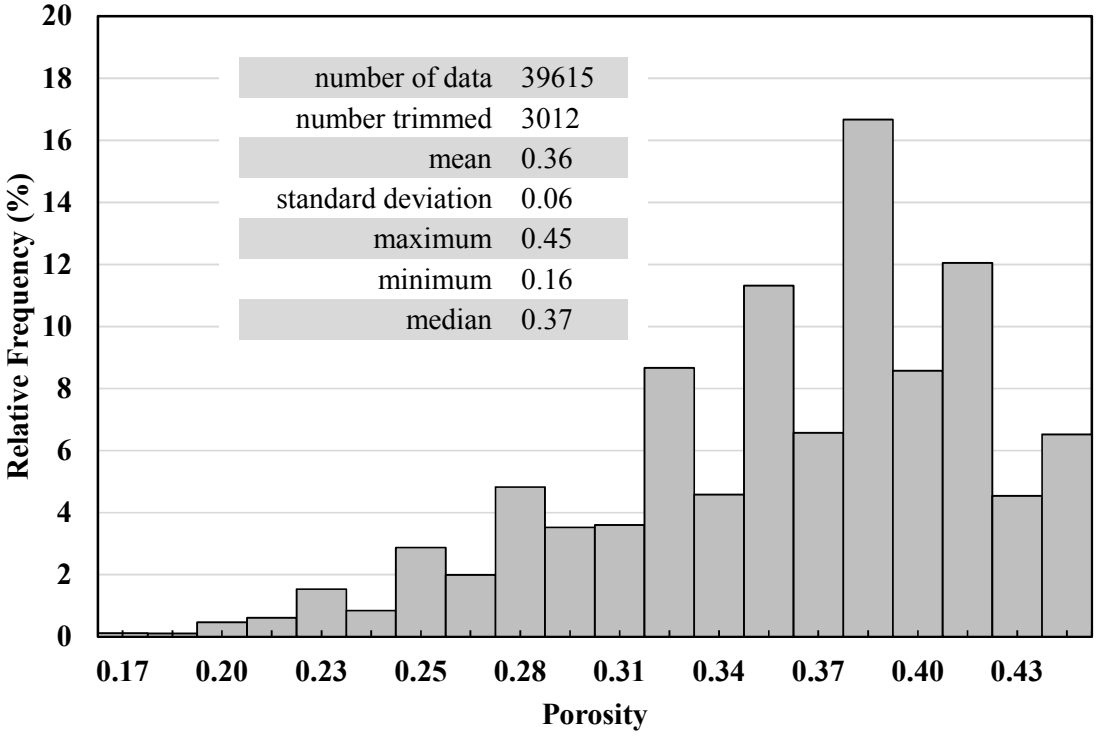

Figure A-3: Relative frequency histogram of trimmed originally estimated porosity values in the C sand interval

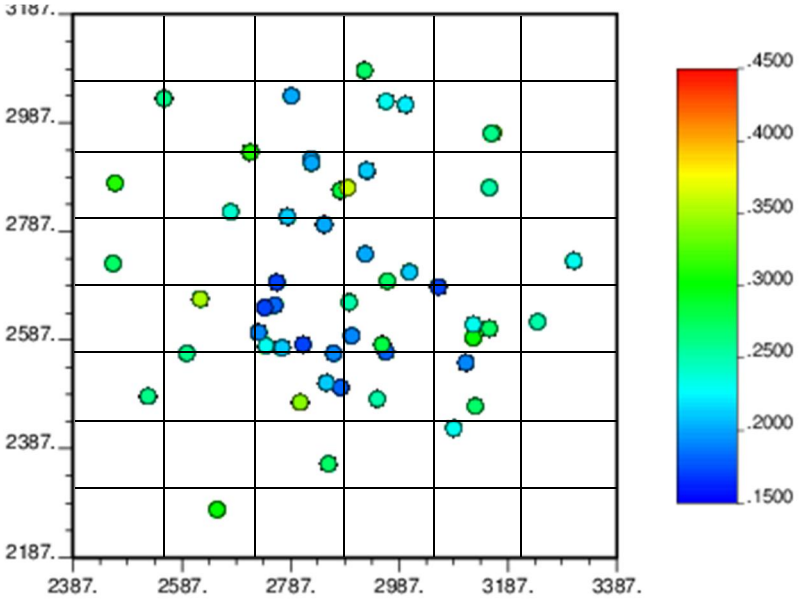

Figure A-4: Well location map showing porosities at the top of the Unit D sand

Using normal score transformations, the porosity distributions were normalized (Figure A-5, Figure A-6 and Figure A-7) and were used in subsequent and separate variogram analyses and modeling for each D, DC shale and C units, respectively.

The variogram is a measure of the variability of a quantity sampled in different locations with respect to spatial coordinates. It is a function of both distance and direction and mathematically defined as:

$$\gamma(\boldsymbol{h}) = \frac{1}{2N(\boldsymbol{h})} \sum_{i=1}^{N(\boldsymbol{h})} [z(\boldsymbol{x}_i) - z(\boldsymbol{x}_i + \boldsymbol{h})]^2 \qquad (3)$$

where,

$\boldsymbol{h}$ – displacement vector between a pair of samples (lag distance);

$N(\boldsymbol{h})$ – number of sample pairs separated by **h**;

$\boldsymbol{x}_i$ – position vector of one of the ithsample pair;

$z(\boldsymbol{x}_i)$ – sampled quantity with position vector $\mathbf{x}_i$;

$\gamma(\boldsymbol{h})$ – variogram of any two sample pairs separated by **h**.

The next step was to estimate variograms in the principal directions, *i.e.* directions of maximum and minimum geological continuity. Two angles define variogram directions – the azimuth angle (ϕ) and the dip angle (θ), as illustrated in Figure A-8. At PBU L-Pad the hydrate accumulation has a calculated structural NE dip ~2.3^o downwards from the horizontal line, which is assumed as the horizontal direction of maximum geological continuity. However, since the reservoir top has been "flattened" (as described in Section 3.4), isotropic horizontal variograms were calculated with dip angle of 0 ^{0} and a large azimuthal angle tolerance of +/-180 ^{0}. A vertical variograms were computed with dip angle of – 90 ^{0}. Table A-1 summarizes the specific parameters used for the three separate facies.

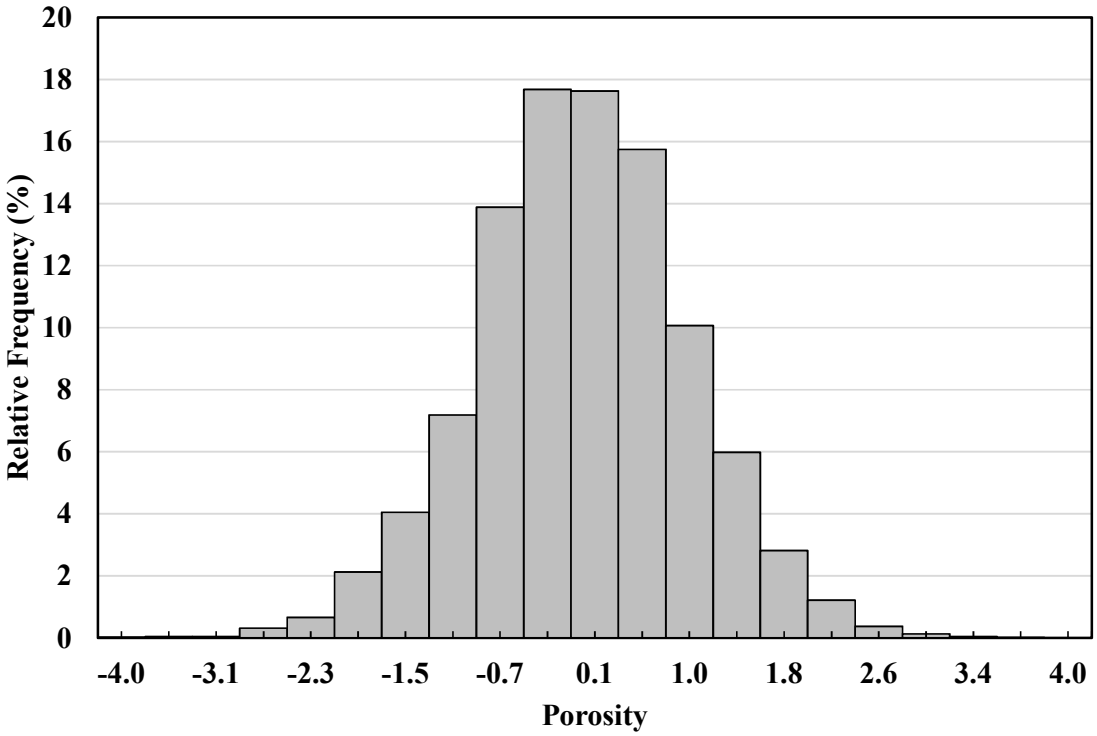

Figure A-5: Relative frequency histogram of normalized porosity for D unit

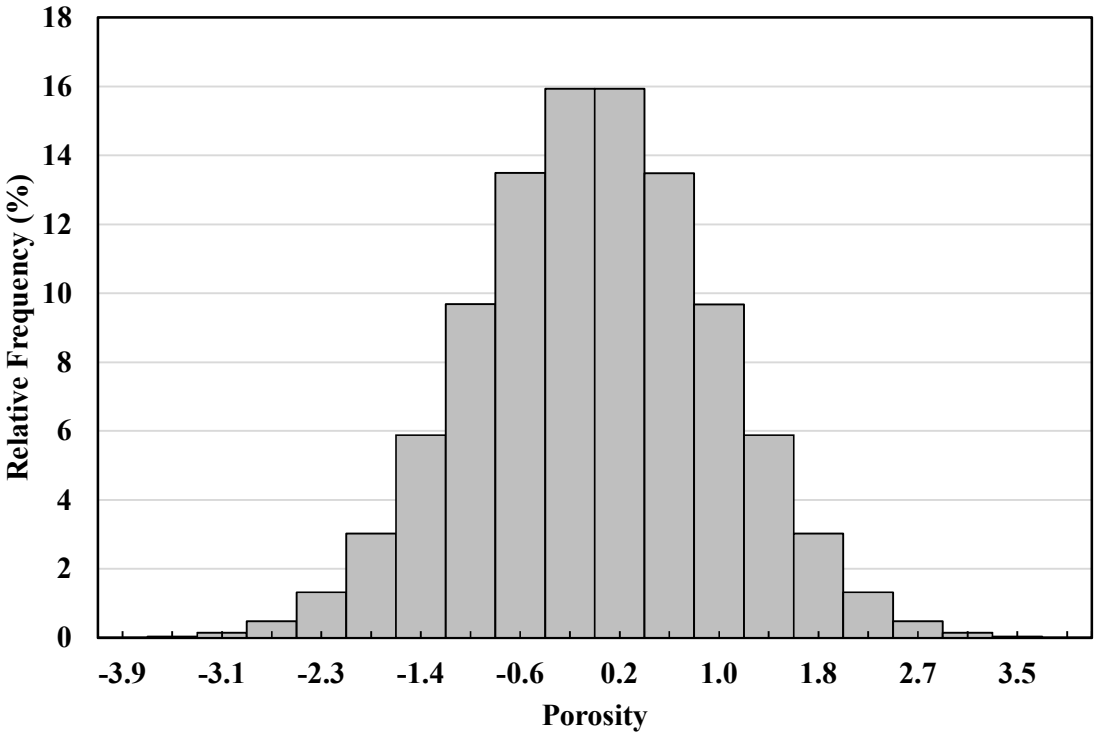

Figure A-6: Relative frequency histogram of normalized porosity for DC shale unit

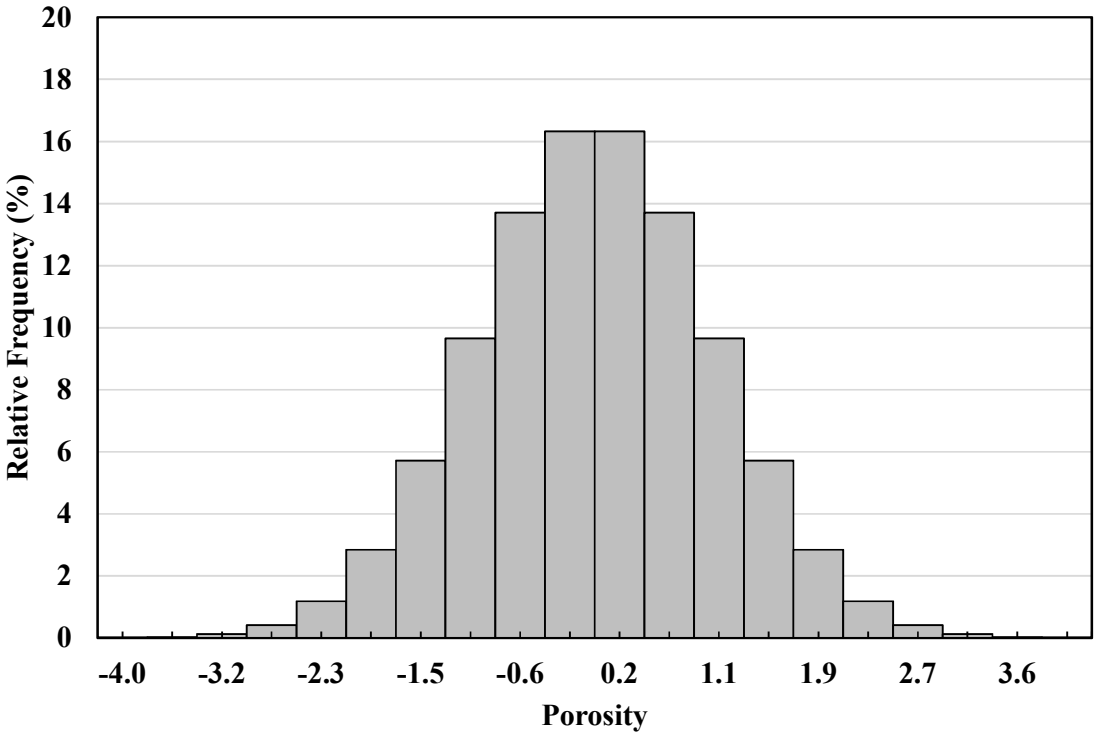

Figure A-7: Relative frequency histogram of normalized porosity for C unit

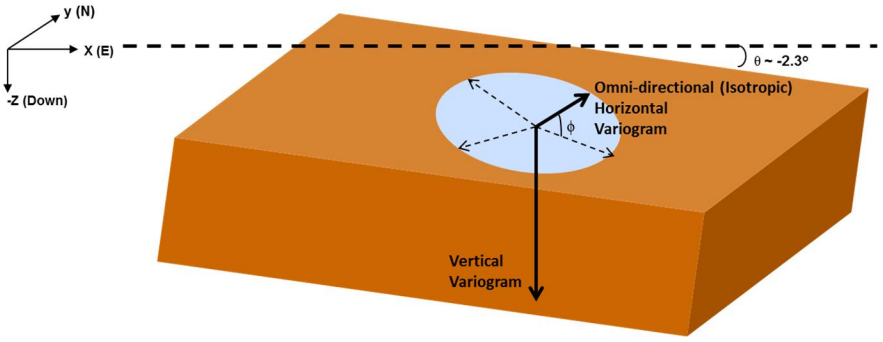

Figure A-8: Anisotropic variogram directions with dip and azimuth angles.

Table A-1: Parameters used for variogram calculations in D, DC shale and C units

Variogram direction	Dip angle (^{0})	Parameter	D unit	DC shale	C unit
Horizontal	0	Number of lags	10	10	10
		Unit lag separation distance (m)	50	50	70
		Lag tolerance (m)	50	50	70
		Dip tolerance (^{0})	2	5	5
Vertical	- 90	Number of lags	18	40	40
		Unit lag separation distance (m)	0.50	0.50	0.5
		Lag tolerance (m)	0.25	0.25	0.5
		Dip tolerance (^{0})	10	10	10

The number of lags represent the largest separation distance in which variograms are evaluated and is in the neighborhood of half the maximum separation distance in the data. This is the region in which computed variograms are known to be more realistic[3]. The unit separation (lag) distances were chosen to maximize the number of porosity data used to calculate the variogram for any given pair of spatial coordinates separated by a lag distance[3]. The lag tolerances were chosen to smoothen the variograms while preserving the variogram structure and the dip angle tolerances were chosen to capture the data in moderately deviated wells[3, 4]. Plots of the calculated (or sample) horizontal and vertical variograms and their models are shown for all three facies in Figure A-9. The sample horizontal and vertical variograms were fitted simultaneously using a combination of positive definite models (refer to Section 2.4.1) such that a) the sum of their variance contributions is equal to 1 and (b) they fit the sample variograms within a mean square error of no more than 1 % of the theoretical sill. **Error! Reference source not found.** shows the parameters of the variogram models for D, DC shale and C units, respectively.

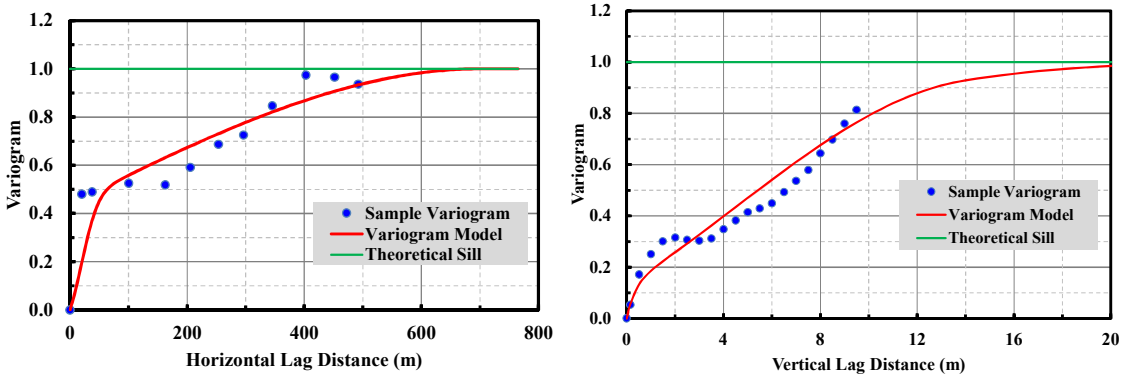

(a)

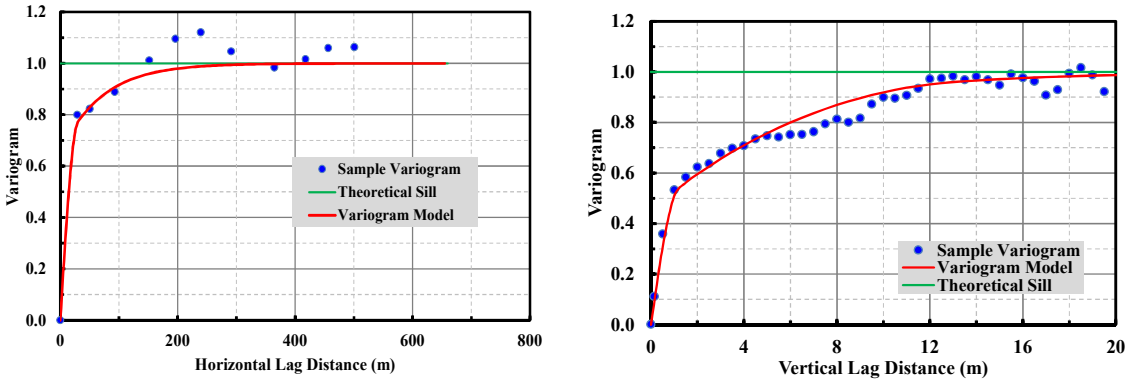

(b)

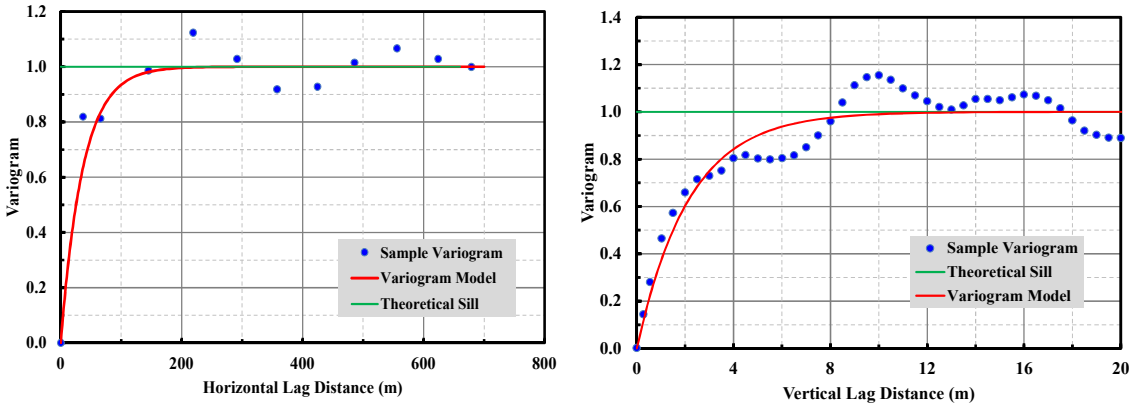

(c)

Figure A-9: Horizontal (left column) and Vertical (right column) sample variograms of (a) D, (b) DC shale, and (c) C units, and their fitted models

Table A-2: Variogram model parameters for D, DC shale and C units

Unit	Model type (index, *i*)	Variance contribution	Horizontal Range, a_{hor} (m)	Vertical Range, a_{vert} (m)
D	Spherical (1)	0.56	700	14.0
	Exponential (2)	0.13	60	1.0
	Gaussian (3)	0.31	60	20.0
DC shale	Spherical (1)	0.45	30	1.2
	Spherical (2)	0.20	30	13.0
	Exponential (3)	0.35	210	18.0
C	Exponential (1)	1.00	110	6.5

The variogram functions are mathematically expressed in Equations (A-2), (A-3) and (A-4), for the facies D, DC shale and C, respectively.

$$\boldsymbol{\gamma}_D(h) = 0.56\begin{cases}\left[1.5h_1 - 0.5{h_1}^3\right], & h_1 \le 1\\ 1, & h_1 \ge 1\end{cases} + 0.13(1 - e^{-3h_2}) + 0.31\left(1 - e^{-3h_3^2}\right) \quad \text{(A-2)}$$

$$\boldsymbol{\gamma}_{DCshl}(h) = 0.45\begin{cases}\left[1.5h_1 - 0.5{h_1}^3\right], & h_1 \le 1\\ 1, & h_1 \ge 1\end{cases} + 0.20\begin{cases}\left[1.5h_2 - 0.5{h_2}^3\right], & h_2 \le 1\\ 1, & h_2 \ge 1\end{cases} + 0.35(1 - e^{-3h_3}) \quad \text{(A-3)}$$

$$\boldsymbol{\gamma}_C(h) = \begin{cases}\left[1.5h_1 - 0.5{h_1}^3\right], & if\ h_1 \le 1\\ 1, & if\ h_1 \ge 1\end{cases} \quad \text{(A-4)}$$

where, $h_i = \sqrt{\left(\frac{h_{vert}}{a_{vert_i}}\right)^2 + \left(\frac{h_{hor}}{a_{hor_i}}\right)^2}$, $i = 1, 2, \ldots$

$h_{vert} = vertical\ distance\ between\ sampled\ and\ u\ nsampledpoints$

$h_{hor} = horizontal\ distance\ between\ sampled\ and\ u\ nsampledpoints$

$a_{vert} = variogram\ range\ in\ the\ vertical\ direction$

$a_{hor} = variogram\ range\ in\ the\ horizontal\ direction$

Using the model variogram as weighting functions, Ordinary Kriging along with Sequential Gaussian Simulation was performed using the normal score-transformed porosity as the input data on a rectangular reservoir grid with high and low horizontal (x x y) resolutions (Table A-3).

Table A-3: Grid resolution, dimension and sizes used for D, DC shale and C units

Horizontal resolution	**Unit**	**Number of grids**		**Grid size (m)**	
		$nx = ny$	nz	$\Delta x = \Delta y$	Δz
High	D	255	40	5	0.5
	DC shale		60		
	C		100		
Low	D	51	40	25	0.5
	DC shale		60		
	C		100		

As discussed in Section 2.4.2, Sequential Gaussian Simulation ensures that the location of the sample data honor their original values (unlike the case if only Ordinary or Simple Kriging was used). Search ellipsoids which have dimensions within the ranges of the variograms were used and search was restricted to a maximum of eight nearest points. The output from the stochastic simulation, which is a normal score porosity, was transformed back to actual porosity values. These porosity values were read into CMG STARS by means of a code generated in MATLAB, and then using the map data of the depth to the top of the reservoir, the rectangular "flattened" geometry was converted back to reflect the actual reservoir geometry. Figure A-10 and Figure A-11 show the horizontal and vertical cross sections of the high resolution geostatistical porosity distribution for selected layers. The 3D structure has been given in Figure 3-7 of the main text.

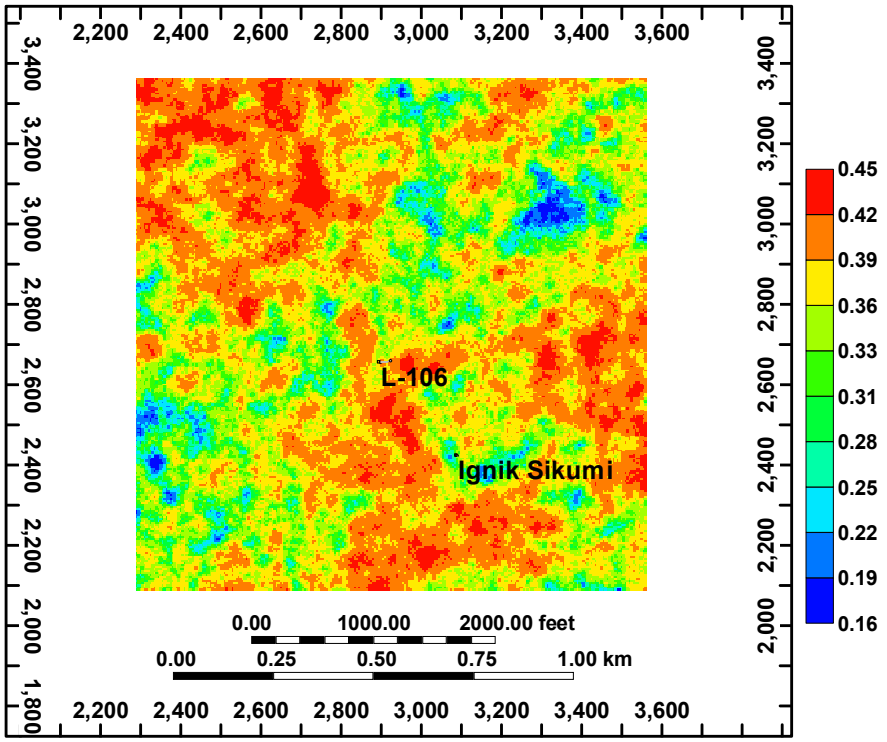

(a)

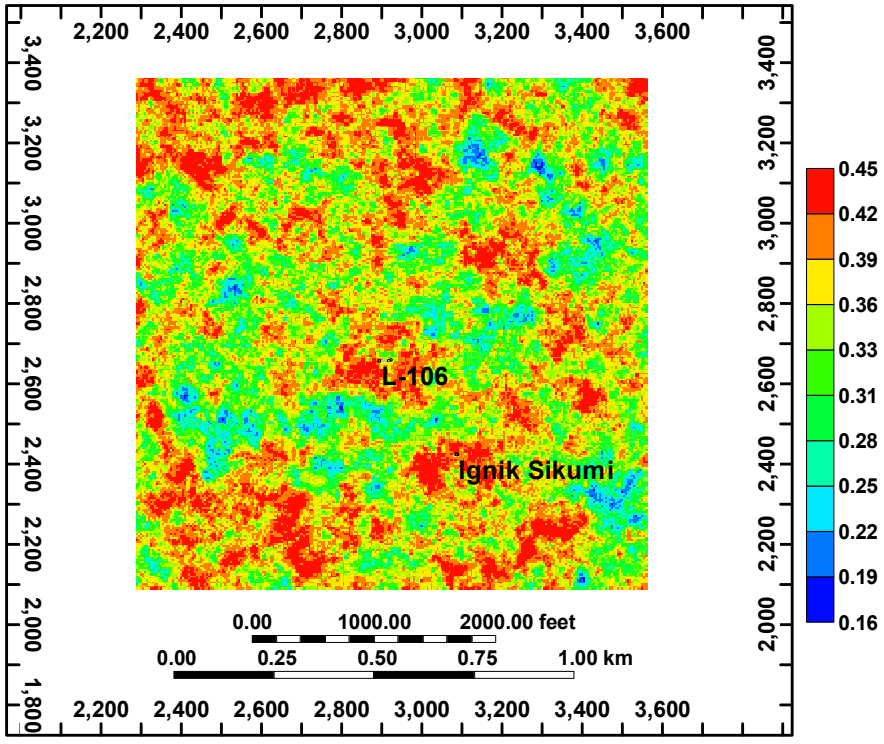

(b)

Figure A-10: Horizontal cross-sections across the middle of (a) D, and (b) C sands showing stochastically simulated porosity distribution

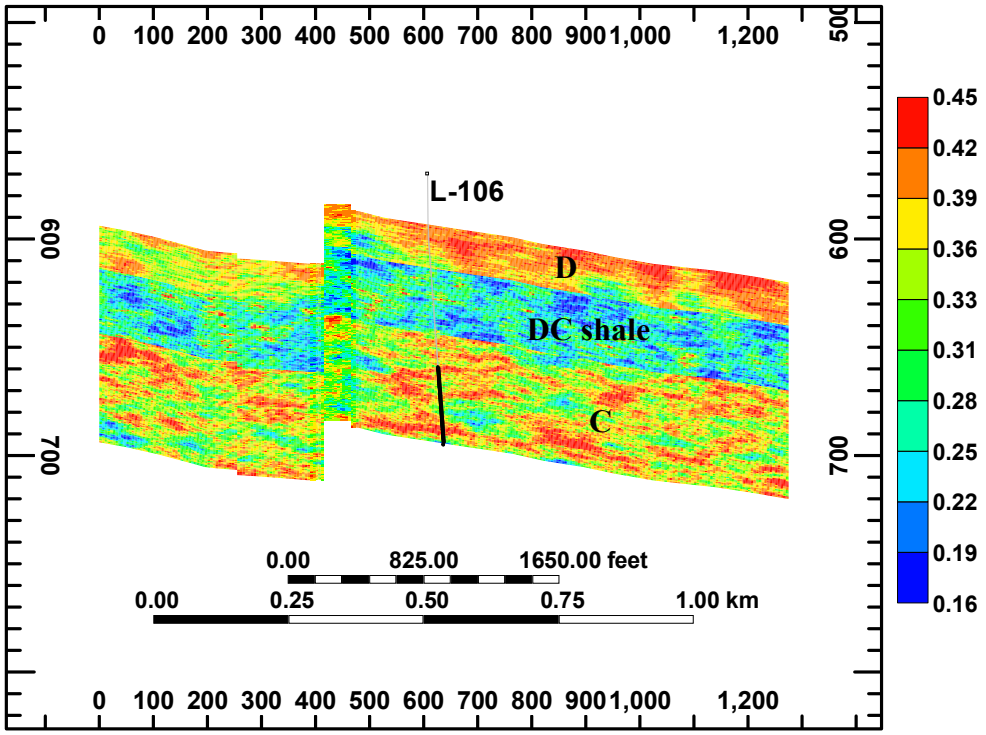

(a)

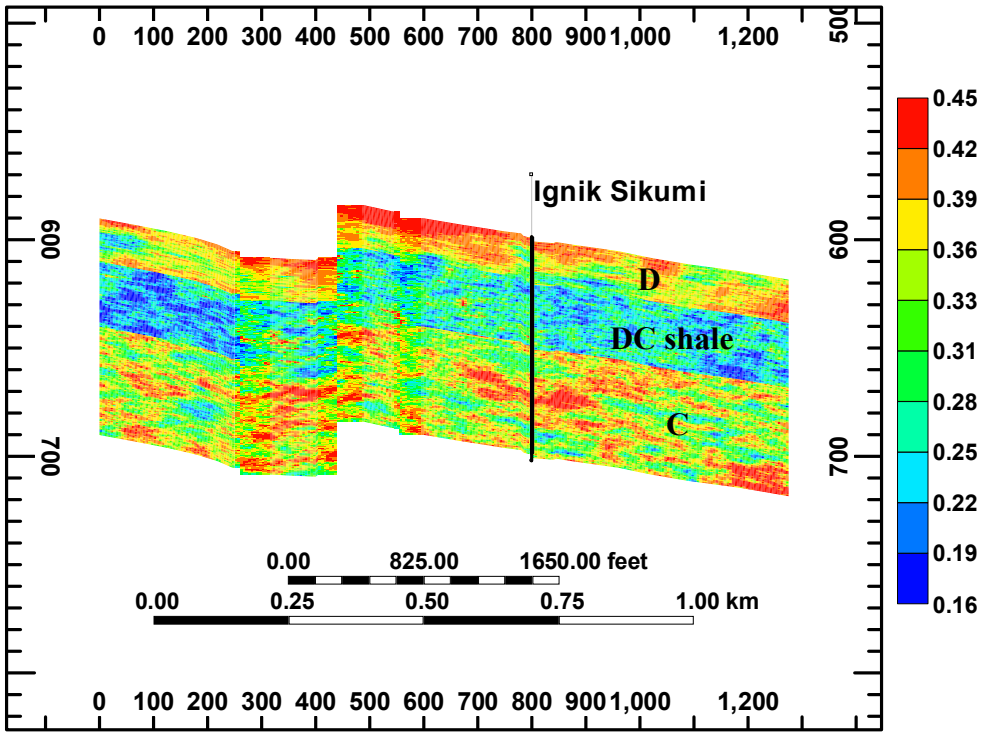

(b)

Figure A-11: Vertical cross-sections across (a) L-106, and (b) Ignik Sikumi wells showing stochastically simulated porosity distribution in the D, DC shale and C units

Figure A-12 shows that results from stochastic simulation are very close to the original well log-inferred porosity values, which confirms that the resulting distribution is tightly controlled by the input well log data.

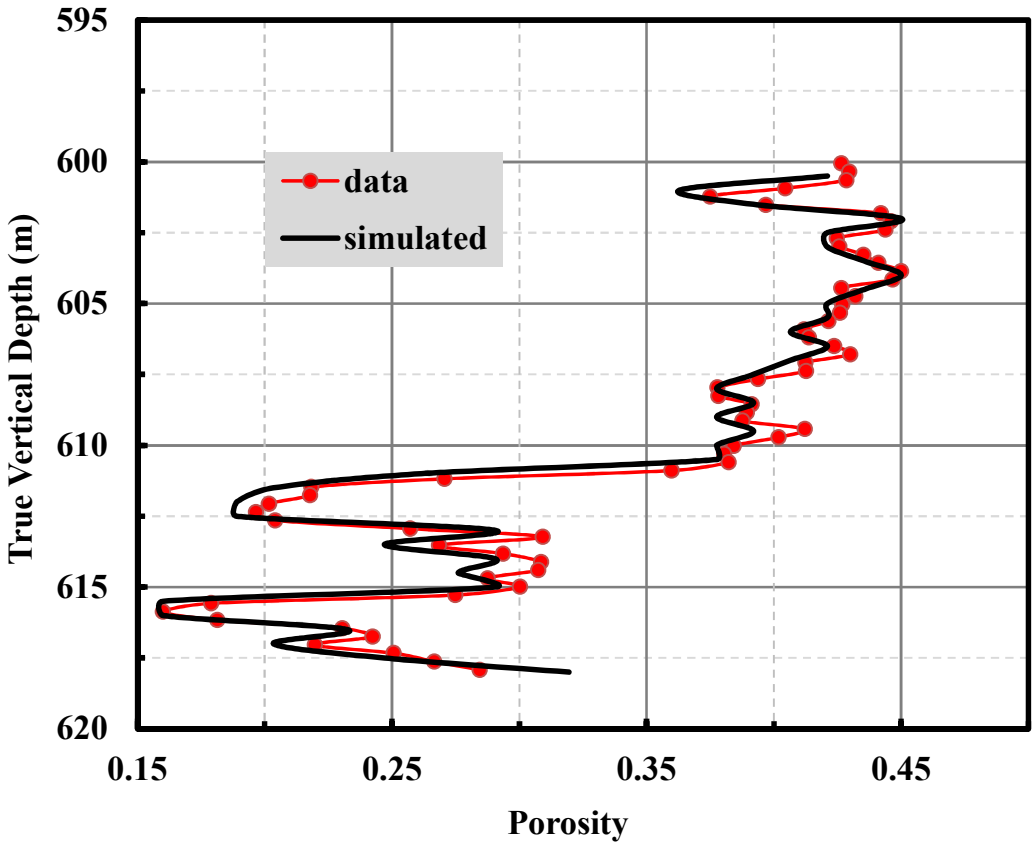

Figure A-12: Comparison of sampled porosity values taken at L-106 with those extracted from a porosity realization field at the same location and the Unit D sand interval.

B. Well Drilling Design

This section of the appendix provides a guide (Table B-1) to drilling the well configurations studied in Section 3.6 of the main text.

Table B-1: Drilling guide for inclined well configurations on the L-Pad

Well-2a	
Entry depth @ D sand	610 m
Deviation from the vertical	82.0 ^{0}

Radius of Curvature (m)		**Build Rate**		**Kickoff Depth (m)**	**Horizontal Departure (m)**
Long Radius	286	6 ^{0}/100 ft	0.2 ^{0}/ m	200	247
Medium Radius	82	20 ^{0}/100 ft	0.7 ^{0}/ m	493	70
Short Radius	7	7.5 ^{0}/3 ft	8.2 ^{0}/ m	600	6

Well-2b	
Entry depth @ D sand	686 m
Deviation from the vertical	98.0 ^{0}

Radius of Curvature (m)		**Build Rate**		**Kickoff Depth (m)**	**Horizontal Departure (m)**
Long Radius	286	6 ^{0}/100 ft	0.2 ^{0}/ m	1176	326
Medium Radius	82	20 ^{0}/100 ft	0.7 ^{0}/ m	826	93
Short Radius	7	7.5 ^{0}/3 ft	8.2 ^{0}/ m	698	8

Well-3a	
Entry depth @ D sand	591 m
Deviation from the vertical	81.5 ^{0}

Radius of Curvature (m)		**Build Rate**		**Kickoff Depth (m)**	**Horizontal Departure (m)**
Long Radius	286	6 ^{0}/100 ft	0.2 ^{0}/ m	184	244
Medium Radius	82	20 ^{0}/100 ft	0.7 ^{0}/ m	475	70
Short Radius	7	7.5 ^{0}/3 ft	8.2 ^{0}/ m	581	6

Well-3b	
Entry depth @ D sand	686 m
Deviation from the vertical	98.5 ^{0}

Radius of Curvature (m)		**Build Rate**		**Kickoff Depth (m)**	**Horizontal Departure (m)**
Long Radius	286	6 ^{0}/100 ft	0.2 ^{0}/ m	1179	329
Medium Radius	82	20 ^{0}/100 ft	0.7 ^{0}/ m	827	94
Short Radius	7	7.5 ^{0}/3 ft	8.2 ^{0}/ m	698	8

Table B-1: Drilling guide for inclined well configurations on the L-Pad (cont'd)

Well-L2a		
Formation entry depth	D Sand	596 m
	C Sand	653 m
Deviation from the vertical		87.7 ^{0}

Radius of Curvature (m)		Build Rate		Kickoff Depth (m)		Horizontal Departure (m)
				D Sand	C Sand	
Long Radius	286	6 ^{0}/100 ft	0.2 ^{0}/ m	158	215	275
Medium Radius	82	20 ^{0}/100 ft	0.7 ^{0}/ m	471	547	79
Short Radius	7	7.5 ^{0}/3 ft	8.2 ^{0}/ m	585	668	7

Well-L2b		
Formation entry depth	D Sand	621 m
	C Sand	679 m
Deviation from the vertical		92.3 ^{0}

Radius of Curvature (m)		Build Rate		Kickoff Depth (m)		Horizontal Departure (m)
				D Sand	C Sand	
Long Radius	286	6 ^{0}/100 ft	0.2 ^{0}/ m	1083	1141	298
Medium Radius	82	20 ^{0}/100 ft	0.7 ^{0}/ m	753	811	85
Short Radius	7	7.5 ^{0}/3 ft	8.2 ^{0}/ m	632	690	7

C. Sensitivity to well perforation

Figure C-1 shows the results of the sensitivity runs conducted on well perforation intervals (mentioned in Section 3.6.2). Figure shows that initial gas rates are reduced as interval between the perforations are multiplied by a factor of 3 (*ref. x3*) and 9 (*ref. x9*), respectively when compared with the results of the original Well-2a (*ref.*). The cumulative gas volumes at the end of 30 years are essentially the same, however, at ~ 3 yr there is a difference of 8.4 x 10^7 ST m^3 (~ 3 BSCF) in total volume produced between *ref.* and *ref. x9*. Owing to the fact that the net present value is more strongly dependent on production volumes in the earliest years, the well perforation intervals of the reference case would be the economic choice, provided there is no significantly increased cost associated with a higher well perforation density. However, a well with perforation interval of *ref. x3* would be a good compromise if there are appreciable costs associated with more well perforations.

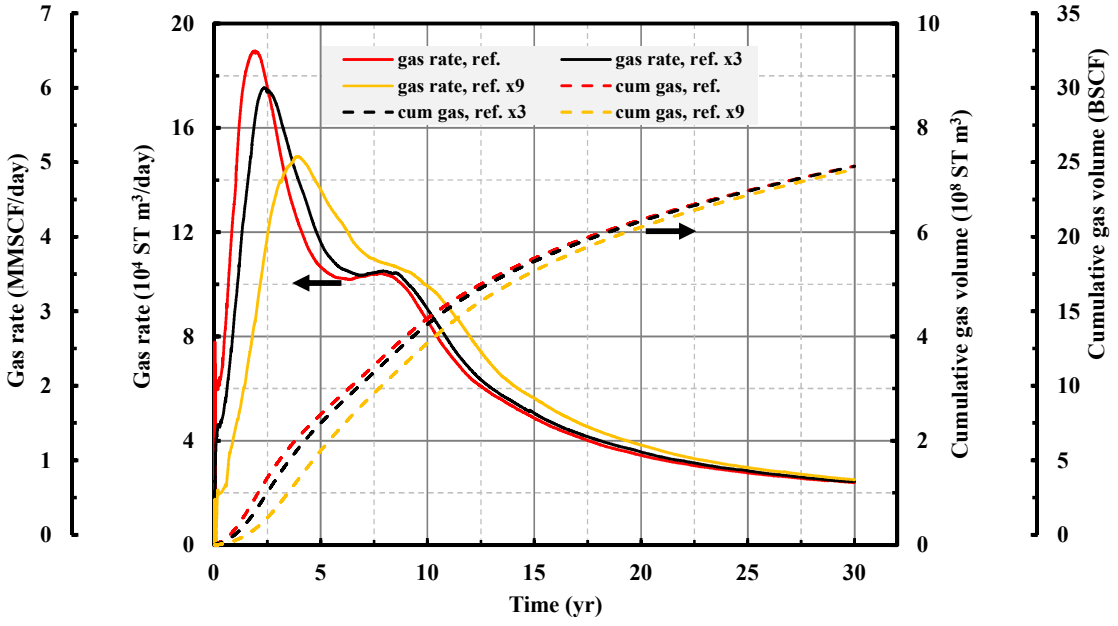

Figure C-1: Gas rates and cumulative volumes from wells with varying perforation density

References

1. Isaaks, E.H. and Srivastava, R.M., *Applied geostatistics*. 1989: Oxford University Press.
2. Clayton, V. and Journel, A.G., *Gslib-geostatistical software library and user's guide.* Technometrics, 1998.
3. Pyrcz, M.J. and Deutsch, C.V., *Geostatistical reservoir modeling*. 2014: Oxford university press.
4. Kelkar, M., Perez, G., and Chopra, A., *Applied geostatistics for reservoir characterization*. 2002: Society of Petroleum Engineers.